

Thermal error and temperature-dependent dynamics modeling of CFRP machine tool spindle unit using IoT system

February 2023

Makoto Kato

A Thesis for the Degree of Ph.D. in Engineering

Thermal error and temperature-dependent dynamics modeling
of CFRP machine tool spindle unit using IoT system

February 2023

Graduate School of Science and Technology
Keio University

Makoto Kato

Table of contents

Table of contents	i
Nomenclature.....	v
1. Introduction	1
1.1. Overview of digital twins in machine tools.....	1
1.2. Motivation behind digital twins for carbon fiber reinforced plastics (CFRP)- structured machine tools (CFRPMTs).....	3
1.2.1. Structure of Internet of Things (IoT) systems	4
1.2.2. Energy efficiency of machine tools.....	5
1.2.3. Energy-saving performance of CFRPMTs.....	7
1.3. Thermal error compensation techniques for high-precision machining.....	10
1.3.1. Machining accuracy of machine tools	10
1.3.2. Counterplan against thermal deformation	11
1.3.3. Estimation models using machine learning.....	14
1.4. Chatter avoidance techniques for high-efficiency machining	15
1.4.1. Mechanism of chatter in the milling process and stability lobe diagrams	16
1.4.2. Receptance coupling substructure analysis and Timoshenko beam models (TBMs) of composite materials.....	19
1.4.3. Factors causing dynamic property changes on machine tools and chatter avoidance techniques in process	20
1.5. Research purpose.....	22
1.5.1. Motivations and objectives	22
1.5.2. Organization of the dissertation	24
2. Development of temperature analysis environment on CFRPMT and IoT systems.....	27
2.1. Prototype CFRPMT	27
2.2. Construction of temperature analysis environment	29

2.2.1.	Introduction to large-scale array of temperature sensors interconnected in series (LATSIS) and temperature measurements on the CFRPMT.....	29
2.2.2.	Machine to machine gateway for LATSIS and displacement sensors	30
2.2.3.	Data server with web application for monitoring.....	31
2.2.4.	Artificial intelligence-based application for estimation and feedback control	32
2.3.	Communication performance of the temperature analysis environment.....	33
2.4.	Summary	36
3.	Thermal error analysis and modeling of CFRPMTs against spindle rotation	38
3.1.	Thermal error measurement according to spindle rotation and idle conditions	38
3.2.	Thermal error analysis of CFRP spindle unit	39
3.2.1.	Thermal error behaviors against cold start and idle reduction.....	39
3.2.2.	Thermal error behaviors against spindle rotational speed.....	42
3.3.	Development of regression models of thermal errors	44
3.3.1.	Data cleansing of temperature and displacement data	44
3.3.2.	Deployment of multiple linear regression (MLR) models for thermal error estimation.....	44
3.3.3.	Discussion of temperature measurement points based on principal component analysis.....	46
3.4.	Performance evaluation of regression models	50
3.4.1.	Performance evaluation against cold start machining.....	50
3.4.2.	Performance evaluation against idle reduction of cooling system	52
3.5.	Summary	55
4.	Dynamical analysis and modeling of CFRP spindle units.....	57
4.1.	Kinematic models of substructures	57
4.1.1.	One-dimensional TBM and receptance matrix	57
4.1.2.	Mechanical property identification for CFRP spindle shafts.....	62

4.2. Multipoint receptance coupling for spindle unit dynamics	65
4.2.1. Multipoint receptance coupling for individual components in axial direction	65
4.2.2. Bearing property identification from frequency response functions (FRFs).....	67
4.2.3. Multipoint receptance coupling considering contact characteristics ..	68
4.3. Validation of CFRP spindle shaft dynamics	70
4.3.1. Impact tests of CFRP spindle shaft and analysis conditions.....	70
4.3.2. Comparison and discussion of analytical models	73
4.4. Validation of motorized CFRP spindle unit dynamics.....	75
4.4.1. Impact tests at the spindle nose and bearing property identification	75
4.4.2. Results of bearing property identification and discussion of effectivity of CFRP application	76
4.5. Summary	79
5. Dynamical analysis and modeling of spindle units including thermomechanical effects	81
5.1. Experimental modeling method of spindle unit dynamics including thermomechanical effects.....	81
5.1.1. MLR models for bearing properties including thermomechanical effects	81
5.1.2. Stability lobe diagrams for predicting stable processes and a novel design of discrete spindle speed tuning.....	82
5.2. Experimental analysis of thermomechanical effects on bearing.....	84
5.2.1. Experimental setup for impact tests at spindle nose	84
5.2.2. Discussion of FRFs under temperature fluctuations	86
5.2.3. Results of bearing property identification.....	89
5.3. Regression model construction of thermomechanical effects on bearing properties.....	91
5.3.1. Selection of effective temperature sensors for MLR.....	92

5.3.2. Preparation of explanatory variables using differential information	93
5.3.3. Contact characteristics identification on taper and collet at spindle– holder–tool interface	94
5.4. Estimation of FRFs at tool tips under temperature variation	96
5.4.1. Experimental setup for impact tests at tool tips	96
5.4.2. Results under warmup operation	98
5.4.3. Results after stopping warmup operation	99
5.5. Application of the modeling of spindle unit dynamics including thermomechanical effects to stability lobe diagrams.....	100
5.5.1. Experimental setup for side milling tests under temperature changes	100
5.5.2. Results of milling tests and process stability.....	102
5.5.3. Discussion of estimated FRFs at the tool tip and chatter conditions.....	104
5.6. Summary	106
6. Conclusions	108
Appendices	112
References	119
Acknowledgements	128

Nomenclature

Roman symbols

A, B, R	Letters for characteristic equations
A_c	Cross-sectional area
A_s	Effective shear area
a_e	Radial depth of cut
a_p, a_{lim}	Axial depth of cut / critical axial depth of cut
$a_{xx}, a_{xy}, a_{yx}, a_{yy}$	Matrix elements of cutting force coefficient
b	Coefficient of MLR model
C_1, C_2, C_3, C_4	Coefficients of shape functions in natural modes
C_r	Coefficient of modal coordinates
cr, ct	Damping in rotational / translational direction
$D_{11}, D_{12}, D_{21}, D_{22}$	Matrix elements of characteristic equations of vibration
d_{in}, d_{out}	Inner diameter / outer diameter of the cross-section
E	Young's modulus
E_n	Energy consumption
F	Force in axis direction
F_t, F_r	Tangential(principal) force / radial force
f_r	Resonant frequency
f_o	Offset frequency for DSST
G	Shear modulus
H	Compliance of linear displacement against the force
$H_{xx}, H_{xy}, H_{yx}, H_{yy}$	Matrix elements of compliance at tool tip
h	Height
I	Cross-sectional area moment of inertia
$\text{Im}(H)$	Values of the imaginary part of H
K_{tc}, K_{rc}	Specific cutting force in tangential(principal) / radial direction
k_c	Chatter lobe number
kr, kt	Stiffness in rotational / translational direction
L	Linear displacement against the moment
L_s	Length of segments
M	Bending moment in differential elements
N	Angular displacement against the force
N_L	Axial load
n_d	Division number of cross-sectional area into unit cells
n_m	Number of modal coordinates
n_q	Number of types of materials or layers
n_s	Number of temperature sensors
n_T	Number of teeth
n_w	Number of instances of train datasets
P	Angular displacement against the moment

P_w	Power consumption
p	Number of representative points on segments or components
R_p	Relative displacement from a reference time
$\text{Re}(H)$	Values of the real part of H
S_{cf}, S_{MAC}	Evaluation value of cost function / MAC
S	Spindle speed
S_{new}	New spindle speed after update in discrete spindle speed tuning
s	Complex number (Laplace operator)
T	Temperature
T_a	Time delay between two consecutive cuts
t	Time
t_c	Sampled number from a reference time
V	Shear force in differential elements
V_o	Volume ratio of used materials
Y	Displacement in frequency domain
x, y, z	Displacement in X- / Y- / Z-axis (y indicates translational displacement from the centroidal axis in differential elements; z indicates position on the centroidal axis of cross-section in differential elements in section 4.1)
X, Y, Z	Cartesian coordinate system X / Y / Z

Greek symbols

$\alpha, \beta, \lambda, \delta, \kappa, \xi, \nu$	Letters for characteristic equations
α_c	Constant for proportional damping
a_e	Radial depth of cut
γ	Shear distortions of the normal line in differential elements
Δh	Extension of material against force
ΔT	Different data of temperature
Δp	Different data of displacement
$\Delta x, \Delta y$	Vibration displacements of tool path in milling process
ε	Phase difference between the displacements of cutting edges
ζ	Structural damping
η_{MT}	Energy efficiency of machine tool
θ	bending angle of the normal line in differential elements
ϑ	Angle of the divided area in polar coordinates
$\vartheta_{st}, \vartheta_{ex}$	Start and exit angles of cutter engagement
Λ	Reciprocal of the eigenvalues
ν	Poisson's ratio
ρ	Density of material of beams
σ	Stress in rule of mixture
τ	Shear stress in rule of mixture
τ_K	Interval for different values
τ_{MT}	Productivity of machine tool

$\phi(z)$	Shape functions of translational displacement under vibration conditions
$\psi(z)$	Shape functions of bending angle under vibration conditions
ω	Angular frequency
ω_c	Chatter angular frequency

Matrices and vectors

\mathbf{b}	Coefficients of MLR model
\mathbf{F}	Force vectors of the receptance matrix in translational and rotational directions, force vectors of milling process in XY plane
\mathbf{K}	Dynamics of spring–damper system
\mathbf{M}	Mass matrix of modal coordinates
\mathbf{S}	Receptance matrix
\mathbf{T}	Temperature matrix for the normal equation of MLR
\mathbf{x}	Position vectors of the receptance matrix
$\Delta\mathbf{T}$	Temperature vector of different data
$\Delta\mathbf{R}$	Displacement vector of different data
$\Delta\mathbf{x}$	Vibration displacement vector
$\Phi(z)$	Shape function vector

Subscript

$BaseMT$	Value of BaseMT
$CFRPMT$	Value of CFRPMT
DC	Value of DC component (value in zero order)
ht	Holder–tool interface
i, k	Index number of row / column in receptance matrix, index number of sensors / instance in MLR
j, l	Index number (e.g., tooth number, unit cubes on cross-section)
$meas$	Measurement values
r	Number of natural modes
sh	Spindle–holder interface
x_u, y_u, z_u	Direction of coordinates on a unit cube
x, y, z	Direction of machine coordinates of spindles

Superscripts

A, B, C	Substructure or element A / B / C
$chiller$	Cooling units
cut	Material removal process
D	Spindle shaft
E	Bearings
H	Holder
n	Number of elements
$process$	Entire machining process

<i>q</i>	Type of used materials
<i>rot</i>	Rotational mode
<i>S</i>	Spindle shaft with bearings and rotor
<i>SH</i>	Spindle–holder assembly
<i>SHT</i>	Spindle unit (spindle–holder–tool assembly)
<i>T</i>	Tool
<i>trans</i>	Translational mode
() : Parentheses	Structures
' : Dash	A first-degree position differentiation

Abbreviations

AC	Alternate current
AI	Artificial intelligence
API	Application programming interface
A/D	Analog to digital
BaseMT	Base machine tool modeled after CFRPMT
CAD	Computer aided design
CAM	Computer aided manufacturing
CFRP	Carbon fiber reinforced plastics
CFRPMT	Carbon fiber reinforced plastics-structured machine tool
CNC	Computerized numerical control
CPS	Cyber-Physical Systems
CSS	Cascading style sheets
CSSV	Continuous spindle speed variation
CSV	Comma separated value
DC	Direct current
DSST	Discrete spindle speed tuning
FEA	Finite element analysis
FFT	Fast Fourier transform
FRF	Frequency response function
HTML	Hyper-text markup language
HTTP	Hyper-text transfer protocol
ID	Identification number
IoT	Internet of Things
LAN	Local area network
LATSIS	Large-scale array of temperature sensors interconnected in series
MAC	Modal assurance criterion
ML	Machine learning
MLR	Multiple linear regression
MRR	Material removal rate
M2M	Machine to machine
NC	Numerical control

OPC UA	Open platform communications unified architecture
PC	Personal computer
REC	Resin concrete
RMSE	Root mean square error
RS-232C	Recommended Standard 232 version C
SOMS	Self-optimizing manufacturing systems
TBM	Timoshenko beam model
TCP	Tool center point
TCP/IP	Transmission control protocol/ internet protocol
TTL	Transistor-transistor logic
1D	One-dimensional
3D	Three-dimensional

1. Introduction

1.1. Overview of digital twins in machine tools

The main task of machine tools is machining with sufficient accuracy and productivity. The form accuracy of workpieces depends on the motion accuracy for positioning and feeding the tools and workpieces of the machine tool. The accuracy of the machine tool must be higher than the required accuracy on the workpiece, generally 10 times or higher. The machining conditions to ensure high productivity are also limited by the mechanical and control characteristics of machine tools. Therefore, the performance of machine tools directly affects the production quality. The development of machine tools is a long-standing subject in manufacturing science and technology and hence contributes to the growth of the industry.

The 1st industrial revolution in which power was generated using steam engines introduced mass production. In the 2nd industrial revolution, motors that use electric power enabled the inverter control of motions and the division of power sources, leading to the advent of manufacturing lines that increased production efficiency. In the 3rd industrial revolution, represented by the invention of numerical control (NC) machine tools and computer-aided design (CAD) software, digitalization using computer technology improved accuracy and repeatability. Machining was automatically performed by the developed NC programs. Digital prototypes greatly reduced the failure of physical prototypes or replaced physical prototypes [1]. The convenience and productivity of manufacturing systems could respond to the need for variety and variable production types, such as mass customization. In the 4th industrial revolution, which is considered to be from the 2010s, the intelligence of machine tools is strongly expected to optimize the entire production/manufacturing process to enhance reliability, efficiency, and flexibility [1], [2]. The concept of Cyber-Physical Systems (CPS) is a representative solution that is a collaboration between computational entities, which are intensively connected to the surrounding physical world and data-accessing/processing services available on the Internet [2], [3]. Currently, the concept in industries is summarized by the term “Industry 4.0” relying on the Internet of Things (IoT), which is a technology that embeds electronics, software, sensors, and network connectivity into devices to allow the collection and exchange of data through the Internet [4]. IoT systems can collect data from fields and provide valuable services, which are processed and optimized by using artificial intelligence (AI) tools, such as machine learning (ML) and cloud computing.

Digital twin is the largest trend in CPS for machine tools, which is defined as “a digital representation of an active unique product (real device, object, machine, service, or

intangible asset) or unique product-service system (a system consisting of a product and a related service) that comprises its selected characteristics, properties, conditions, and behaviors by means of models, information, and data within a single or even across multiple life cycle phases.” [5]. Digital twin can be simulated in multi-physics and multi-scale level based on the modeling of machine tools and processes. The updated simulation results are obtained by real-time synchronized data acquisition and provide optimized and advanced decisions by monitoring the machine conditions and state estimations.

Additionally, modern machine tools have complex structures in response to the need for sufficient accuracy and productivity. Due to the increasing demands for highly efficient, flexible, lightweight, and energy saving machine structures, ensuring productivity has become an essential goal of manufacturers [6]. The higher the rotational speeds and torque, the larger the complexities of the phenomena and the larger the thermal deformation on machine tools [7]. The industry recognizes that thermal errors are a critical issue that causes deterioration of form accuracy compared with geometric, static, and dynamic errors [8]. The study of thermal errors/vibration is a long-standing subject to achieve high-precision machining with high productivity. As an approach to mechanical design, employing carbon-fiber-reinforced plastics (CFRP) improves machine performance because of its high specific rigidity and thermal stability [9]–[11]. However, achieving complete reduction in deterioration of form accuracy only by mechanical design is difficult, and numerical models of thermal deformation and dynamics become more complex due to different thermal conductivity and dynamical properties between materials as well as its anisotropy. Digital twin is expected to be the breakthrough of limitations on the modeling and engineering analysis capabilities of simulation [12]. The analysis of thermal deformation and dynamics on machine tools using advanced structural materials with IoT systems is essential for the improvement of machining accuracy and productivity and the discussion of the interaction between physical and virtual entities. Model construction using actual measurement data has the potential to enhance the performance of machining, in comparison with the conventional approach that only uses simulations following the progress of machine tool components in Industry 4.0.

As a case study of digital twin, this study attempts to develop IoT systems on a CFRP-structured machine tool (CFRPMT). The applications of digital twin and saving energy are introduced in Section 1.2. The problems of thermal errors and chatter are reviewed from the viewpoint of the implementation of IoT systems and saving energy. Section 1.3 reviews the phenomena and compensation techniques for thermal errors to improve machining accuracy. Section 1.4 reviews the phenomena and avoidance techniques for chatter to improve productivity. Finally, Section 1.5 presents the aim and organization of the dissertation.

Table 1-1 Information links of SOMS' components

Links of SOMS' components	Outlines	Connection of physical and virtual entities
CAD/CAM and controller	Trajectory planning considering process, machine, and controller characteristics	No
Model to process	Simulation of process machine interactions	Yes
Process to production quality	Prediction of machining results	No
Process to machine	Multi-physical monitoring	No
Machine to process	Autonomous adaptronic machine components	No
Model to monitoring	Model-based "teach-less" and re-calibrating monitoring	No
Model and controller	Machine simulation including mechanical, thermal and control behavior	No
Machine to controller/monitoring	Control-integrated monitoring	Yes
Controller/monitoring to machine	Process control	Yes
Production quality to intelligent components	Feedback of workpiece quality data	Yes

1.2. Motivation behind digital twins for carbon fiber reinforced plastics (CFRP)-structured machine tools (CFRPMTs)

The works of digital twins are virtual factories [4], where the evolution is by the digitalization of the knowledge and intelligence of workers. A possible application is self-optimizing manufacturing systems (SOMS). SOMS aim to autonomously adapt to the ever-changing manufacturing environment and continuously optimize the control settings for the production quality (i.e., workpiece quality, productivity in terms of parts produced per time, manufacturing stability, reliability, and costs of energy and resource efficiency) [13]. The substituted components of intelligence are represented as model, controller, and monitoring. The required information links of the components of SOMS are listed in Table 1-1. The intelligence is built using the connection of the physical and virtual entities by the technologies of CPS. Moreover, the analysis and simulation of mechanical, thermal, and control behaviors produce meaningful information of the production quality [13]. These models serve as a base for the intelligence as well as the quality of SOMS.

The key components for the construction of CPS are IoT systems sensing physical data. The construction of IoT systems is reviewed in subsection 1.2.1. Being energy efficient, which is an important performance metric for machine tools, as well as having high machining accuracy and productivity is reviewed in subsection 1.2.2. The development of

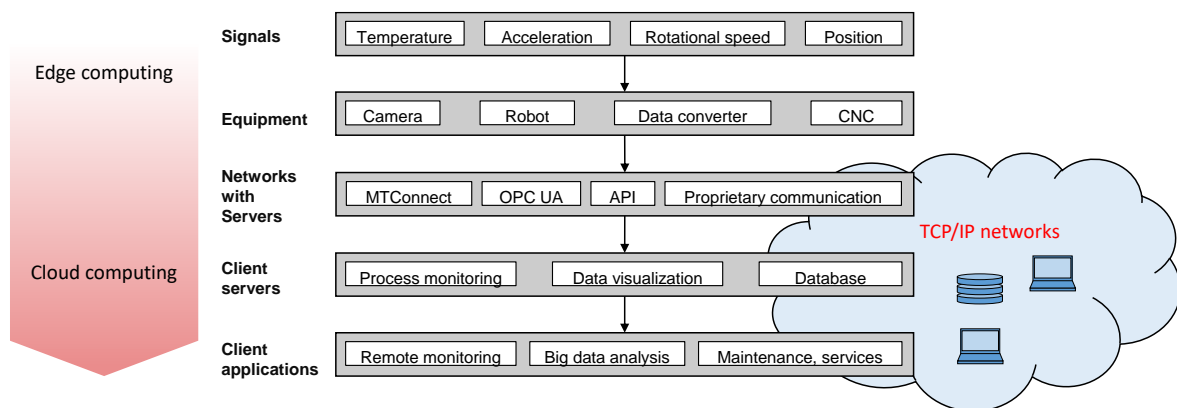


Fig. 1-1 Examples of constructing an IoT platform for production systems.

mechanical and thermal models on a modern machine tool having complex structures plays an important role. As the introduction to employing a CFRPMT, the improvement of the energy-saving performance by using CFRP is reported in subsection 1.2.3.

1.2.1. Structure of Internet of Things (IoT) systems

As various types of equipment are used in production systems, IoT technologies have become a foundation for connecting all entities (Fig. 1-1). Sensor or control signals, such as process data or machine information, are collected from the equipment. Processing on or near the equipment is called edge computing. In the development of a digital twin using edge computing exclusively, a computerized numerical control (CNC) connects additional storages and computers with wiring, and the applications must be installed and maintained in each of the equipment. Servers pre-process and label data from the equipment for data communication. Client servers must have data storage and visualization functions, which contribute to the implementation of intelligent technologies and valuable services through transmission control protocol/ internet protocol (TCP/IP) networks.

For networks of production systems, several royalty-free communication standards have been set. MTConnect was developed by the MTConnect Institute to standardize access to machine tool information [14]. A web service was developed for 5-axis mill turn centers to generate reports and notifications of various operations [15]. An application of the machine tool component, called MTConnect Adapter, was developed to transform machine tool information from a proprietary communication (MAPPS HMI). A server that collected data from Adapter, called MTConnect Agent, communicated with client servers using hyper-text transfer protocol (HTTP) technology. For a tabletop 3-axis milling machine with a dynamometer, an accelerometer, a round/minute meter, and radio frequency identification tags [16], the MTConnect architecture was implemented to monitor the signals and status, where an application programming interface (API) was used to connect to the CNC. A

monitoring system for the finish machining of the assembly interface was constructed by connecting the CNC and force sensors on the holding device through a proprietary communication (PROFINET) [17]. The Open platform communications unified architecture (OPC UA) is an machine to machine (M2M) communication protocol for industrial automation developed by the OPC Foundation [18], which is also embedded in a novel communications standard called universal machine technology interface to standardize Industry 4.0 [19]. To collect CNC data through three proprietary communications (FOCAS, SuperCom, and cncapi) [20], the OPC UA server was set up for each CNC. The drilling process was automated by an application using computer-aided design information through the OPC UA and by transmitting a robot program through a proprietary communication (EtherCAN) [21].

Recently, most vendors of controllers and/or machine tools prepare OPC UA and/or MTConnect interfaces; however, conventional equipment and external sensors require networks with servers capable of data format transformation. Sensor integration in [16], [17] was implemented using the same server to Adapter as the connection to the CNC. Existing machines are rarely equipped with sufficient interfaces for large and various data. An additional server is suitable for factory information, such as the room temperature, movement of carriers and/or workers, and other characteristics. An advantage of server client networks in factories is the division of each piece of equipment for a simple connection with Ethernet and for maintaining edge computing. Moreover, client applications must implement cloud computing in various equipment, where the architecture from signals to networks (with servers) remains flexible.

1.2.2. Energy efficiency of machine tools

Recently, the energy efficiency of machining tools has been garnering attention [22]. Motorized spindle units are equipped with high-power motors that produce a large amount of heat. Therefore, in most applications, spindle housing is equipped with a liquid cooling medium in a closed cooling circuit [23], [24]. The power consumption of peripheral equipment, such as chillers, coolant pumps, controllers, and servo amplifiers, excluding the energy for the material removal process, accounts for the majority of the power consumption of 5-axis machine tools [25]. According to the analysis of power consumption (Fig. 1-2), cooling systems account for 51% of the total energy consumption in the operation on a 5-axis machine tool [26]. The electricity consumption of machine tools depends on the duration of operations.

An approach to make machine tools more energy efficient is the improvement of productivity through the optimization of tool path on NC program, the operation of peripheral equipment as inverter control, and the automations such as automatic tool

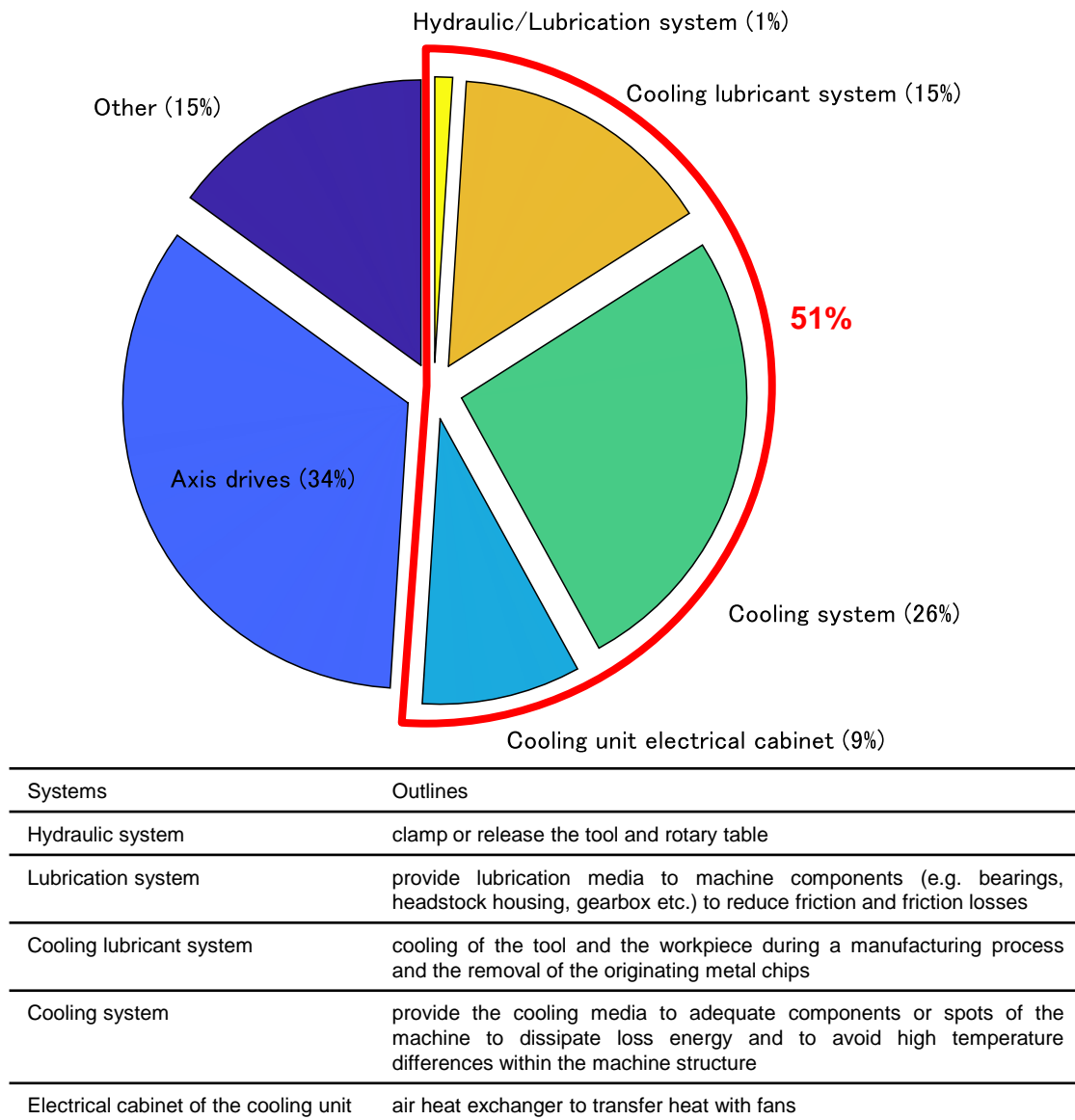


Fig. 1-2 Energy demand of a 5-axis machine tool (DMU80 eVo linear, DMG Mori). [26]

changer (ATC) and automatic pallet changer. Consequently, a development scheme for milling tools that enable higher feed rates with the optimization of the depth of cut and feed rates based on allowable cutting force has been proposed [27]. The machining condition was optimized by developing a virtual machine tool as a digital twin in terms of energy consumption [28]. Square end mills with high removal capacity, rather than ball end mills, were used for the 5-axis machining process based on the development of a computer aided manufacturing (CAM) system that could generate efficient tool paths [29]. An analysis of the power demand for facing, milling, turning, and drilling was conducted, and the most efficient machining process considering the wear and tear of the tool was identified [30]. Meanwhile, propositions for the efficient use of peripheral equipment have been made. For example, propositions for optimization of the cooling systems by controlling the flow rate of

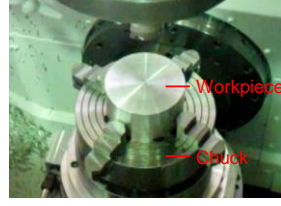
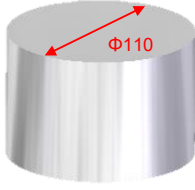
cutting fluid [31], controlling the bed cooling mechanism [32], and analyzing the spindle cooling mechanism [33] have been made.

Therefore, the improvement and optimization of energy efficiency in each equipment and process have been achieved. For the further improvement of energy-saving performance, it is necessary to develop new machine tools that can reduce operating time and power consumption by reviewing structural materials. Reducing weight and inertia of moving parts by replacing conventional steel materials with lightweight materials will simultaneously realize high-efficiency and energy-saving [9], [34]. To this end, application of aluminum alloys, resin concrete, fine ceramics, fiber-reinforced plastics, and porous metals as structural materials for machine tools have been proposed [35], [36]. Additionally, machine tool structures must maintain rigidity and low coefficients of thermal expansion. Unlike structural steels, CFRP have the following characteristics [9]–[11]: high specific strength, specific elastic modulus, superior fatigue strength, good dimensional stability owing to the low coefficient of thermal expansion, and high heat and chemical resistance.

1.2.3. Energy-saving performance of CFRPMTs

A first machine tool employing CFRP for all elements was prototyped by the Japan Machine Tool Builders' Association [37]. The CFRPMT developed in this study is modeled after a conventional 5-axis machine tool (called BaseMT in this research) and has same size as the BaseMT. The details of each element are summarized in Chapter 2. The improvement of energy-saving performance was validated by comparing the CFRPMT and BaseMT. The standard part with the machining process and conditions for the evaluation are summarized in Fig. 1-3. As also shown in the figure, this machining process was indexed by sequence numbers N1-8. First, the top and side surfaces of a bar made of aluminum were machined to create a regular octagonal shape (N1,2). Second, drilling, chamfering, and threading were performed at nine locations on the top surface as (N3-5). Finally, drilling, chamfering, and threading were performed at four locations on each side in the same manner as the top surface using the A-axis and C-axis rotation (N6-8). The total volume removed was 114500 mm³, and that in the side rough process of N2 was 90990 mm³. For the utilization of the damping properties of CFRP, the machining condition of N2 on the CFRPMT was optimized by maximizing the feed rate where the vibration amplitude was the same as that on the BaseMT. Therefore, the energy-saving performance was compared under three conditions: machining on the BaseMT, machining on the CFRPMT, and machining on the CFRPMT with the optimized machining conditions of N2. A CNC guide (SERVO GUIDE, FANUC) was used to measure the total energy consumption of the motors, denoted by E_n^{motor} , and the total machining time, denoted by $t^{process}$.

Rough processing (N1, N2)



N1: Milling

- Φ80, 4 teeth
- Axial depth of cut: 2 mm
- Rotational speed: 2986 min⁻¹
- Feed rate: 1194 mm/min

N2: Side milling

- Φ32, 4 teeth
- Width of cut: 2mm × 6 pass
- Axial depth of cut: 9mm × 3 pass
- Rotational speed: 2986 min⁻¹
- Feed rate: 1593 mm/min (3185 mm/min on CFRPMT)

Thread processing on top surface (N3-5)



N3: Drilling

- Φ3.4, 2 teeth
- Depth of cut: 12 mm
- Rotational speed: 12240 min⁻¹
- Feed rate: 6744 mm/min

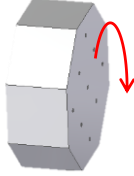
N4: Chamfering

- Φ8, 1 tooth
- Depth of cut: 1.8 mm
- Rotational speed: 3185 min⁻¹
- Feed rate: 318 mm/min

N5: Threading M4

- Depth of cut: 8 mm
- Rotational speed: 1194 min⁻¹

Thread processing on side surface (N6-8)



- C-axis rotation for the positioning of the side surface

N6: Drilling

- Φ3.4, 2 teeth
- Depth of cut: 10 mm
- Rotational speed: 12240 min⁻¹
- Feed rate: 6744 mm/min

N7: Chamfering

- Φ8, 1 tooth
- Depth of cut: 1.8 mm
- Rotational speed: 3185 min⁻¹
- Feed rate: 318 mm/min

N8: Threading M4

- Depth of cut: 8 mm
- Rotational speed: 1194 min⁻¹

Finished workpiece

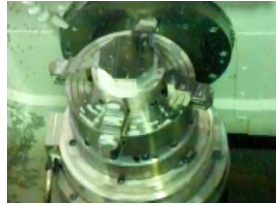
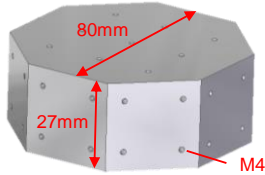


Fig. 1-3 Machining process and machining conditions of standard parts.

In the keynote paper [22], the energy efficiency of machine tools η_{MT} is defined as the ratio of the spindle power demand P_w^{SHT} to the total power demand $P_w^{process}$. In these comparisons, the required cutting energy for the removal process E_n^{cut} was assumed to be constant. The energy efficiency of machine tools was evaluated using Equation (1-1).

$$\eta_{MT} = \frac{P_w^{SHT}}{P_w^{process}} := \frac{E_n^{cut}}{E_n^{process}} = \frac{E_n^{cut}}{E_n^{motor} + P_w^{chiller} \times t^{process}} \quad (1-1)$$

Here, the total energy demand of the process is the sum of the energy demand of motors, E_n^{motor} , and peripheral equipment. The nominal value of the power consumption of the chiller $P_w^{chiller}$ is 1.2 kW, and the product of the power consumption and machining time is used as the total power of the peripheral equipment. Productivity τ_{MT} is defined as the

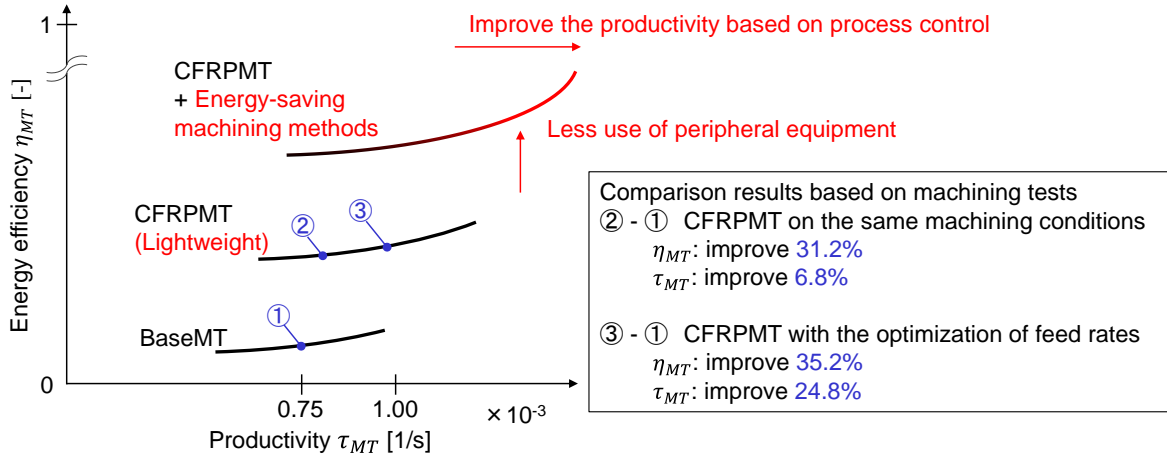


Fig. 1-4 Results and motivation of the energy-saving performance of CFRPMT.

time consumed in machining one standard part. It is the number of machined parts in unit time.

$$\tau_{MT} = \frac{1}{t_{process}} \quad (1-2)$$

Figure 1-4 shows the summary of the energy-saving performance of the CFRPMT. The improvement of energy efficiency and productivity are denoted by the ratios $\eta_{CFRPMT}/\eta_{BaseMT}$ and $\tau_{CFRPMT}/\tau_{BaseMT}$, respectively. Due to the lightweight structures of the CFRPMT, the energy efficiency and productivity were improved by 31.2% and 6.8%, respectively. Further, the optimization of the feed rate on N2 improved productivity by 24.8%. Additionally, the total energy demand decreased owing the reduction of the operation time of the chiller. Rough processing takes most of the time for the form creation, and the optimization of the machining conditions contributes to the energy-saving of machine tools.

Moreover, the dimensional errors of machined parts on CFRPMT and BaseMT were compared. As an example of the accuracy, the displacement of the Z-axis direction decreased by 36.8% from 45.9 to 29.0 μm due to cold start [37], [38]. Machining at cold start is directly beginning operations, without warm-up, on machine tools. Using the thermal characteristics of CFRP, CFRPMTs can lead to the reduction and optimization of peripheral equipment used for thermal errors. Two energy-saving machining methods, cold start and idle reduction on CFRPMT, are proposed, where idle reduction is stopping the cooling systems under standby states. These energy-saving methods can contribute to the improvement of energy efficiency of machine tools and must be implemented simultaneously with optimization of machining conditions to increase machining accuracy and productivity.

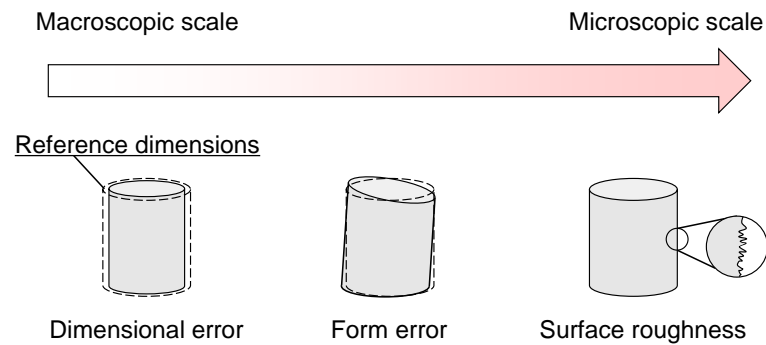


Fig. 1-5 Categorization of machining errors of workpieces.

1.3. Thermal error compensation techniques for high-precision machining

For the implementation of energy-saving machining methods, the thermal characteristics of machine tools must be discussed to maintain and improve accuracy. Section 1.3.1 introduces the requirements and categorization of the accuracy of machine tools. Section 1.3.2 explains the counterplan to deal with thermal deformation and the contribution of CFRP. Finally, Section 1.3.3 reviews the thermal error estimation using ML, which can be installed on IoT systems.

1.3.1. Machining accuracy of machine tools

A machined part has machining errors from the target dimensions, such as the reference dimensions decided by CAD models (Fig. 1-5). Machining errors can be classified into dimensional errors, form errors, and surface roughness based on their scales and characteristics [39]. The feasible levels of these machining errors are called machining accuracy of machine tools, and it is desirable for machine tools to have high machining accuracy. From the viewpoint of machining accuracy, machine tools are classified into the following three types [40]:

- Standard machine tools: machining accuracy within 10–100 μm
- High-precision machine tools: machining accuracy 1 μm
- Ultra-precision machine tools: machining accuracy within 0.001–0.1 μm

For example, standard, high-precision, and ultra-precision machine tools are used to produce machine parts such as bolts, for machining dies and molds, and for machining camera lenses that are brittle materials and require optical performance, respectively. The

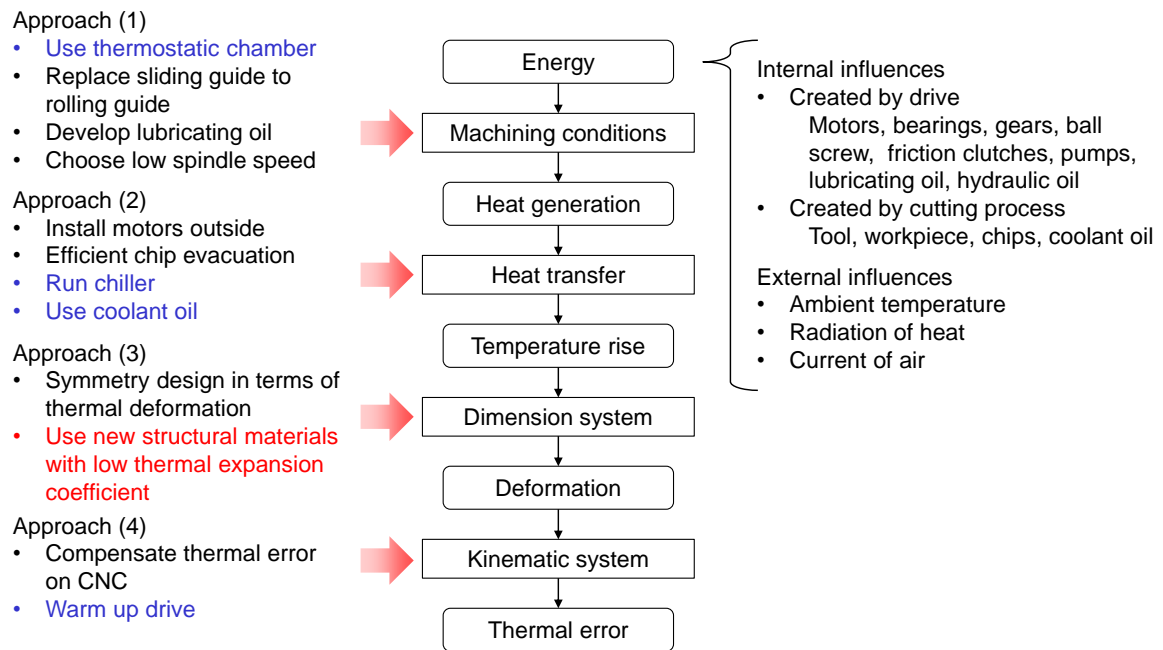


Fig. 1-6 Chain of thermal effects on machine tools and the extra operation of peripheral equipment and motors for the suppression of thermal effects. [41]

dimensional and form errors highly depend on the motion accuracy of the machine tools for feeding and positioning the cutting tool and workpiece. The machining accuracy depends on static characteristics, such as static stiffness. Meanwhile, the control bandwidth of CNC machine tools is less than 200 Hz, and the cutting tools rotate at a higher frequency. Surface roughness depends on the dynamic characteristics of machine tools.

Machining centers are 5-axis machine tools with ATCs that are capable of automatically storing, selecting, and changing the various cutting tools required at different stages of a process. Machining centers are used not only in mass production but also for machining of dies and molds. Simultaneous 5-axis machining can create high-precision three-dimensional (3D) shapes. Even in 3-axis machining, the use of the rotary axis as an index for the positioning enables the machining with one chucking of the workpiece, which can ensure machining accuracy and productivity. For this reason, machining centers have become a mainstream production tool in recent years, and the current preferred precision in the industry, as well as this research, is less than 10 μm of machining accuracy.

1.3.2. Counterplan against thermal deformation

As presented in a keynote paper, up to 75% of the dimensional/form errors on workpieces are caused by thermal influences [7]. Figure 1-6 shows the relationship between heat sources that cause thermal deformation of machine tools and machining accuracy [41]. These heat sources are classified into internal and external heat sources. Internal heat

sources include frictional heat generated by the motion and cutting heat generated by the process. Conversely, external heat sources include changes in ambient temperature and thermal radiation from lighting, other machines, and operators. The heat is transferred to the components of machine tools resulting in non-uniform temperature distributions. Temperature changes cause deformation at various points depending on the thermal expansion coefficient. Finally, the relative location between the cutting tool and workpiece changes and results in machining errors. The relative displacement from the desired position at the tool center point (TCP) is called thermal error. To improve machining accuracy, the chain from the heat sources to thermal errors must be broken. The following is the counterplan against each process of thermal effects:

(1) Process of heat generation:

Fig. 1-6 presents the environmental arrangements and machine designs to suppress temperature variation. The influence of external heat sources can be avoided by using a thermostatic chamber, preventing air convection, and preventing heat radiation. To reduce the frictional force, rolling guides can be used instead of sliding guides, and the performance of lubrication oil can be improved. Selecting a low spindle speed is an example of optimizing the machining conditions.

(2) Process of temperature rise:

The machine designs to avoid heat conduction/transfer to machine tools can be seen in commercial machine tools. The motor is mounted outside the machine body, and the showroom is designed to prevent the chips from accumulating cutting heat. From the temperature control viewpoint, a chiller runs to cool the housing, and coolant oil is used to remove the cutting heat.

(3) Process of thermal deformation:

Machine designs to minimize the influence of thermal deformation are proposed. Specifically, thermally symmetrical structures [42] and structural materials with high thermal stability are employed.

(4) Process of thermal error:

As in-process control methods, thermal error compensation to offset the TCP on NC program is discussed based on modeling methods of thermal error behaviors. In addition, warm-up operation before machining the parts is conducted to reduce evident changes in thermal errors on machining regardless of machine designs.

Using CFRP for structural materials of machine tools is a part of the counterplan to

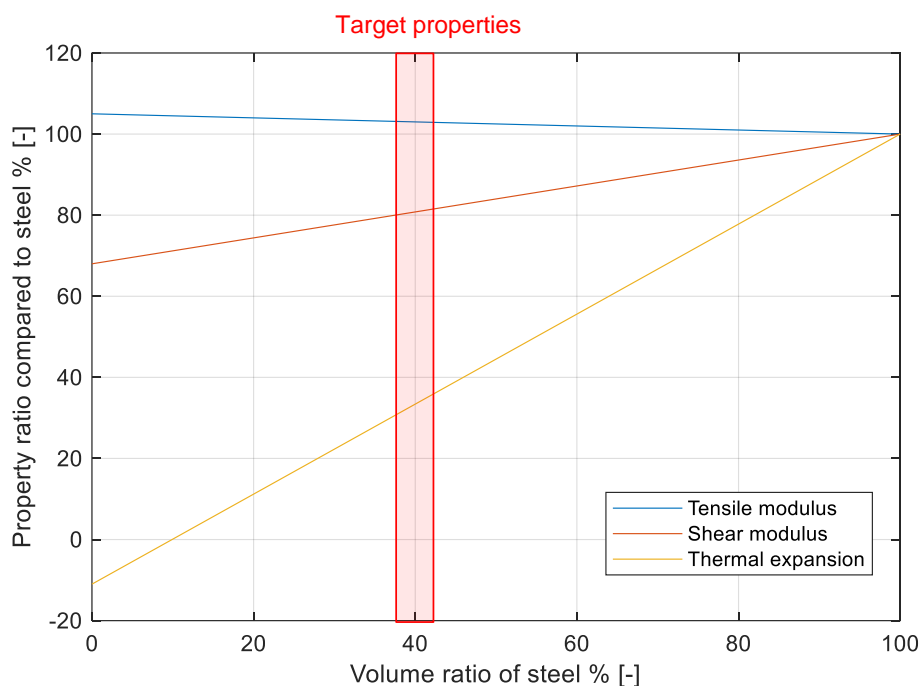


Fig. 1-7 Relationship between the steel volume ratio and properties of a spindle shaft; red area represents the target properties of CFRP spindle shafts used in this research. [11]

deal with thermal deformation. Other candidates, such as amber, ceramics, and glass, already exist as structural materials for bearings and encoders. As mentioned in Section 1.2.2, although these materials have high hardness, sufficient strength is required. Steels, as the common structural materials, have a linear thermal expansion coefficient between 10 and 15 K^{-1} . The linear thermal expansion coefficient of CFRP in the radial direction of the fibers is approximately 8 K^{-1} , and that in the axial direction is 10 times smaller than that of steels [43]. A hybrid structure of CFRP and steel was employed on the spindle shaft of the CFRPMT. An approach to the mechanical design of the thermal expansion and static stiffness was proposed by Kono et al. [11] (Fig. 1-7). The relationship between the volume ratio of steel and the linear thermal expansion coefficient/static stiffness is calculated based on the rule of mixtures [44]. However, the mechanical properties deteriorate in a perpendicular direction due to the anisotropy of composite materials. In the actual development of CFRP elements, steels are used at the outermost diameter for bearing fixation, protection of CFRP from oil and chips, and partial replacement of conventional products with bolt fastening and welding [10], [11]. Meanwhile, the uniform enhancement of the mechanical characteristics of machine tools in all directions is challenging. Although each developed element of the CFRPMT can realize small thermal expansion and simulate a positive impact on the target direction of the TCP, evaluation of thermal errors of a machine tool fully structured by CFRP is desirable.

The approaches written in blue in Fig. 1-6 require additional employment of peripheral

equipment and motors. To reduce the energy consumption of these extra operations, the analysis of thermal errors due changes in the environment temperature is required. An on/off control scheme for a hot gas bypass cooling system was proposed to facilitate operation at the optimal coefficient of performance for ideal heat exchange [45]. Consequently, a tradeoff between energy efficiency and thermally induced displacement was reported: 75% energy saving was achieved. However, the TCP fluctuation was $1.5 \mu\text{m}$ under operation at a constant low-speed spindle rotation of 1000 min^{-1} . Simultaneously, it was revealed that the cooling systems already run at the optimal high-speed spindle rotation speed. From the perspective of manufacturers, excessive temperature increases in spindle motors and bearings must be avoided. A possible way to save energy within cooling systems for high-speed spindle rotation is under idle conditions. From the perspective of thermal errors, constant low-heat sources that enable the repeatability of thermal deformation behaviors should be eliminated. Thus, to consider environment temperature changes, further discussion on spindle unit design and construction of robust estimation models is required.

1.3.3. Estimation models using machine learning

The thermal error compensation technique of subtracting estimated thermal error values from the NC program command values has high applicability, even after designing and structuring machine tools. With the progress of computing technologies, several modeling approaches have been proposed that use a considerable amount of sensor information available on structured machine tools. An artificial neural network with 11 resistance temperature detectors was proposed [46]. A multiple linear regression (MLR) model has been developed using 18 resistance temperature detectors [47]. Further, a support vector machine-based regression model has been constructed using 32 thermocouples and data on operation conditions [48]. A study employed finite element analysis (FEA) to identify 128 appropriate measurement positions for the thermal distribution against main internal heat sources [49]. Further, fiber Bragg grating sensor signals at those points were used for training long short-term memory networks, artificial neural networks, convolutional neural networks, and support vector machines. In addition, kinematic modeling methods have been widely discussed. Transfer functions, whose inputs are the temperatures of six main heat sources at the spindle, X-, Y-, Z-, and C-axis motors as well as the ambient temperature, were identified; thermal errors were estimated by linearly superposing responses against measured temperatures [50]. A study developed dynamic models in the rotational axis direction using four resistance temperature detectors, an embedded displacement sensor, and spindle speed information [23]. In addition, FEA has been used for thermal error estimation. In a study, the stiffness equation was solved by

forming 26 uniform temperature areas, and the calculation method of node displacement from temperature measurements was installed on a CNC [51]. In another study, the accumulated thermal expansions of all elements at the TCP were predicted based on the measured temperature distribution at 284 points via large-scale arrays of temperature sensors interconnected in series (LATSIS) [52]. Moreover, the performance of the aforementioned estimation and compensation techniques has been validated against test data. These regression models were trained using training datasets. The operation for data acquisition of training datasets is also considered to improve the performance.

In thermal error estimation, the calculation of compensation values incurs high computational costs. Clustering methods, such as fuzzy clustering [46], k-means clustering [47], and Bayesian networks [48], have been combined to obtain appropriate models. Even when using kinematic models, self-learning algorithms of SOMs that use previous data help maintain the estimation performance [13], [53]. Thus, the development of thermal error models with AI techniques requires IoT systems so that advanced program libraries and databases available in the cloud can be utilized. Moreover, recent machine tools should work for not only mass production but also a wide variety of products. Supposing such a flexible manufacturing system, each machine tool has different idle time for waiting and setup operation on each workpiece in job scheduling. The idle time affects the behaviors of thermal errors and the efficacy of the warm-up operation for form accuracy. To realize high-precision machining, thermal errors under noncontinuous machining over a long operation time including the idle time must be considered. The performance of thermal error estimation must be evaluated along with the implementation of energy-saving machining methods after the construction of CPS.

1.4. Chatter avoidance techniques for high-efficiency machining

High-efficiency machining is based on safe operation without unexpected failures. The machining conditions are limited by the available command values of CNC and the process-machine interactions. Abnormal vibration causes poor surface and shape quality and catastrophic tool or machine damage. Self-excited vibration, called chatter, often occurs in process despite low cutting force conditions owing to the regenerative relationship in chatter. In particular, chatter limits productivity in the industry. For the further improvement of energy efficiency, the optimization of machining conditions is essential to achieve high-efficiency machining. Section 1.4.1 presents the mechanism of chatter in the milling process and the stability lobe diagrams (SLDs) for predicting stable process as a common process planning method. Section 1.4.2 reviews a semi-analytical method to acquire machine tool

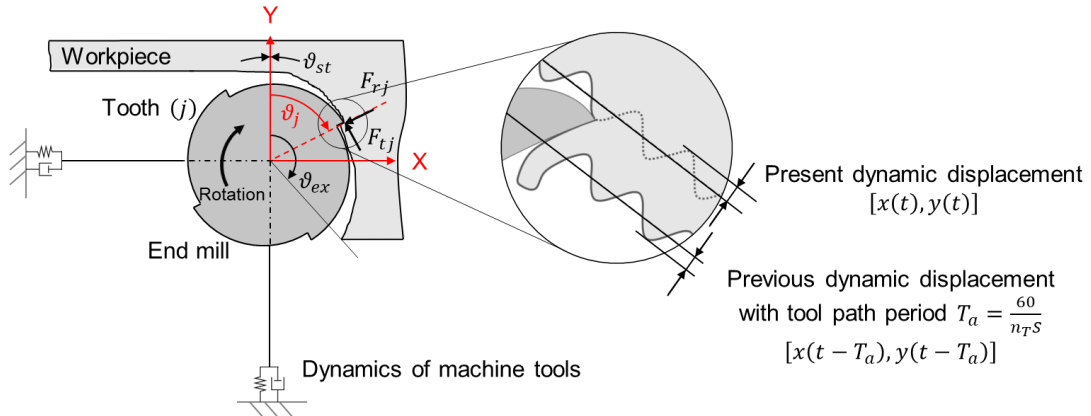


Fig. 1-8 Diagram of the cross-section of the end milling process. [54]

dynamics for the SLDs with minimum preliminary tests. Section 1.4.3 reviews the factors that deteriorate estimation quality of SLDs as well as chatter avoidance techniques.

1.4.1. Mechanism of chatter in the milling process and stability lobe diagrams

Abnormal vibrations in machining processes are roughly classified into forced vibration and chatter [6], [54]. Forced vibration is magnified by the vibration of forced disturbances like cutting force or displacement disturbances from external sources, such as motors, gears, bearings, and floors. The counterplan against forced vibration is isolating/suppressing the vibration source [55] or improving the dynamic rigidity and/or damping of the machine [56]. To reduce forced vibration of cutting, the machining conditions can be optimized by eliminating the tooth-passing frequency and its harmonics that do not synchronize with the resonance frequency of the machine tools. In particular, the end milling process has periodic cutting force fluctuations that cause forced disturbances. Meanwhile, chatter is an unstable phenomenon of the process–machine interaction owing to the transfer characteristics of the cutting process and machine structures.

Figure 1-8 illustrates the end milling process. j -th tooth moves in a trochoidal trajectory and removes the workpiece material with the radial depth of cut. The difference in the vibration displacements $\Delta x(t), \Delta y(t)$ is the difference between the trajectory of the present cutting edge and the trajectory of the previous cutting edge in the X- and Y-axes directions, respectively. Here, time delay between two consecutive cuts is T_a . The cutting force at a tooth varies with the rotation angle or time. Considering the integration of n_T teeth, the force added to the end mill tool can be obtained as follows:

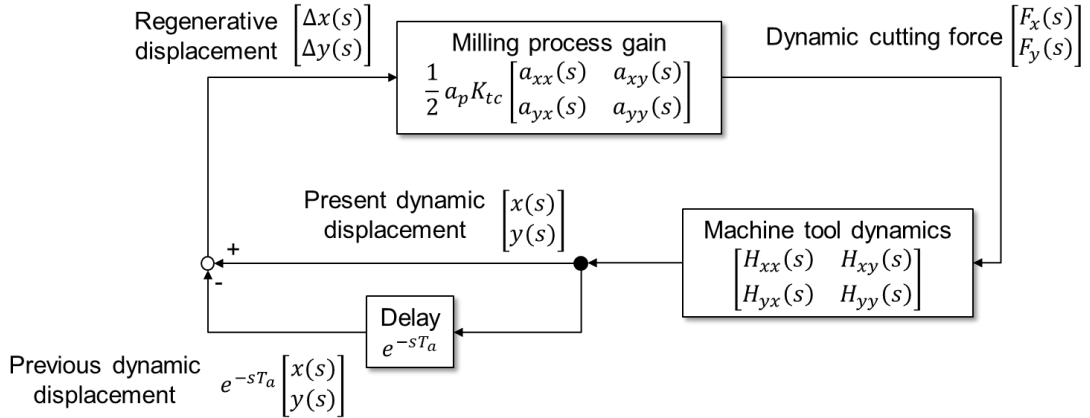


Fig. 1-9 Block diagram of the end milling process. [54]

$$F_x = \sum_{j=0}^{n_T-1} (-F_{tj}(\vartheta_j)\cos\vartheta_j - F_{rj}(\vartheta_j)\sin\vartheta_j) \quad (1-3)$$

$$F_y = \sum_{j=0}^{n_T-1} (F_{tj}(\vartheta_j)\sin\vartheta_j - F_{rj}(\vartheta_j)\cos\vartheta_j)$$

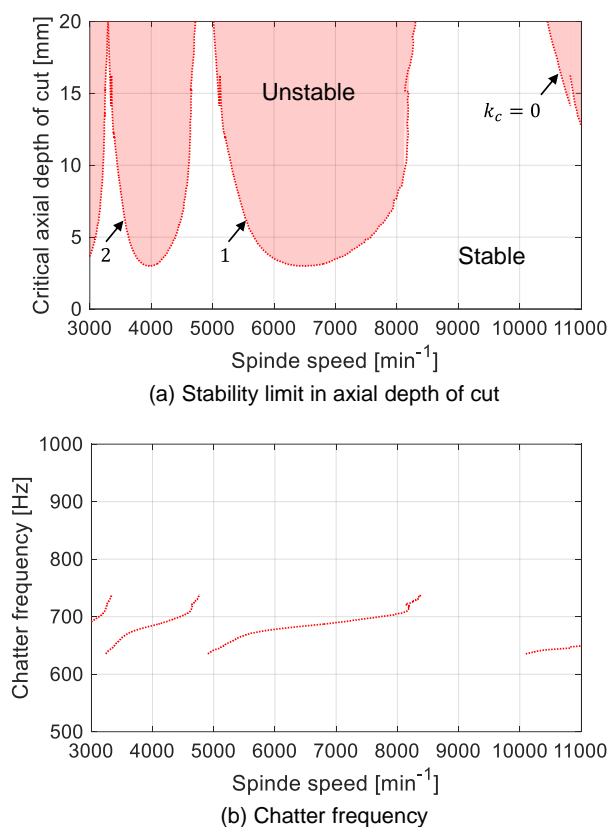
The cutting forces are written in the vectors.

$$\mathbf{F}(t) = \frac{1}{2} a_p K_{tc} \begin{bmatrix} a_{xx} & a_{xy} \\ a_{yx} & a_{yy} \end{bmatrix} \Delta \mathbf{x}(t) \quad (1-4)$$

Here, a_{xx} , a_{xy} , a_{yx} , and a_{yy} are the components of the cutting force coefficient matrix in end milling varies with time or rotation angle. a_p is the axial depth of cut and K_{tc} is the specific cutting force in tangential direction. The variation of cutting force oscillates the machine tool structures. The dynamic displacement varies the time delay, which can be expressed in the frequency domain as follows:

$$\Delta \mathbf{x} = (1 - e^{-sT_a}) \begin{bmatrix} H_{xx}(s) & H_{xy}(s) \\ H_{yx}(s) & H_{yy}(s) \end{bmatrix} \mathbf{F} \quad (1-5)$$

Equations (1-4) and (1-5) imply that the dynamic displacement results from fluctuations in the cutting forces and the dynamic displacement causes fluctuations in the cutting forces. This regenerative relationship constitutes a closed-loop system, as shown in the block diagram in Fig. 1-9. A limitation is the time dependence of the cutting force coefficient



$$K_{ct} = 220 \text{ MPa}, \frac{K_{rc}}{K_{tc}} = 0.3, n_T = 4, d_{out} = 10 \text{ mm}, a_e = 1$$

Fig. 1-10 Example of simulated stability limits for chatter in the end milling process; the machine tool dynamics use measurement results in subsection 5.4.3.

matrix to analyze the phenomena.

To solve this relation at low computational costs, the zeroth-order approximation analysis was proposed under the assumption of a single dominant frequency [57]. Figure 1-10 shows an example of the stability limit diagram. The calculation is summarized in subsection 5.5.1. Machining conditions for the analysis is attached. Process planning based on SLDs is the selection of stable machining conditions. To maximize the material removal rate (MRR) for high-efficiency machining, the axial depth of cut can be set to the maximum value at the rotational speed range of 8500–10500 min^{-1} . For more accurate assumptions about the milling process in the frequency domain, another formulation considering multiple chatter frequencies has been proposed [58]. In addition, the stability limits for specific tools and processes have been discussed, such as ball end mills [59], serrated tools [60], helix end mills [61], [62], and milling tools with unequal tooth pitch [63].

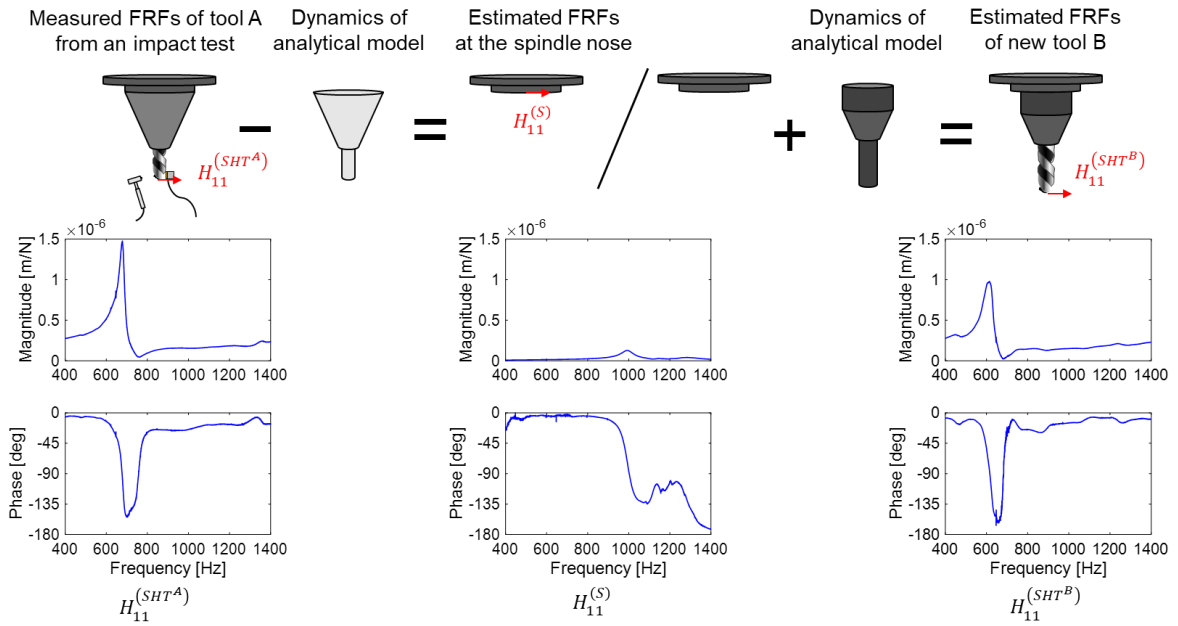


Fig. 1-11 Example of receptance coupling substructure analysis.

1.4.2. Receptance coupling substructure analysis and Timoshenko beam models (TBMs) of composite materials

For the analysis of SLDs, information on machine tool dynamics is required. An impact test under idle conditions is one of the simplest methods to acquire frequency response functions (FRFs) [6], [24], [64]. The layout and mechanical properties of structural materials, especially on machine tool spindle units, strongly correlate with FRFs at the tool tips. Using FEA, the vibration performance of CFRP drive shafts prepared by filament winding with integrated metal flanges under various fiber orientations was validated [65]. The natural frequency of the bending vibration in CFRP drive shafts was found to be higher than that of metals with the same dimensions; this reduced the vibration amplitude [66]. Further, the bending stiffness and radial stiffness of the air spindles were improved by designing a stacking sequence [67]. The enhancement of stiffness and damping properties can contribute to extending stable machining conditions.

Receptance coupling substructure analysis (RCSA) is a renowned semi-analytical method to obtain FRFs for a wide variety of tool types with minimum experimentation [68]–[70]. Figure 1-11 illustrates an example of the procedure of RCSA. After the FRFs of the spindle nose have been obtained from the receptance measurements, the FRFs of the tool tips are obtained by coupling them with the analytically obtained FRFs of another tool coupled with a holder. Therefore, the measurement results can be used without extra measurements and exact structure models. For the analytical models in RCSA, one-dimensional (1D) Euler-Bernoulli models and 1D Timoshenko beam models (TBMs) are

often employed owing to the symmetric structures of the spindles [68], [69], [71]. Dynamic stiffness can be increased by optimizing the interaction between the tool, holder, and spindle nose modes [69]. The analytical models of RCSA are very useful for discussing the interaction and modifying the dynamics.

Beam models can aid in the design development to minimize computational costs [72]. TBMs consider shear deformation and bending deformation and are suitable for analytically obtained FRFs for RCSA owing to the low slenderness ratio of the spindles and its expressiveness over a wide range of frequencies. Many kinematic models have been proposed for laminated composite beams with a basic rectangular cross-section to explain the deformation and stress fields of each layer individually [73], [74]. These advanced models produce accurate deformations and stress for deflections. However, conventional TBMs can achieve sufficient estimation accuracy for resonant frequency in the first vibration mode, which has been confirmed for cantilever beams [75]. The differential equations of advanced models have additional variables, making it difficult to obtain general solutions. Hence, FEA is often employed for vibration analysis. In laminated composite pipes, the formulated bending stiffness is examined by adding a load within the plastic region to several pipe thicknesses [76]. However, parameter identification of mechanical properties focusing on the dynamic stiffness of CFRP spindles are yet to be validated.

The use of general solutions helps avoid solving differential equations with approximate methods. Discussion of the equivalent mechanical properties in TBM improves the reliability of the analysis and performance of the CFRP spindles. Compared with FRA, the models constructed by multi-body system approach using general solutions can quickly provide guidelines for designing CFRP spindle design proposals such as the mechanical design of thermal expansion and static stiffness (Fig. 1-7). Additionally, RCSA has applicability owing to having the translational and rotational coordinates.

1.4.3. Factors causing dynamic property changes on machine tools and chatter avoidance techniques in process

Considerable research has been conducted on stability analysis; however, the prediction of SLDs based on these results may fail. A keynote review indicated machine tool dynamics as the main source of errors in predicting stability during operation (Table 1-2) [6]. It categorized the concepts into gyroscopic effects [71], thermomechanical effects [10], structural joints, and torsional stiffness. Another study reported the effect of the individual bearing properties on a tool point FRF using RCSA, where the bearings were modeled as spring-damper systems [77], [78]. The bearing properties under spindle rotation were identified by an inverse stability procedure using chatter test results [71]. Additionally,

Table 1-2 Main sources of inaccuracies for SLDs [6]

	Concept	Effect of stability
Machine	Gyroscopic effects	Decrease of stability
		Negligible effect
	Thermomechanical effects on bearings	Reduction of chatter frequency
		Decrease of stiffness
		Increase of damping
Process	Torsional stiffness	Variations on stability
	Tool and workpiece contact	Increase of dynamic stiffness
	Moving of the tool outside the workpiece	Lobe shape remains unchanged
	Process damping effect	Increase of stability
	Variable cutting coefficients	Slight variations on stability
	Exact kinematics of milling process	Negligible effect

rotational speed and temperature have been observed to influence the dynamics of recent machine tools for high-speed machining [24]. In another study, FRFs of tool tips were measured with decreasing bearing temperature after stopping the spindle [10]. Gao et al. estimated the resonant frequencies of aerostatic spindles through a multi-physics simulation of the gyroscopic effects and temperature analysis, which included their bearings and cooling systems [79]. Another study compared these estimated resonant frequencies with the measurement results of thin-wall cuttings under varying rotational speeds and preloads [80].

When the process planning fails and chatter occurs owing to these factors, decreasing the depth of cut is a simple countermeasure. However, productivity is drastically detracted by reducing MRR and updating the NC program. Spindle speed is the most flexible process control parameter for altering the process stability. According to the chatter avoidance techniques in process, spindle speed control, which is categorized into discrete spindle speed tuning (DSST) and continuous spindle speed variation (CSSV), is discussed as a function of SOMS [6], [13]. After the detection of the chatter conditions, the spindle speed in DSST is regulated to move the process to the stability pocket. A searching method that iteratively updates the spindle speed until the chatter is diminished has been proposed [81]. This approach allows the oscillation of chatter to detect its condition and produces a failed workpiece. In CSSV, the spindle speed is varied continuously about a nominal spindle speed to disrupt the regenerative effect. To improve the suppression performance, designing the vibration pattern of speed variation is beneficial. However, a very large torque is required at the turnaround points that leads to an increase in the cost, size, and thermal deformation of the machine tool [82]. The design of spindle speed variation requires several time-consuming, expensive, and complex-stability simulations to determine the optimal parameters of the speed and amplitude [6], [83]. Moreover, the operation with high acceleration on spindles decreases the energy efficiency. The priority of the chatter

avoidance techniques is the process planning of SLDs based on reliability assurance.

Although the bearing dynamics have been widely simulated, bearing dynamics models have not yet been constructed from physical measurements. A previous study manually identified bearing properties from the measurements [78]. Dynamical models based on RCSA can implement SLDs at low computational costs. Hence, the analysis of bearing properties based on RCSA is essential to improve the prediction accuracy and convenience of SLDs. The simulation approach cannot define accurate temperature conditions under unsteady states owing to the underlying complex phenomena. Moreover, the energy-saving machining methods will experience further difficulty in the analysis due to the temperature changes in the immediate environment. An understanding of the thermomechanical effects from measurements would contribute to the reliability of model-based control methods. The regression models of the thermomechanical effects have the potential to update SLDs in process. The compensation of SLDs at low computational costs can implement a feed-forward spindle speed tuning as a novel DSST approach, which can maintain productivity.

1.5. Research purpose

Section 1.5.1 summarizes the background and objective of this dissertation. Section 1.5.2 introduces the organization of the dissertation.

1.5.1. Motivations and objectives

The improvement of machining accuracy, productivity, and energy efficiency of machine tools using automation technologies is a desirable goal. Digital twin is a crucial technology of CPSs to install the intelligence on machine tools and are widely discussed in Industry 4.0. The accurate modeling of thermal error and dynamics on machine tools is essential for enhancing the reliability of process control. Based on the mechanical design approaches, thermal error/structural dynamics of machine tools become more complex owing to installing high-power motors, composite materials, and energy-saving machining methods on machine tool spindle units. This research aims to develop CFRP spindle unit models of thermal error, structural dynamics, and temperature-dependent dynamics. The real-time synchronized temperature data is used to update physical information. The combination of IoT systems and kinematic approaches can overcome the limitations of modeling complex phenomena. By compensating for the influence of energy-saving machining methods on thermal errors and dynamics, the desired machining accuracy, productivity, and energy efficiency can be achieved.

IoT systems that can collect considerable sensor information on such complex machine

tool structures can contribute to experimental analysis and modeling of complex phenomena using ML techniques. The components of IoT systems are already in existence, but the network architecture remains flexible. The application of digital twins as SOMS is assumed in each machine tool as edge computing. Control systems in cloud computing can retrofit a wide variety of machine tools after their production in the industry. However, the modeling of complex machine tool structures and industrial networks for digital twins are discussed separately.

This study attempted to construct IoT systems having a considerable number of temperature sensors externally mounted on a CFRPMT, and their information was collected through networks. Moreover, monitoring functions for measurement data and estimation models and a feedback control system through networks are developed. The development of IoT systems can install digital twins of thermal error and dynamics on spindle units through networks. A benchmark of the delay of control systems can be provided.

For high-precision machining, thermal error compensation techniques are required to suppress the influence of thermal deformation. The cooling systems remove lost heat from motors and work to maintain the temperature distribution of machine tools. However, peripheral equipment for cooling, such as chillers, account for the majority of the power consumption of machine tools. Meanwhile, using less peripheral equipment induces larger thermal deformation, resulting in larger thermal errors. The practical use of thermal stability characteristics of CFRP with thermal error compensation techniques can realize energy efficient and high-precision machining.

Thermal errors on CFRPMTs, not only under normal operations but also under idle reduction/from cold start, are measured. The analysis of thermal errors is the first attempt to investigate the effectiveness of CFRP usage. Moreover, thermal error estimation models are proposed using considerable temperature sensor information and ML techniques. For the flexible manufacturing systems where recent machine tools are, thermal error estimation performance under various ambient/initial temperature conditions must be evaluated after work positioning. The effective model construction and the data acquisition for train datasets are discussed. Owing to the difficulty of direct implementation of ML techniques to CNC, the implementation of thermal error estimation through networks is meaningful for the industry as well.

For high-efficiency machining, chatter avoidance techniques are required to maintain machining conditions in high MRR. SLDs can suggest the optimal machining conditions, where the FRFs of the tool tips are needed for the estimation of a stable process. Numerical modeling methods for spindle dynamics can help the mechanical design from the viewpoint of productivity; similarly, an approach for designing linear thermal expansion coefficients

can help static stiffness [11] from the viewpoint of machining accuracy.

In this research, the mechanical properties of CFRP spindle shafts are formulated as a function of the volume ratio or stacking sequence in a uniform cross-section. The parameter identification for TBM facilitates the use of general solutions, which contributes to low computational costs in vibration analysis. Dynamical characteristics of CFRP spindle shafts can be estimated using the information of the dimension and mechanical properties. Moreover, by generalizing receptance coupling, the dynamic properties of the bearings are identified, and the mode shapes are observed.

Additionally, this identification method can experimentally analyze thermomechanical effects on bearings, the accurate estimation of which is difficult in FEA owing to the complex boundary conditions and mechanical properties.

The behaviors of bearing properties under temperature fluctuations can be experimentally analyzed using IoT systems. Based on the development of the regression model for thermomechanical effects and the dynamical model of CFRP spindle shafts, a novel experimental regression model of spindle units considering thermomechanical effects is proposed. The regression models are constructed at the spindle nose, which has high expandability to various holder–tool assemblies by RCSA. Moreover, a novel chatter avoidance technique of DSST is proposed to compensate for the thermomechanical effects on SLDs using the proposed model. This technique has the potential to improve productivity while decreasing the chances of the detection of chatter conditions and failure of the products/machine tools.

1.5.2. Organization of the dissertation

Figure 1-12 summarizes the organization of the dissertation.

Chapter 1 provides an overview of digital twins and their applications in recent machine tools, which is a concept of CPS for addressing manufacturing issues. The state-of-the-art in terms of thermal errors and chatter is summarized to meet the requirements of machining accuracy and productivity. The motivation and purpose of the dissertation are declared by considering the potential of digital twins for CFRPMTs.

In Chapter 2, a temperature analysis environment is developed on IoT systems, which acquire considerable sensor information and contain the computational capacity for ML. Section 2.1 reviews the configuration of the CFRPMT along with the evaluation results of thermal characteristics of each component. Section 2.2 summarizes the system architecture of the temperature analysis environment and the development of the monitoring functions for process information. Moreover, the communication performance of the feedback systems through networks is evaluated in Section 2.3. Section 2.4 summarizes the development of

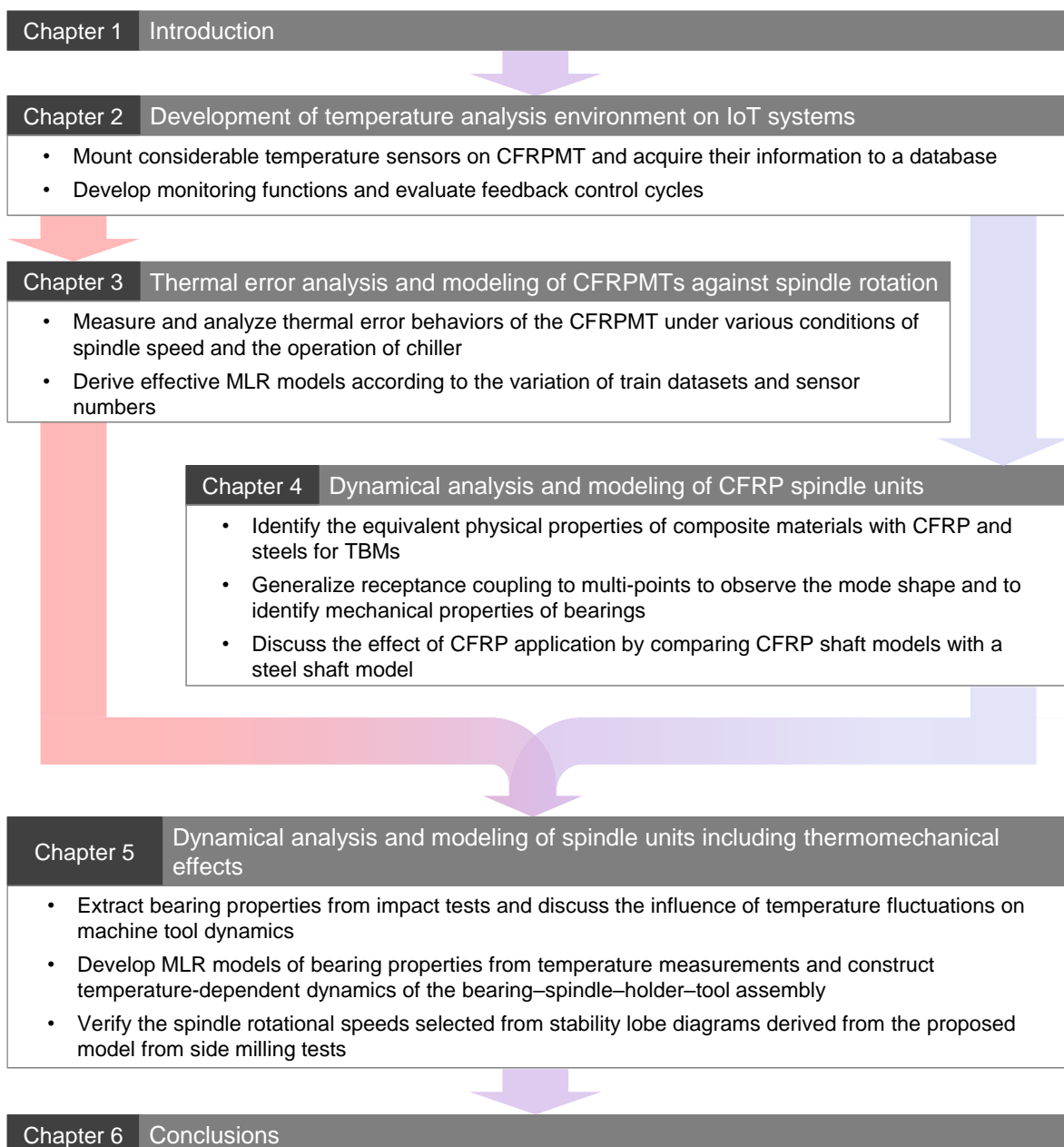


Fig. 1-12 Diagram of the organization of the dissertation; the novelty with the proposals is listed in bullet point format.

the temperature analysis environment.

In Chapter 3, thermal errors on the CFRPMT are analyzed and modeled. Section 3.1 shows the experimental setup for thermal error measurement under various operations of the spindle and chiller. The measured data are labeled for analysis and modeling. The behaviors of thermal errors are analyzed using temperature measurements in Section 3.2. The results indicate the influence of the energy-saving machining method and the use of CFRP for machine tool structures. Section 3.3 proposes MLR models for thermal errors and analyzes temperature measurement points by principal component analysis. The

estimation performance is evaluated using test data acquired during the operation of the energy-saving machining methods in Section 3.4. The appropriate models and effective number of datasets for the learning process are also discussed. Section 3.5 summarizes the thermal error analysis and modeling of the CFRPMT.

Dynamical models of CFRP spindle units are developed in Chapter 4. Section 4.1 reviews kinematic models of TBM and proposes the formulation of the equivalent mechanical properties of CFRP spindle shafts for TBMs. In Section 4.2, multipoint receptance coupling is proposed to identify bearing properties and observe mode shapes. The FRFs and mode shapes of a CFRP spindle shaft of the developed models are measured and compared in Section 4.3. The dynamical models of the CFRP spindle unit are developed by combining the spindle shaft models with bearing properties. Section 4.4 shows the identification of bearing properties by impact tests, improvement of dynamics, and superior mechanical design of CFRP spindle shafts by changing the layout of CFRP. Finally, Section 4.5 summarizes the dynamical analysis and modeling of CFRP spindle units.

In Chapter 5, the influence of thermomechanical effects on bearings is analyzed by considering the measurement results of thermal errors in Chapter 3 and by using the developed dynamical model in Chapter 4. Section 5.1 comprises the proposal of an experimental modeling method of the thermomechanical effect on bearings and machine tool dynamics. In addition, its application to SLDs and a novel DSST design for the chatter avoidance are proposed. Impact tests are conducted under temperature fluctuations caused by spindle rotation, and the behaviors of machine tool dynamics based on the bearing properties identification are discussed in Section 5.2. Section 5.3 consists of the modeling of thermomechanical effects on bearings using temperature information as inputs. Dynamical models of thermomechanical effects on bearings and CFRP spindle units are validated by impact tests in Section 5.4. Side milling tests are conducted to validate the proposed models that the changes of SLDs are predicted by temperature measurements in Section 5.5. Finally, Section 5.6 summarizes the analysis and modeling of thermomechanical effects on bearings.

Chapter 6 concludes the dissertation.

2. Development of temperature analysis environment on CFRPMT and IoT systems

2.1. Prototype CFRPMT

The CFRPMT employed in this research is introduced in this section. Figure 2-1 shows the CFRPMT. Table 2-1 shows the mass of each feed axis and the inertia of each rotational axis. Table 2-2 shows the motor ratings and motion space. Each element was designed to realize a static stiffness equivalent to that of conventional steel, so that the structure weight was drastically reduced by using CFRP.

In the development phase of the CFRPMT, the thermal expansion of each element was evaluated in comparison with elements in the BaseMT. The shaft of the main spindle configures five-layer types manufactured by filament winding process, oriented at the angles 0° , 30° , -30° , $\pm 30^\circ$, and $\pm 45^\circ$ with respect to the center axis. When the spindle was rotated at 12000 min^{-1} for 250 min, the axial thermal expansion of the main spindle unit was reduced to 35% [11]. The ram maintained a symmetrical structure by adopting CFRP plates in the rolled steel rectangular pipes. The thermal expansion in the feed axis direction was reduced by 30% under the environment temperature change from 20 to 28 °C for 8 h [84]. The saddle with a slider consisted of CFRP plates and aluminum alloy casting to achieve further weight reduction. The 30% reduction of the thermal expansion in Z-axis was estimated by the FEA under the heat generation related to X- and Z-axis feed motion [84]. Because the column and the bed were fixed elements, dynamic stiffness was further improved by using CFRP plates having four-layer types, oriented at the angles 0° , 45° , -45° , and 90° , on the outside and resin concrete (REC) on the inside, which has high damping properties. The appropriate filling rate and arrangement of REC were determined by FEA. As well as the damping ratio in first frequency mode was 73% improved, the thermal expansion in the Z-axis direction was reduced by 20% under the environment temperature change from 20 to 28 °C until being a steady value [84]. The ball screw used CFRP shaft inserted in steel pipes. The positioning errors on one side under repeating full stroke feed motion with related structures weight were reduced by 69, 66 and 57% on related X-, Y- and Z-axis direction, respectively [85]. The C-axis spindle uses CFRP shaft mainly orientated at parallel to the rotational axis, and the stage part uses isotropic molding CFRP. The thermal expansion in the rotational axis direction was reduced by 62% under switching rotation on 300 min^{-1} for 3 h. The cradle of the A-axis turning table uses CFRP plate to reduce the inertia of the parts away from the rotation axis. When the turning table was rotated for 3 h, the thermal expansion in the direction normal to the plane was reduced by 54%.

The above results confirmed that each element to which CFRP was applied had

2. Development of temperature analysis environment on CFRPMT and IoT systems

improved thermal characteristics owing to the mechanical design technologies. For high-precision machining, it is important to evaluate the thermal errors between the tool and workpiece in a CFRPMT that consists of these advanced elements. The dynamic properties must be evaluated because the priority of mechanical design is static stiffness and thermal expansion.

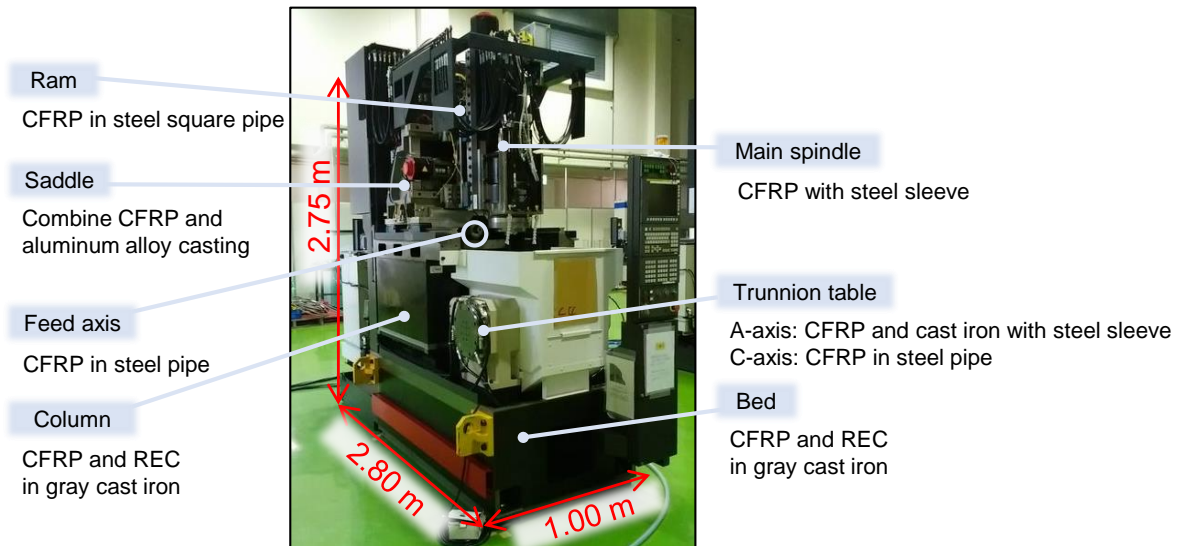


Fig. 2-1 Configuration of CFRPMT using new structural materials.

Table 2-1 Structures weight

Axis	Base machine	CFRP machine tool
X-axis mass	950 kg	710 kg
Y-axis mass	2050 kg	1190 kg
Z-axis mass	600 kg	490 kg
A-axis inertia	2.8 kgm ²	1.9 kgm ²
C-axis inertia	0.22 kgm ²	0.15 kgm ²
Spindle shaft inertia with rotor	0.026 kgm ²	0.020 kgm ²

Table 2-2 Motor specifications

Axis	Travel	Rated power
X-axis feed	340 mm	2.5 kW
Y-axis feed	300 mm	2.7 kW
Z-axis feed	230 mm	4.5 kW
A-axis rotation	-	2.4 kW
C-axis rotation	-	3.7 kW
Spindle rotation	-	26 kW

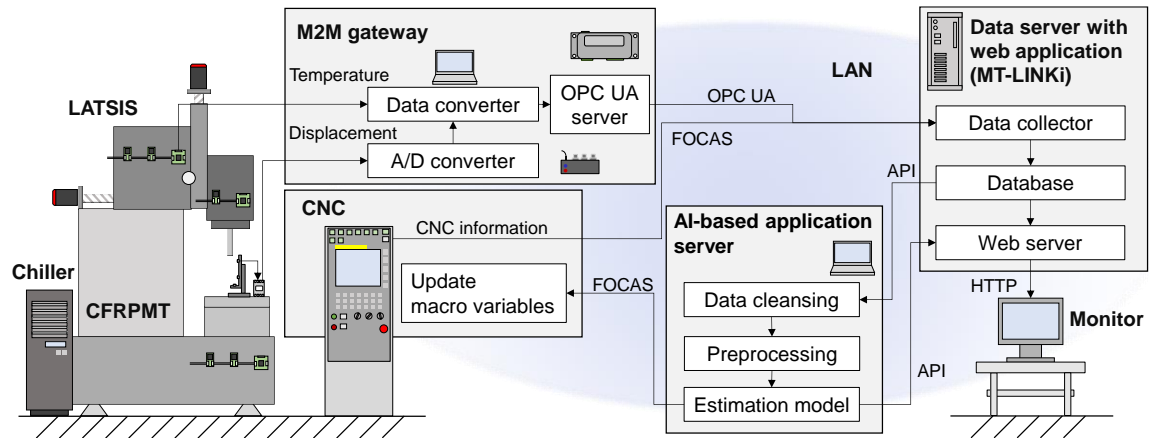


Fig. 2-2 System architecture of temperature analysis environment.

2.2. Construction of temperature analysis environment

IoT systems that incorporate client-server systems offer the advantages of expandability and flexibility based on same communication interface. The system architecture of the IoT systems is illustrated in Fig. 2.2. It comprises a CNC (31i MODEL B5, FANUC) for the CFRPMT, a M2M gateway for LATSIS and displacement sensors, a data server with a web application, and an application server for installing AI technologies. This section introduces the components of the developed temperature analysis environment.

2.2.1. Introduction to large-scale array of temperature sensors interconnected in series (LATSIS) and temperature measurements on the CFRPMT

With the progress of embedded system and sensing technologies have progressed, several temperature sensors can be installed without requiring the use of many ports for analog to digital conversion on equipment. LATSIS is a temperature measurement system that can serially connect to up to 200 microcontrollers (MSP430FR2355, Texas Instruments) with sensors in a line [52]. Each microcontroller reads sensor signals, communicates with neighboring sensors to define their own ID, and sends sensor information with its ID at 0.1 Hz. Three hundred contact temperature sensors (TMP102, Texas Instruments) and two infrared sensors (MLX90615, Melexis) were mounted on the CFRPMT. Further, the temperature sensors were divided into three LATSIS based on the machine configuration: the spindle unit, saddle, and fixed elements such as the bed and column.

Figure 2-3 shows the representative measurement points of temperature sensors. Temperature sensors are covered thermally conductive silicon with electromagnetic

2. Development of temperature analysis environment on CFRPMT and IoT systems

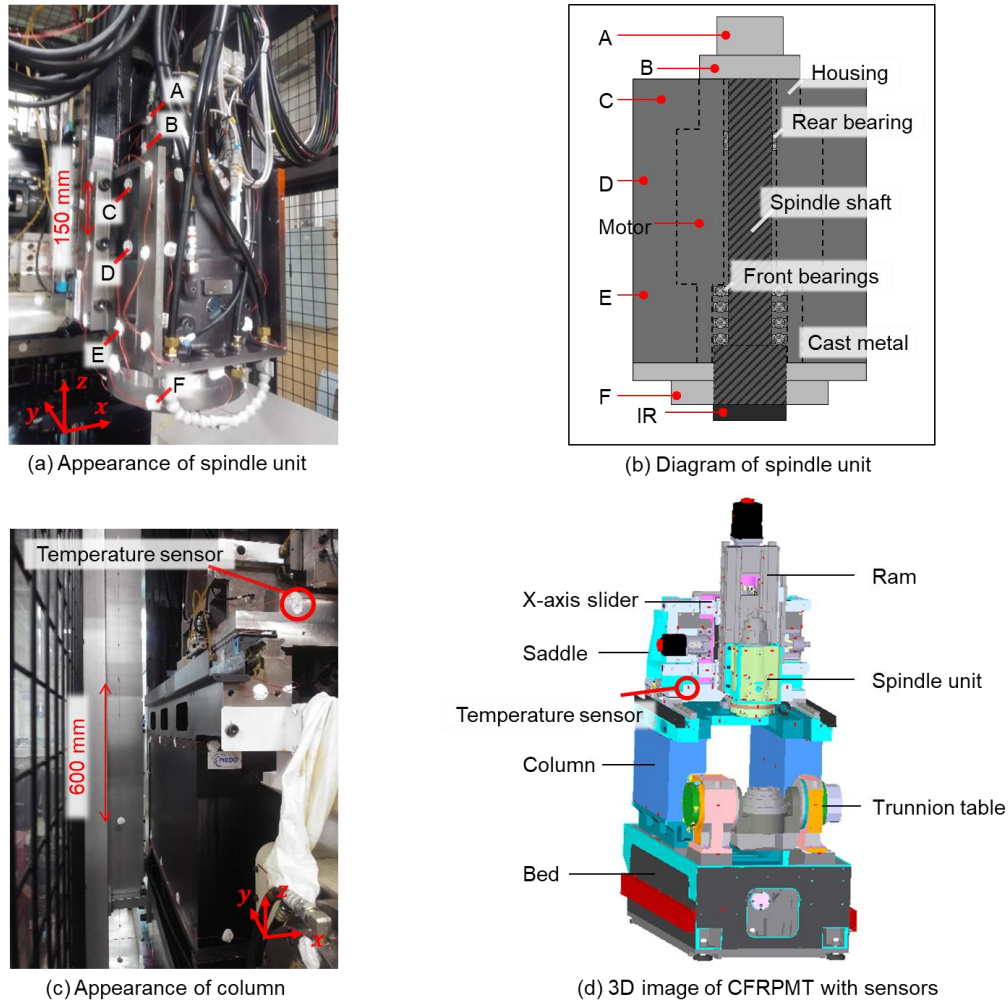


Fig. 2-3 Representative measurement points of temperature sensors.

shielding. As show in Fig. 2-3(b), the representative points of temperature sensors on spindle unit are labeled as A to F from the rear side to monitor and discuss thermal distribution. The spindle nose was painted as a black body, and its temperature was measured via two infrared sensors labeled “IR.” The pitches of the mounted sensor array positions were approximately 150 mm around the spindle unit, ball bearings, and linear guides, and 300 mm around the other components. In addition, 20 sensors for ambient temperature were hung from the four corners inside the exterior with 600 mm of the pitch, labeled “Room”, as shown in Fig. 2-3(c). The temperature measurement points of LATSIS are summarized in Appendix A.

2.2.2. Machine to machine gateway for LATSIS and displacement sensors

Each LATSIS was developed to send sensor signals in asynchronous serial

Table 2-3 Specifications of the measurements on database

Signal	Unit	Source	Equipment	Accuracy	Resolution	Sampling cycle [s]
Temperature	°C	Contact temperature sensors	LATSIS	0.5	0.065	10
Temperature	°C	Infrared sensors	LATSIS	0.5	0.02	10
Temperature	°C	Build-in sensor of spindle motor	CNC	-	1	0.5
Rotational speed	min ⁻¹	Pulse coder	CNC	-	1	0.5
Displacement	μm	Eddy current sensors	A/D converter	0.3	0.1	60

communication of the TTL level. The sensor signals in the hexadecimal number were sequentially conveyed in descending order of identification numbers (IDs). To perform the displacement measurements, eddy current sensors (HA-30S, SENTEC) with amplifiers (LS-500, SENTEC) were employed. Further, the analog signals were converted to digital data using an analog to digital (A/D) converter (NR-500 and NR-HA08, KEYENCE). In addition, sampled displacement data was saved on intermediate files in comma separated value (CSV) format at 1 min intervals.

For the transmission of data to the data server, an OPC UA server on a Linux computer (CPS-MC341-ADSC1-931, CONTEC) was employed. The referenced nodes, referred to as tags in the OPC UA, contained the data for the responses of specific HTTP requests. A Windows computer (PC-GN276FSG9, NEC) received signals from three LATSIS and read an intermediate file in parallel, converted the units of temperature signals to degrees Celsius, and then transmitted the temperature data through asynchronous serial communication of RS-232C, whose pre-processing was developed in a programming language (Python 3.9, Python Software Foundation). Each tag corresponding to an ID on the OPC UA server was successively updated to the current temperature data at 0.1 Hz and current displacement data at 0.017 Hz.

2.2.3. Data server with web application for monitoring

The data server collected data from the OPC UA server and CNC. A commercial IoT platform (MT-LINKi, FANUC) was created on a Windows computer (EliteDesk 800 G5 DM, HP). This platform collected data through the OPC UA, MTCConnect, and FOCAS. Therefore, CNC information, including the machine status, axes positions, spindle speeds, etc., was collected without the need for an additional server. The collected data were labeled as per

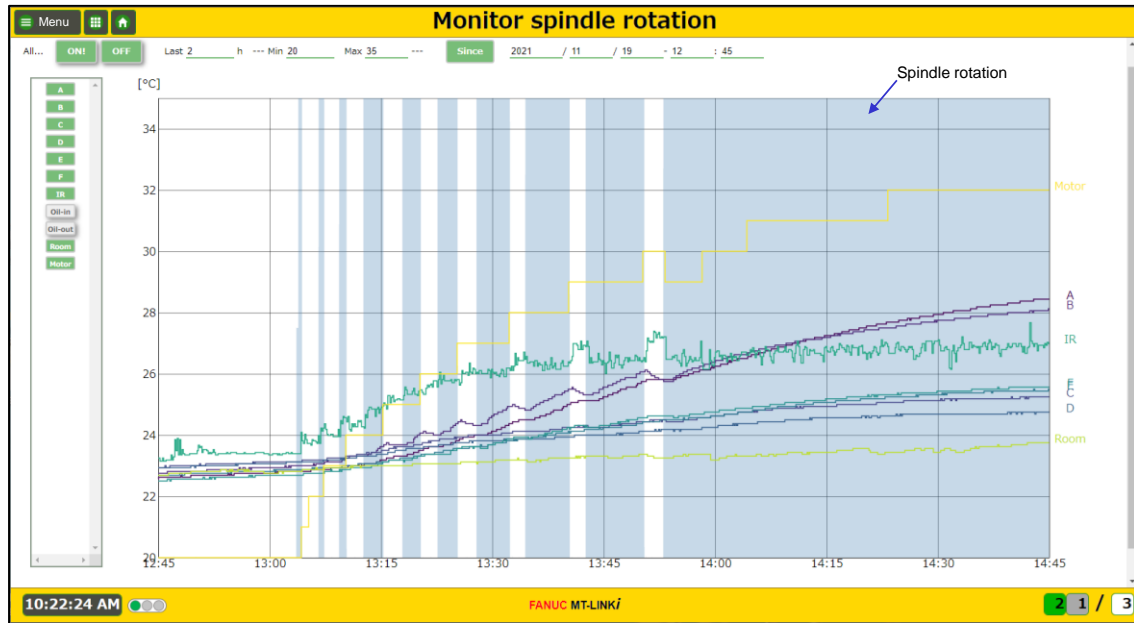


Fig. 2-4 A monitoring page for representative temperature signals on spindle units.

the information model and stored with a timestamp in a database (MongoDB 3.6, MongoDB). Further, the temperature analysis environment was defined as a group “Group-CFRPMT,” which comprised two devices of the OPC UA server as “CFRPMT-CONTEC” and CNC as “CFRPMT-CNC.” Table 2-3 summarizes the specifications of the measurements on the database through networks. Temperature and displacement data as along with the CNC information were continuously stored in the database and selectively output to CSV files.

Another function of the platform was a web server based on an execution environment (Node.js 10.16, Node.js Developers), with an API for reading the stored data. Figure 2-4 shows a web page for monitoring temperature signals, which was developed using HTML with JavaScript and CSS. The temperature data could be selected, be rescaled, and were monitored on the local area network (LAN) of The University of Tokyo and/or via remote access through the Internet.

2.2.4. Artificial intelligence-based application for estimation and feedback control

An AI-based application was executed on a Windows computer (ENVY Laptop 15-ep1000, HP). An API server was developed in the programming language, Python 3.9. Selected data for estimation models was read from the database through API requests. The current and previous data underwent data cleansing to remove outliers caused by electrical noise on temperature sensors. In data preprocessing, the time series data was arranged for datasets to be used for running estimation models as inputs. The API server provided

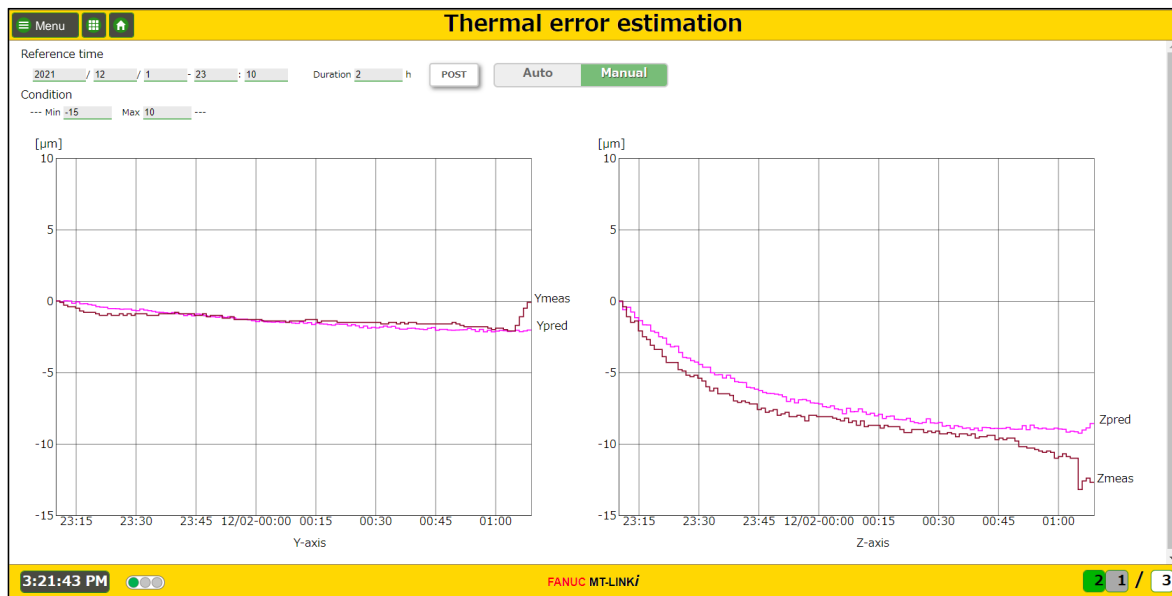


Fig. 2-5 A monitoring page for thermal error estimation.

estimation values as relative displacement from reference points at reference time, which was set by reading the change of sequence number of CNC programs and through API requests manually. Figure 2-5 shows a web page running real-time thermal error estimation against measurement results as an example. The estimation models in Fig. 2-5 are discussed in Chapter 3.

Macro variables in CNC are often used for keeping the machining information such as work coordinates, tool length, and so on. The AI-based application continuously updates macro variables for the compensation values calculated by estimation models. This feedback function is developed in Python 3.9 with FOCAS libraries. The revision history of macro variables is also stored in the database on the data server.

2.3. Communication performance of the temperature analysis environment

The control systems in machine tools require reliable communication with admissible latency. The admissible latency is a few microseconds for motion control, such as high-precision positioning [86], and a few minutes or more for process control. Thermal deformation is a semi-static phenomenon and is measured in intervals of 3[87], 5[88], [89], and 15 [90] min. Additionally, estimation models are evaluated every 8 h to update model parameters as SOMS [89]. Recent industrial automation employs considerable equipment and moving machines, such as autonomous mobile robots. The use of wireless communication can reduce wiring effort and integrate dynamic systems [91]. For installing

2. Development of temperature analysis environment on CFRPMT and IoT systems

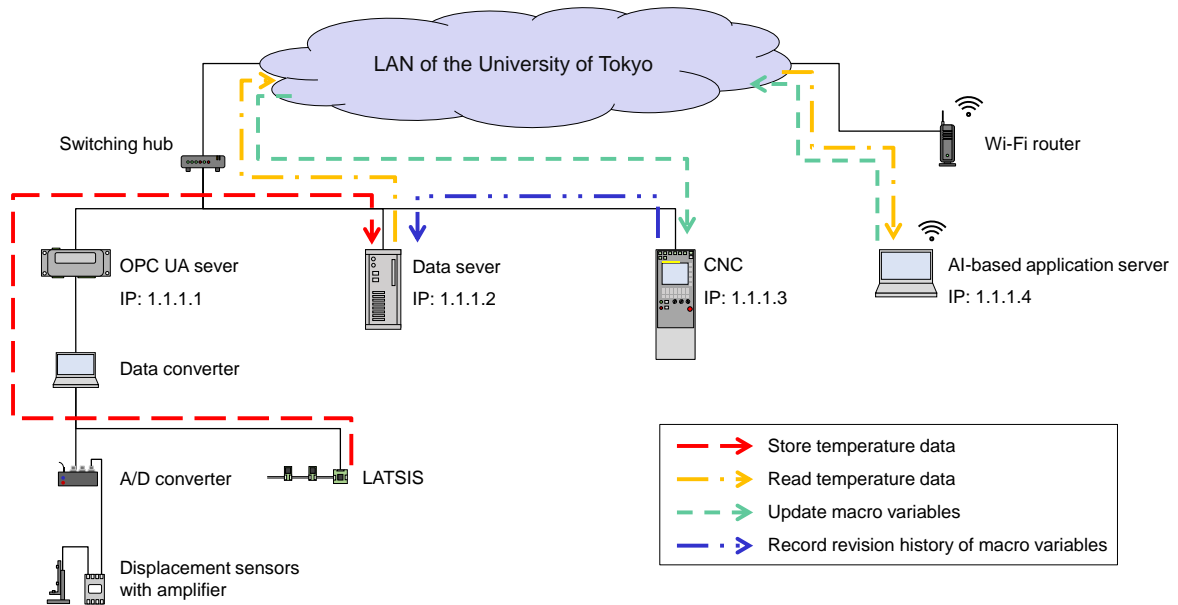


Fig. 2-6 Physical network diagram with communication paths of temperature data.



Fig. 2-7 Experimental setup of the control cycle measurement of the temperature analysis environment.

the intelligence on AI-based application servers, the communication performance of the temperature analysis environment is evaluated.

Figure 2-6 shows the physical network diagram of the temperature analysis environment. IP addresses are assigned for four equipment in the LAN. The temperature data measured by LATSIS is stored in the database on the data server. The AI-based application server reads the stored temperature data. After the calculation of the compensation values, macro variables are updated. The data server also recodes the revision history of macro variables.

According to the communication performance, the temperature data are used for the evaluation. Figure 2-7 shows the experimental setup. A temperature sensor of LATSIS was placed on a hot pack and an ice pack. The time of switching locations between the hot and

2. Development of temperature analysis environment on CFRPMT and IoT systems

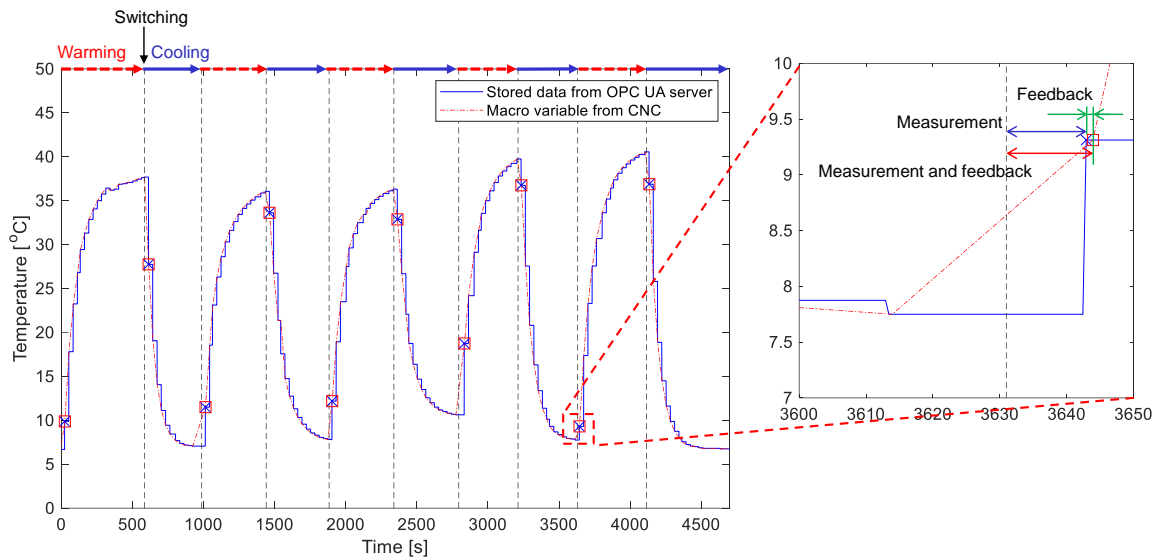


Fig. 2-8 Measurements of temperature data on the data server.

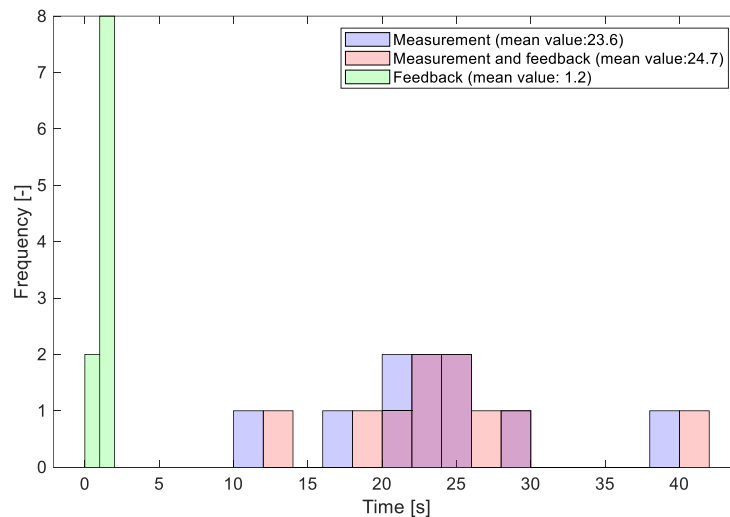


Fig. 2-9 Distribution of the delay of the measurement and feedback.

ice packs is measured on the system time of the data server. In this experiment, the AI-based server preprocesses the temperature data, but updates macro variables to current temperature values without running the estimation. Therefore, the data server records the time of switching locations, temperature data from the OPC UA server, and temperature data from CNC. The locations are switched 10 times.

Figure 2-8 shows the time series of the temperature data. Note that the responsibility of temperature changes is evaluated by the measurement results, not the thermal resistance of the silicon and contact. After switching locations, the first increase or decrease of the temperature is marked when the sensor was warming or cooling. According to the enlarged figure, the duration of the temperature change from the OPC UA server responds

to the delay of the measurement and that of the macro variable from CNC responds to the delay of the measurement and feedback. The difference between the two durations is the delay of the feedback control of the AI-based application server. Additionally, temperature gradually changes to saturation values, which requires more than 5 min. The characteristics of heat conduction and heat transfer of temperature sensors must be considered during the measurements.

Figure 2-9 shows the distribution of the delay of the measurement and feedback. The mean values of the delay are shown in the legends. The measurement delay vibrates owing to the responsibility and sampling cycle of LATSIS. Heat is conducted to the sensor chip, and the sensor measures temperature in every 10 s. In the seventh measurement, having the longest measurement delay at 38.7 s, two samples are contained so that the value of the first sampled data does not increase. Owing to the measurement process on the M2M gateway, the mean value of the measurement delay becomes more than 20 s. According to the feedback delay, the mean value is 1.2 s, and updating macro variables has low variability. The total delay of the measurement and feedback is 24.7 s on average. The communication performance of networks is sufficient against thermal deformation. However, the responsivity of the sensors should be considered while constructing digital twins.

2.4. Summary

This chapter describes the development of a temperature analysis environment on CFRPMT and IoT systems as a platform of digital twins. The contents are summarized as follows.

- The CFRPMT is constructed by machine tool elements using CFRP. Each element is designed to realize a static stiffness equivalent to that of conventional steel and is confirmed to be a smaller thermal expansion coefficient in target directions.
- The temperature analysis environment comprises four components: the CNC, the M2M gateway, the data server, and the AI-based application server. 302 temperature sensors of LATSIS were externally mounted on a CFRPMT. Temperature data, displacement data, and CNC information are collected to the data server through the LAN at 0.1 Hz, 0.017 Hz, and 2 Hz, respectively. Several monitoring pages for current signals and estimation results are developed on the data server. The AI-based application server accesses the database of the data server by API requests and processes the data by regression models using ML techniques to estimate the conditions of the CFRPMT (e.g. thermal errors). Moreover, the AI-based application server is used for providing API to return

2. Development of temperature analysis environment on CFRPMT and IoT systems

estimation results and for updating macro variables to construct feedback control systems. The developed temperature analysis environment runs for measurement, data acquisition, data storage, computerization, and feedback in real-time.

- The communication performance of the temperature analysis environment is evaluated by the response of temperature fluctuations. The total delay of the measurement and feedback is 24.7 s on average.

3. Thermal error analysis and modeling of CFRPMTs against spindle rotation

3.1. Thermal error measurement according to spindle rotation and idle conditions

For high-precision machining by CFRPMTs supposing flexible manufacturing systems and energy-saving machining methods, thermal error behaviors under significant temperature fluctuations must be discussed. By the temperature analysis environment developed in Chapter 2, thermal errors of the CFRPMT against spindle rotation are measured under various ambient/initial temperature conditions for the analysis and modeling.

Figure 3-1 shows the experimental setup for thermal error measurement. A test bar with bottle grip taper shank was attached to the main spindle, and displacement sensors were attached to the jigs made of super Invar. Figure 3-1 shows the spindle rotational speeds as experimental conditions. Constant rotational commands were provided for 2 h to collect train datasets. Under the idle conditions after stopping spindle rotation, the machine tool waited for 3 h with the chiller either being stopped (idle reduction) or in operation (standby). This measurement cycle was repeated for two weeks and the measurement from cold start was conducted three times. The datasets under a stepwise change of rotational

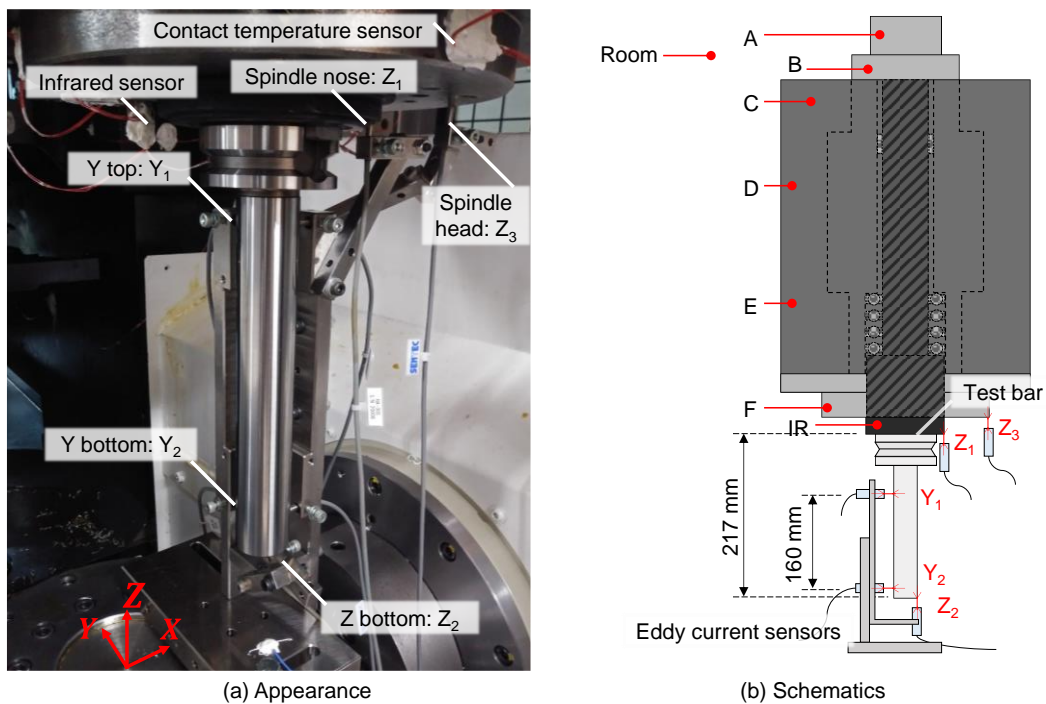


Fig. 3-1 Experimental setup for thermal error measurement.

3. Thermal error analysis and modeling of CFRPMTs against spindle rotation

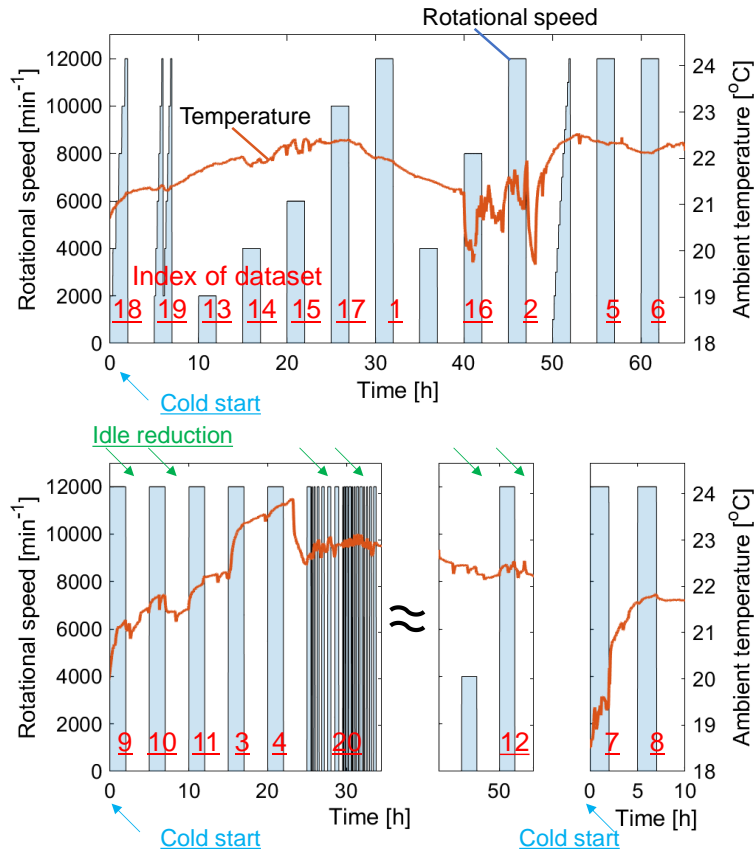


Fig. 3-2 Spindle rotational speed and temperature Room during thermal error measurement.

speed and switching spindle rotation were collected for the validation of estimation models. Table 3-1 summarizes the experimental conditions for the thermal error analysis and the estimation model construction and validation. Each dataset was numbered according to the conditions of spindle rotation and previous operation as the index. Thermal errors in the X-axis were less than $5 \mu\text{m}$ in a dataset and had minimal influence because the CFRPMT had symmetrical designs when viewed from the front.

3.2. Thermal error analysis of CFRP spindle unit

Thermal expansion of spindle units is among the largest sources of thermal errors. To install energy-saving machining methods, thermal error measurement was conducted under various operation condition of the cooling system and the consequent thermal error behaviors was discussed.

3.2.1. Thermal error behaviors against cold start and idle reduction

Figure 3-3 shows the measurement results at spindle rotational speed of 12000 min^{-1} .

3. Thermal error analysis and modeling of CFRPMTs against spindle rotation

Table 3-1 Experimental conditions according to dataset

Index	Spindle rotational speed [min ⁻¹]	Previous rotational speed [min ⁻¹]	Operation of the cooling system	Usage
1	12000	10000	-	Train
2	12000	8000	-	Train
3	12000	12000	-	Train
4	12000	12000	-	Train
5	12000	From 1000 to 12000 by 1000	-	Train
6	12000	12000	-	Train
7	12000	-	Cold start	Train
8	12000	12000	2 nd operation from cold start	Train
9	12000	-	Cold start	Train
10	12000	12000	2 nd operation from cold start, after idle reduction	Train
11	12000	12000	3 rd operation from cold start, after idle reduction	Train
12	12000	4000	After idle reduction	Train
13	2000	From 2000 to 12000 by 2000 ×2	-	Train
14	4000	2000	-	Train
15	6000	4000	-	Train
16	8000	12000	-	Train
17	10000	6000	-	Train
18	From 2000 to 12000 by 2000	-	Cold start	Test
19	From 2000 to 12000 by 2000 ×2	From 2000 to 12000 by 2000	2 nd operation from cold start	Test
20	Switching 0 to 12000	Switching 0 to 12000	Idle reduction while stopping spindle rotation	Test

The index of datasets was from 1 to 12 and the reference point of relative displacement was set at the start of each dataset.

The results in green lines represent datasets 1 to 6 of those collected after more than 10 h, that is 2 measurement cycles from cold start. Displacement Z_2 of datasets 2 and 3 indicates the difference compared to the others. Figure 3-4 shows the thermal expansion in the Z-axis direction and temperature values of dataset 2. Temperatures A and B show the

3. Thermal error analysis and modeling of CFRPMTs against spindle rotation

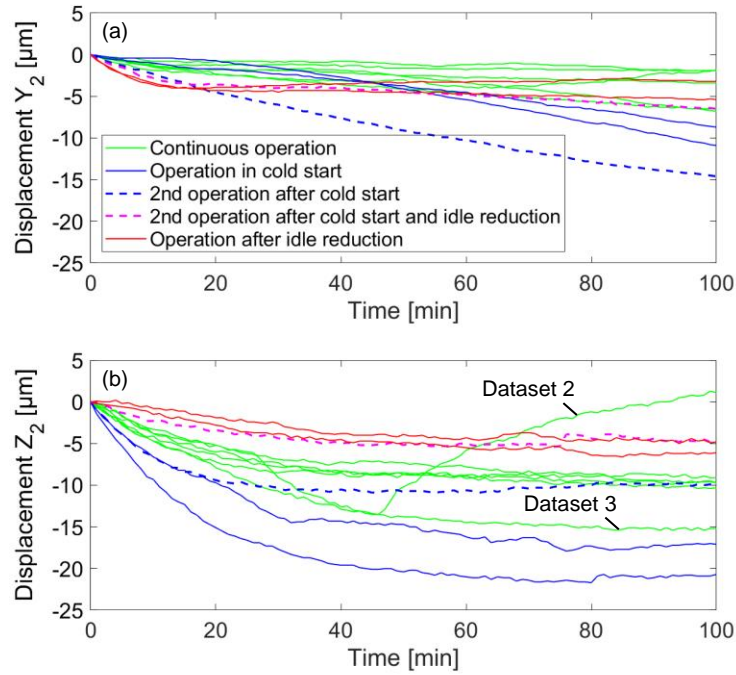


Fig. 3-3 Thermal errors at the TCP (a) in the Y-axis direction; (b) in the Z-axis direction at 12000 min^{-1} according to previous operation.

saturation values after 60 min. However, the behavior of Z_3 corresponded to temperature C–F mounted on cast metal. Further, displacement $Z_3 - Z_1$ explains the thermal expansion of structures between the spindle nose and front cover, which was approximately $5 \mu\text{m}$ in 10 min. The time constant of CFRP spindle shaft with bearings was smaller than that of cast metal and housing. In addition, displacement $Z_1 - Z_2$ explains the thermal expansion and contraction of the test bar, which is highly correlated to temperature Room as well as temperature IR. Z_2 of dataset 3 also shows the influence of increasing the ambient temperature by $1 \text{ }^\circ\text{C}$ during the operation, as shown in Fig. 3-2. In contrast, the other datasets exhibited highly reproducible behavior when temperature Room did not fluctuate.

The results in blue lines were for those collected from cold start in Fig. 3-3. Thermal errors in the Z-axis direction were larger than under other experimental conditions. The blue dashed line shows the largest thermal errors in the Y-axis direction. From cold start, the thermal expansion in the Y-axis direction exhibited a delay of approximately 20 min. Thereafter, thermal errors were proportional to time. This behavior was saturated after 2 measurement cycles.

The results in red lines indicate the measurement after idle reduction. Thermal errors in the Z-axis direction were suppressed within $5 \mu\text{m}$ in 60 min. However, the displacement of $5 \mu\text{m}$ in $-Y$ -axis occurred in 15 min. Figure 3-5 shows the inclination $Y_2 - Y_1$ of the test bar. The design of the spindle unit assumes continuous use of the cooling system. Therefore, the inclination in $-A$ -axis became almost twice as large after idle reduction. In previous

3. Thermal error analysis and modeling of CFRPMTs against spindle rotation

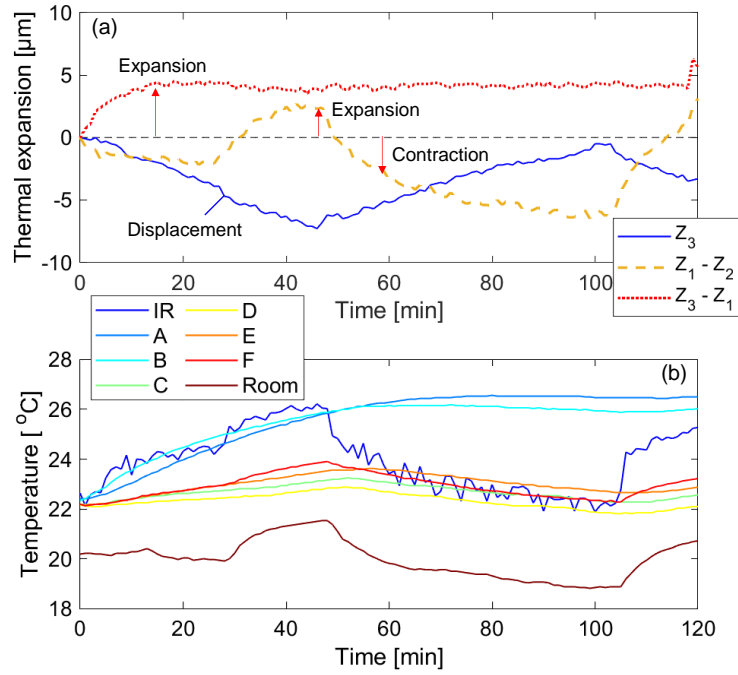


Fig. 3-4 (a) Thermal expansion in the Z-axis direction; (b) Temperature around the spindle unit on dataset 2.

research [37], thermal errors of a 5-axis machine tool were measured after idle reduction and standby. Thermal errors were reduced; however, unique behavior such as that when using CFRPMT was not observed. Idle reduction on CFRPMTs effectively retained generated heat and maintained its dimensions.

Cold start without warm-up operation induces large thermal errors. Gradually, thermal errors in $-Y$ -axis occur, despite reaching a steady state of thermal errors in $-Z$ -axis. Idle reduction can compensate for the decrease of thermal errors in the Z-axis direction and enable efficient warm-up of spindle units. However, compensation techniques based on control and mechanical design are required.

3.2.2. Thermal error behaviors against spindle rotational speed

Figure 3-6 shows the thermal errors according to spindle rotational speeds. Datasets 13 to 17 and dataset 1 are shown. Through comparisons between displacement Z_1 and Z_2 at low-speed rotation (2000, 4000, and 6000 min^{-1}), thermal errors were observed to occur within 3 μm and were mainly affected by ambient temperature. The results of displacement Z_2 at high-speed rotation (8000, 10000, and 12000 min^{-1}) indicated that the thermal errors became larger than those at low-speed rotational speed, and the saturation values were correlated to rotational speeds. The tendency of thermal errors in the Y-axis direction was

3. Thermal error analysis and modeling of CFRPMTs against spindle rotation

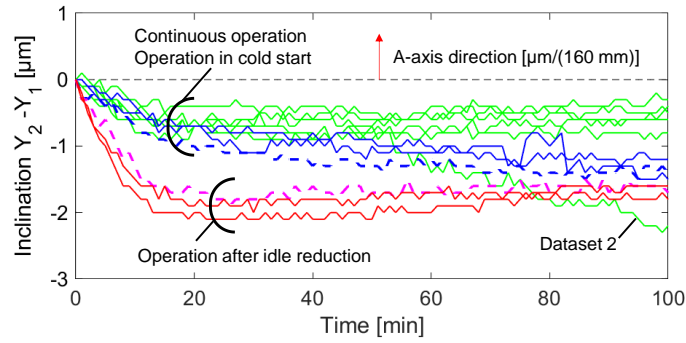


Fig. 3-5 Inclination of the test bar (legend of lines is same to Fig. 3-3).

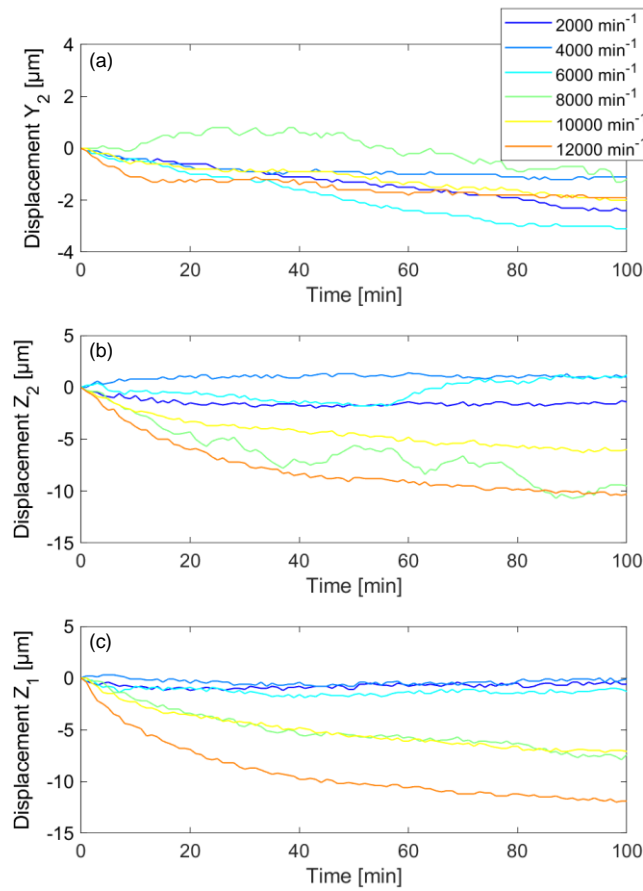


Fig. 3-6 Thermal errors according to spindle rotational speed (a) at the TCP in the Y-axis direction; (b) at the TCP in the Z-axis direction; (c) at the spindle nose in the Z-axis direction.

similar to that under other conditions, as shown in Fig. 3-3. Following the warm-up of the CFRPMT, thermal errors in the Y-axis direction became stable and small operation time-dependent behavior was observed.

For the learning process of estimation models, datasets only under high rotational speeds have the potential to develop sufficient models. Moreover, the fluctuation of the length of the test bar must be considered.

3.3. Development of regression models of thermal errors

Machine learning can modify the relation between inputs and outputs from train datasets without defining kinematic models. Therefore, the applications of machine learning can be expected to compensate for the negative impacts of energy-saving machining methods on complex thermal error behaviors. However, the performance of machine learning models is highly dependent on datasets, data cleansing, and data preprocessing. In this study, simple regression models based on MLR and considerable temperature sensors were developed to estimate thermal errors at the TCP. Before evaluating the performance through comparisons of the number of train datasets and sensor signals, the effectiveness of temperature measurement points is discussed.

3.3.1. Data cleansing of temperature and displacement data

The data server stores temperature and displacement data from the OPC UA server with timestamps. If a failure of the measurement occurred, the values of tags were not updated on the M2M gateway. However, electronic noise was rarely observed on the voltage values of temperature sensors. Consequently, the measured temperature data was not used and previous values were used when the variation was over the threshold value of 1 °C.

Displacement data experiences a jump when the spindle rotation command on/off is switched because of the deformation caused by rotatory inertia. The measured displacement data was offset by the variation from the previous values when the variation was over the threshold value of 3 μm .

As shown in Table 3-1, the longest sampling cycle of all data on the developed thermal analysis environment was 60 s of displacement data. Other data was down-sampled to 1 min. Thus, from the above data cleansing and data preprocessing results, each dataset had 300 training instances.

3.3.2. Deployment of multiple linear regression (MLR) models for thermal error estimation

The thermal error estimation in the entire time from start-up machine tools is required especially in the case of different idle time for waiting and setup operation on each workpiece in job scheduling. For high-precision machining in such a flexible manufacturing system, relative TCP errors from the reference position obtained after work positioning are discussed. MLR is known as a machine learning technique; however, it functions as a statistical approach assuming a linear relationship between inputs and output. To realize

3. Thermal error analysis and modeling of CFRPMTs against spindle rotation

uniform applicability against various datasets and long-term estimation, the relative displacement from the previous sample is estimated by MLR models, as expressed in Equation (3-1)

$$\Delta p^j = \mathbf{b}^T \Delta \mathbf{T}_k = \{b_0 \quad \dots \quad b_{n_s}\} \begin{Bmatrix} 1 \\ \Delta T_{1,k} \\ \vdots \\ \Delta T_{n_s,k} \end{Bmatrix} \quad (3-1)$$

Relative displacement Δp_j in and temperature $\Delta T_{i,j}$ of i -th sensor in a sample k are the difference data from the previous sample. Further, n_s indicates the amount of sensor information used in MLR models. To obtain appropriate coefficients \mathbf{b} , the minimization problem of the difference between the model and measurement is defined as expressed in Equation (3-2).

$$S_{cf} = \frac{1}{n_w} \sum_{k=1}^{n_w} (\mathbf{b}^T \Delta \mathbf{T}_k - \Delta p_{j,meas}) \quad (3-2)$$

Here, n_w is the number of instances in train datasets. Against Equation (3-2), the normal equation is known as shown in Equation (3-3).

$$\mathbf{b} = (\mathbf{T}^T \mathbf{T})^{-1} \mathbf{T}^T \Delta \mathbf{p}_{meas} \quad (3-3)$$

where,

$$\mathbf{T} = [\Delta \mathbf{T}_1 \quad \dots \quad \Delta \mathbf{T}_{n_w}] \quad (3-4)$$

$$\Delta \mathbf{p}_{meas} = \{\Delta p_{1,meas} \quad \dots \quad \Delta p_{n_w,meas}\}^T$$

Thermal error estimation values are accumulated relative displacement predicted by data from a reference time, as shown in Equation (3-5)

$$R_p = \sum_{k=1}^{t_c} \Delta p_k \quad (3-5)$$

In this study, the models labeled as Y_2 and Z_2 were directly learned relative displacement behaviors from temperature data as inputs. From the analysis in Section 3.3, thermal errors in the Z-axis direction are highly affected by ambient temperature change. Hence, measured thermal expansion $Z_1 - Z_2$ was also trained by using 20 of temperature

3. Thermal error analysis and modeling of CFRPMTs against spindle rotation

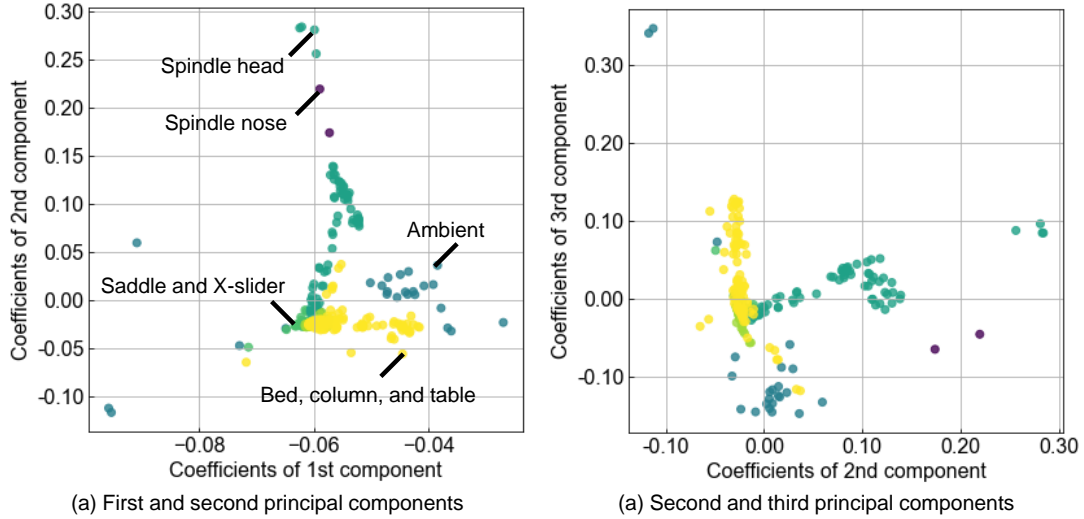


Fig. 3-7 Results of principal component analysis for 302 points of temperature changes in the datasets.

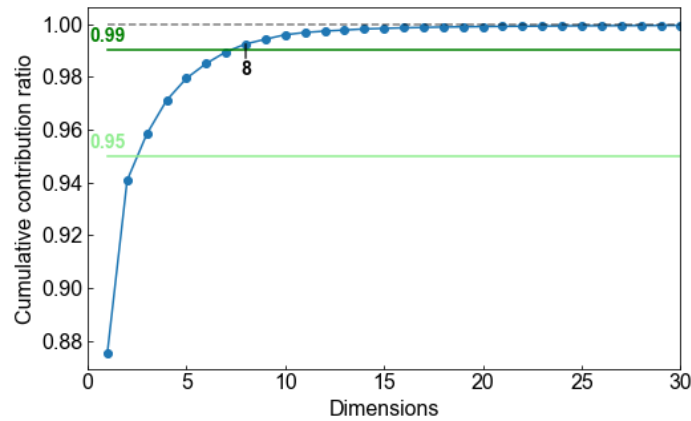


Fig. 3-8 Cumulative contribution ratio of temperature changes.

Room, 2 of temperature IR, and spindle rotational speed. The model labeled as $Z_1 + TL$ was constructed by the estimation models of test bar length and at spindle nose for each as follows: the predicted length $Z_1 - Z_2$ was subtracted from predicted displacement Z_1 after developing two MLR models.

3.3.3. Discussion of temperature measurement points based on principal component analysis

Principle component analysis is a dimensionality-reduction method for analyzing large datasets with a statistical procedure. Principal components are basis vectors determining hyper-planes in the same number of dimensions as the datasets. Obtained principal components from the covariance matrix of the datasets approximate in the least squares

3. Thermal error analysis and modeling of CFRPMTs against spindle rotation

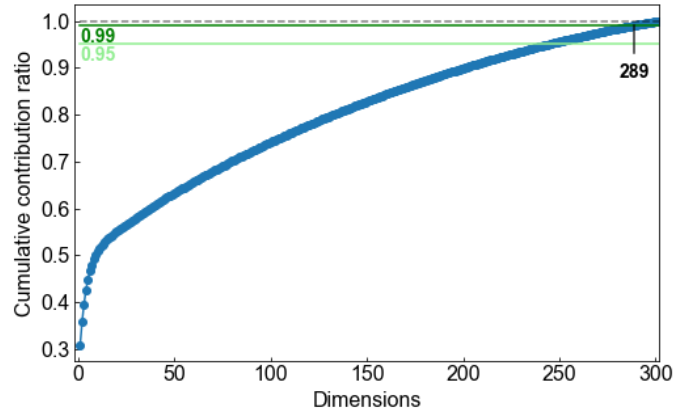


Fig. 3-9 Cumulative contribution ratio of relative temperature in 1 min.

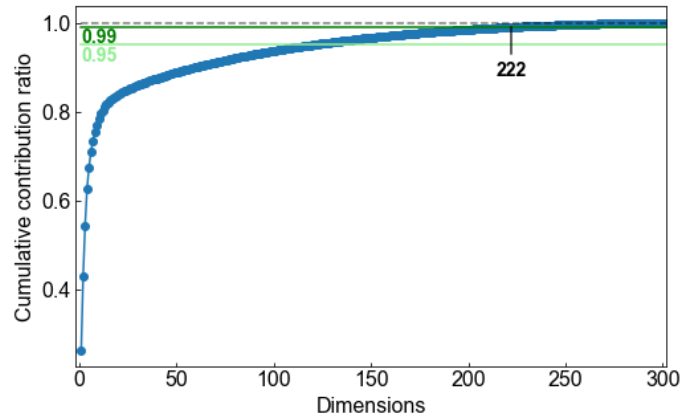


Fig. 3-10 Cumulative contribution ratio of relative temperature in 5 min.

sense. 20 of the datasets in Table 3-1 are analyzed by using a programming library, scikit-learn 0.24.2.

Figure 3-7 shows the results of the principal component analysis. The first, second, and third principal components have larger values against measurements on the spindle unit and ambient. Temperature distribution on the CFRPMT is mainly generated by spindle rotation and ambient temperature changes. Figure 3-8 shows the cumulative contribution ratio of the datasets. The dimensions of the datasets can be reduced to 8, which can explain 99% of temperature information. Most temperature behaviors are similar to others, owing to the measurement conditions generated by the two main heat sources.

Besides, the proposed regression models use relative temperature. Figure 3-9 shows the cumulative contribution ratio in principal component analysis for relative temperature whose time interval is 1 min. The dimensions of relative temperature behaviors are 289. Most temperature sensors have individual temperature gradients. When the time interval is changed to 5 min, the dimensions decrease to 222 as shown in Fig. 3-10. Temperature

3. Thermal error analysis and modeling of CFRPMTs against spindle rotation

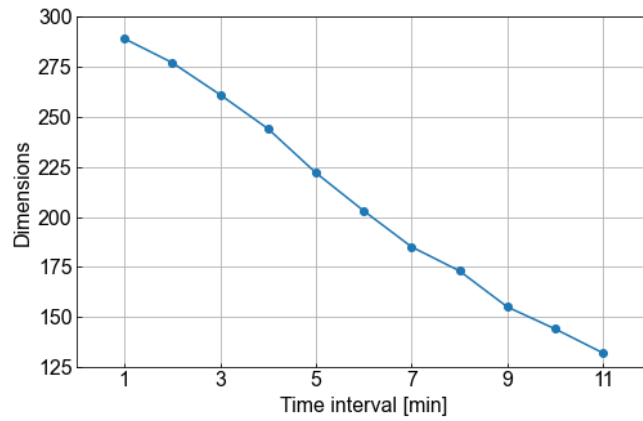


Fig. 3-11 Dimensions having 99% of cumulative contribution ratio according to time intervals of relative temperature.

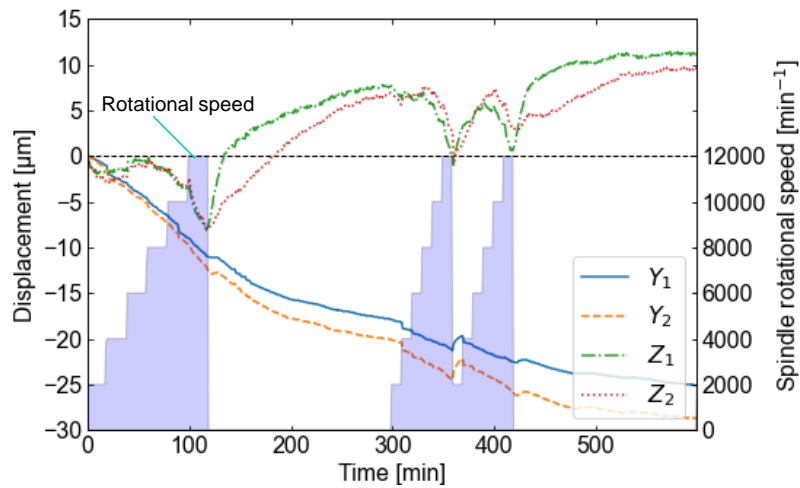


Fig. 3-12 Thermal errors after cold start on datasets 18 and 19.

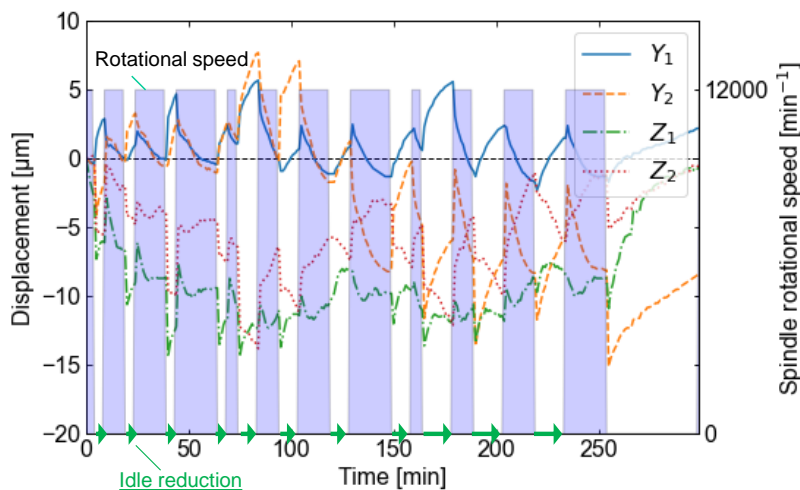


Fig. 3-13 Thermal errors under idle reduction on dataset 20.

3. Thermal error analysis and modeling of CFRPMTs against spindle rotation

sensors close to other sensors have the same temperature gradients if the time interval changes to longer.

Figure 3-11 shows the dimensions having 99% of cumulative contribution ratio according to time intervals of relative temperature. The dimensions have decreasing trend from short to long time intervals. Temperature measurement points are enough to install estimation models in previous research. However, considerable temperature sensors must be installed if temperature distribution measurement is required in high frequency. The proposed models to estimate thermal errors every 1 min can effectively use the information of almost temperature sensors.

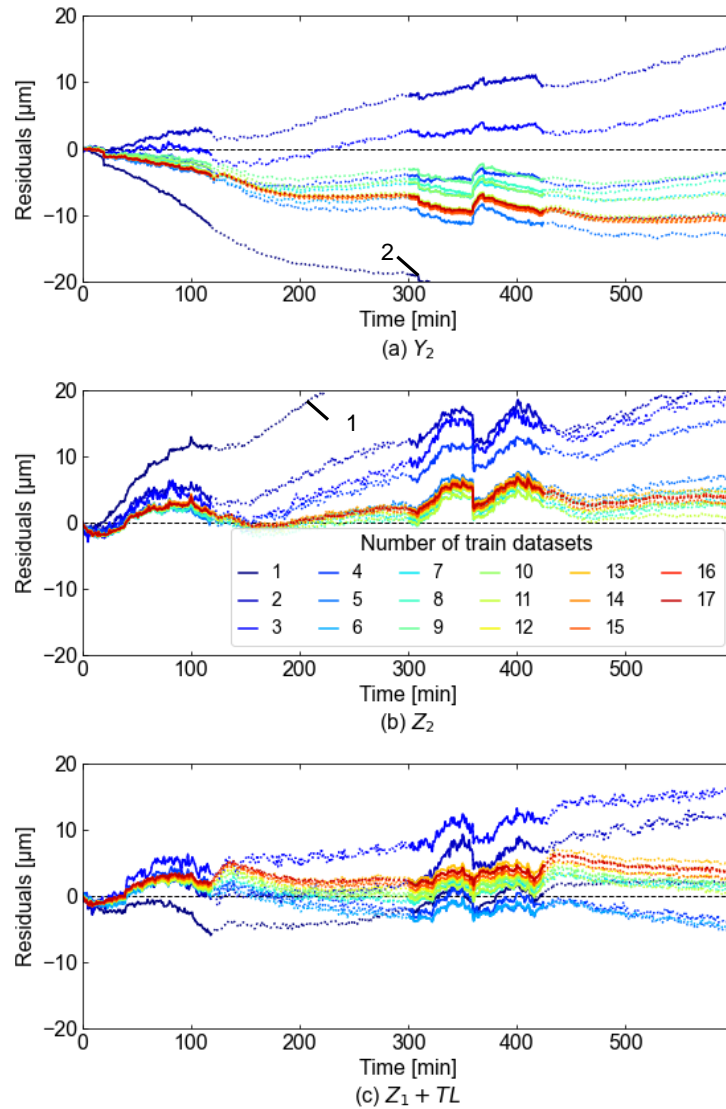


Fig. 3-14 Residuals of thermal error estimation on datasets 18 and 19 in each estimation model.

3.4. Performance evaluation of regression models

Figure 3-12 shows thermal errors from cold start on datasets 18 and 19 when spindle rotational speed was varied from 2000 to 12000 min^{-1} in steps of 2000 min^{-1} at 20 min and 10 min intervals twice, respectively. Figure 3-13 shows thermal errors under idle reduction. Spindle rotation for 5, 10, 15, and 20 min at 12000 min^{-1} and the idle conditions for 5, 10, and 15 min under idle reduction were repeated in order. The above test datasets including data under the idle conditions were evaluated.

The estimation models must be developed with low costs, through less use of train datasets and sensor information. Figure 3-14 shows examples of residuals subtracted from measurement values at cold start, where the structure of estimation models was fixed while the number of train datasets was changed. In the evaluation, data cleansing for displacement data of test datasets was not performed. Solid parts of lines indicated the operation of spindle rotation, and dotted parts indicate the idle conditions. The order to be used for the train datasets corresponded to the index in Table 3-1. The performance of thermal error estimation converged according to the number of train datasets. Therefore, three properties of residuals at the solid parts are evaluated:

- Mean value
- Maximum value
- Root mean square error (RMSE)

Moreover, the number of temperature sensors used in the models Y_2 , Z_1 , and Z_2 was reduced at random while maintaining its order.

3.4.1. Performance evaluation against cold start machining

Figure 3-15 shows the properties of residuals on datasets 18 and 19, with varying number of train datasets using all temperature sensors. It can be concluded that the estimation models need not use train datasets from cold start. A large number of train datasets deteriorates the performance, which is a result of low sensitivity caused by overfitting owing to the train datasets. Mean values and RMSE are similar because thermal error estimation experiences difficulty at the start and residuals remain. The performance of model $Z_1 + \text{TL}$ was better than that of model Z_2 , in the case of using small number of datasets. Further, the thermal error behavior at the spindle nose exhibited high reproducibility and the division of models against ambient temperature worked well.

Figure 3-16 shows the properties of residuals on datasets 18 and 19, with varying number of temperature sensors using all train datasets. Model Y_2 can estimate thermal

3. Thermal error analysis and modeling of CFRPMTs against spindle rotation

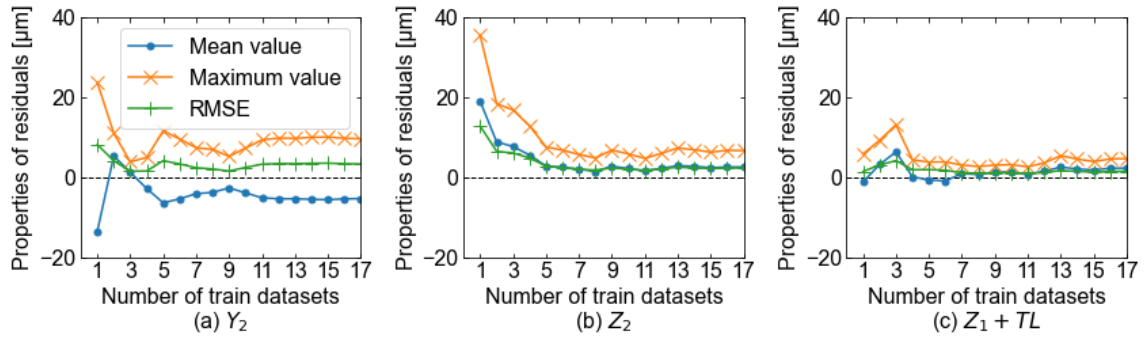


Fig. 3-15 Performance evaluation of thermal error estimation at cold start according to the number of train datasets in each estimation model.

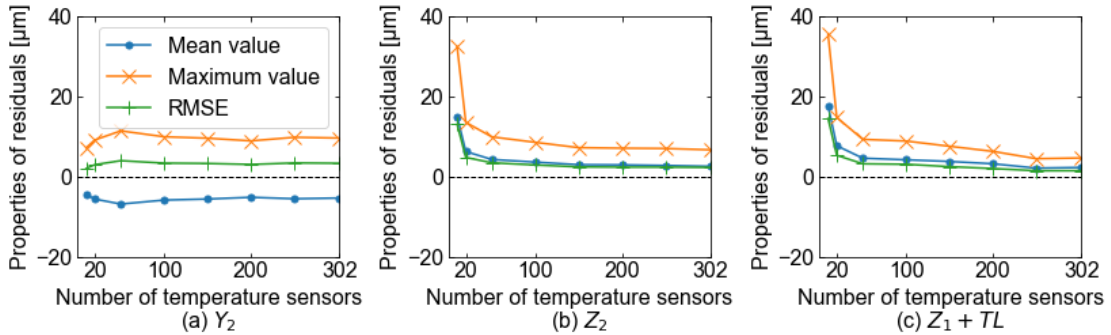


Fig. 3-16 Performance evaluation of thermal error estimation at cold start according to the number of temperature sensors in each estimation model.

errors despite a small number of sensors, because of the linear tendency of thermal errors in the Y-axis direction.

Figure 3-17 summarizes the maximum values of residuals at cold start according to the use of datasets. The contour of $10\ \mu\text{m}$ is projected in green dashed lines. Model $Z_1 + \text{TL}$ exhibited a larger blue area, implying the efficiency and robustness for the learning process. In the development of estimation models for machining at cold start, the information from 302 sensors is sufficient to construct estimation models. However, large train datasets, such as validating spindle rotational speed dependence, are not required. Figure 3-18 shows maximum values when the index of train datasets is changed to the increasing order of spindle speeds. The train datasets measured under spindle rotation $2000\text{-}10000\ \text{min}^{-1}$ are firstly used for the estimation models, in contrast to the order in Table 3-1 and Fig. 3-17 firstly using the train datasets measured under spindle rotation $12000\ \text{min}^{-1}$. The estimation performance gradually increases with the increase of the number of train datasets. Remarkably, the minimum area of maximum values around nine of the train datasets in Fig. 3-17 disappears in Fig 3-18. The relative displacement is estimated by the integral value of the product of relative temperature and its coefficient. To obtain effective

3. Thermal error analysis and modeling of CFRPMTs against spindle rotation

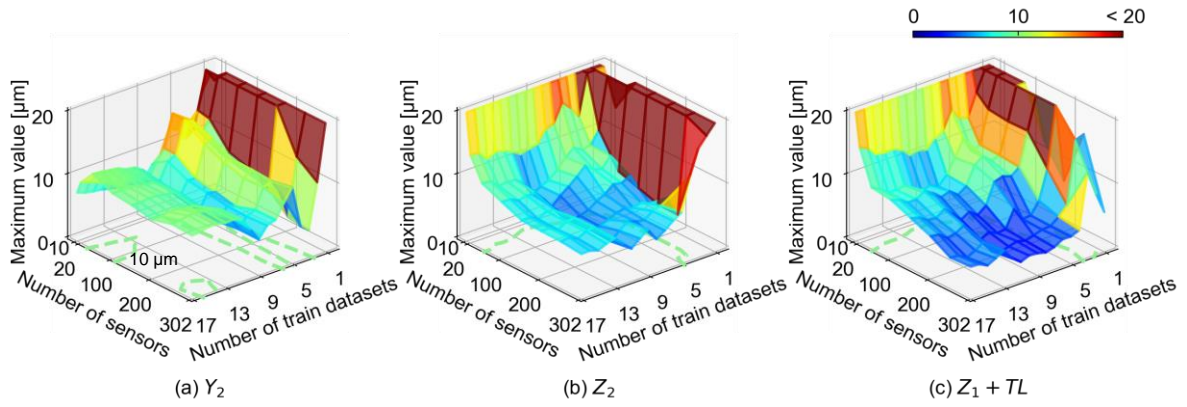


Fig. 3-17 Maximum values of residuals at cold start according to the use of datasets in each estimation model.

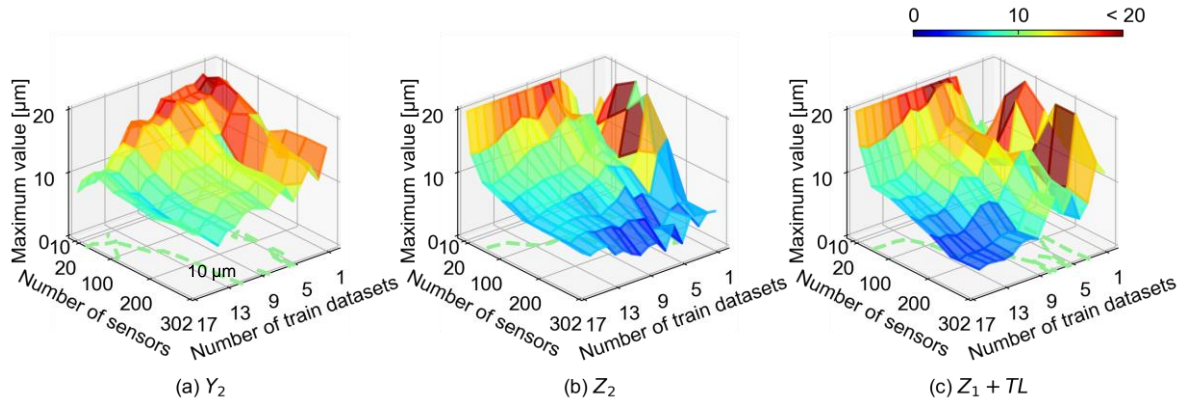


Fig. 3-18 Maximum values of residuals at cold start when the index of train datasets is changed to the increasing order of spindle speeds.

coefficients by MLR, train datasets measured under the fastest spindle rotation are worth reducing the number of train datasets.

3.4.2. Performance evaluation against idle reduction of cooling system

Figure 3-19 shows the residuals of thermal error estimation on dataset 20 while conducting idle reduction. The local peaks of residuals corresponding to thermal errors because of switching operation were suppressed with the increase in the use of datasets. Figure 3-20 shows the properties of residuals on dataset 20, for varying number of train datasets using all temperature sensors. Compared to that in Fig. 3-15 at cold start, train datasets after idle reduction helped in the improvement of the performance. Further, the necessity of datasets 13 to 17 was minimal and was similar to the results for cold start.

3. Thermal error analysis and modeling of CFRPMTs against spindle rotation

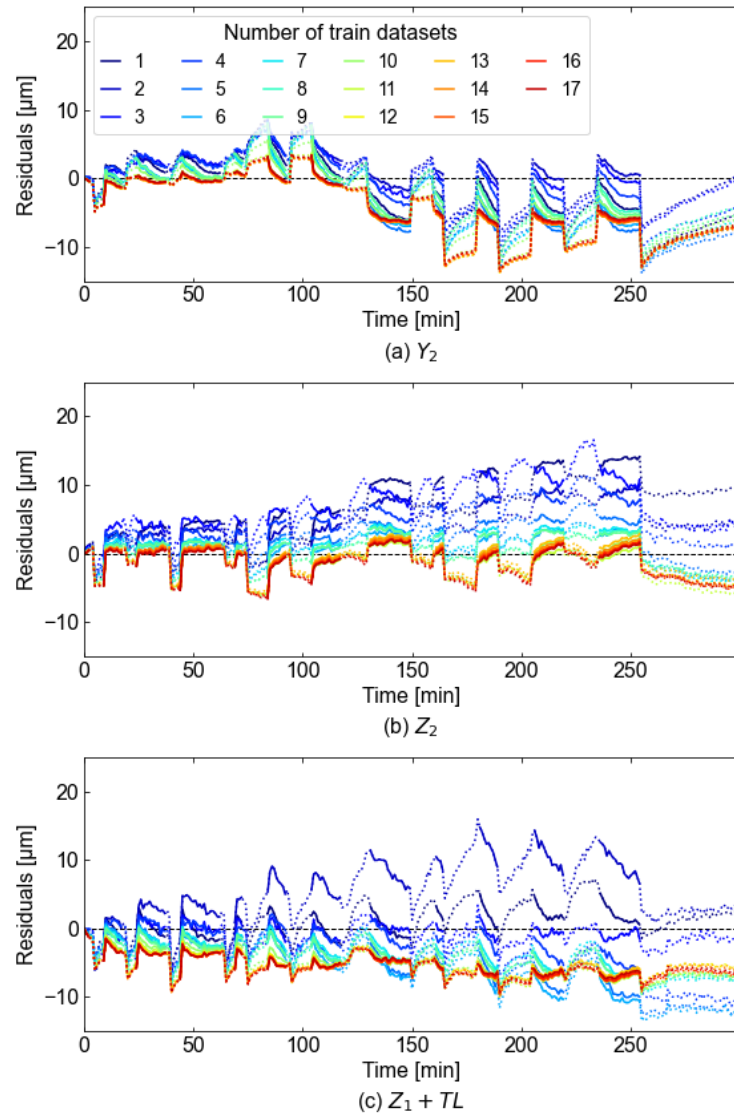


Fig. 3-19 Residuals of thermal error estimation on dataset 20 in each estimation model.

Figure 3-21 shows the properties of residuals on dataset 20, with varying number of temperature sensors using all train datasets. The estimation performance of model Y_2 and $Z_1 + TL$ deteriorates when the number of temperature sensors increases in spite of the improvement against cold start machining as shown in Fig. 3-16. It is considered that these models have difficulty to learn short-term temperature fluctuation from train datasets.

Figure 3-22 summarizes the maximum values of residuals under idle reduction according to the use of datasets. The improvement of models Y_2 and $Z_1 + TL$ are found to be saturated. Moreover, the effective number of sensors was under half of the total number. This can be attributed to the influence of multicollinearity in MLR. The reduction of explanatory variables is expected to improve the estimation quality. However, the switching operation was not included in train datasets and frequently induces unsteady states on thermal deformation. Further, change in the measurement of train datasets was also

3. Thermal error analysis and modeling of CFRPMTs against spindle rotation

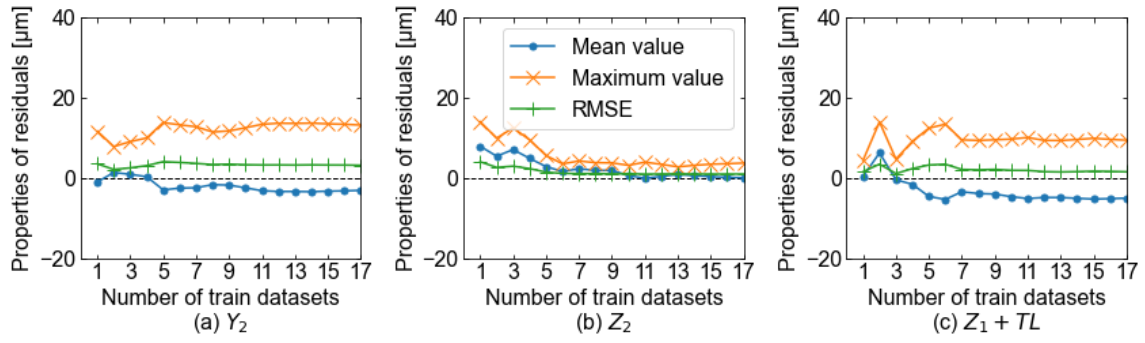


Fig. 3-20 Performance evaluation of thermal error estimation at cold start according to the number of train datasets in each estimation model.

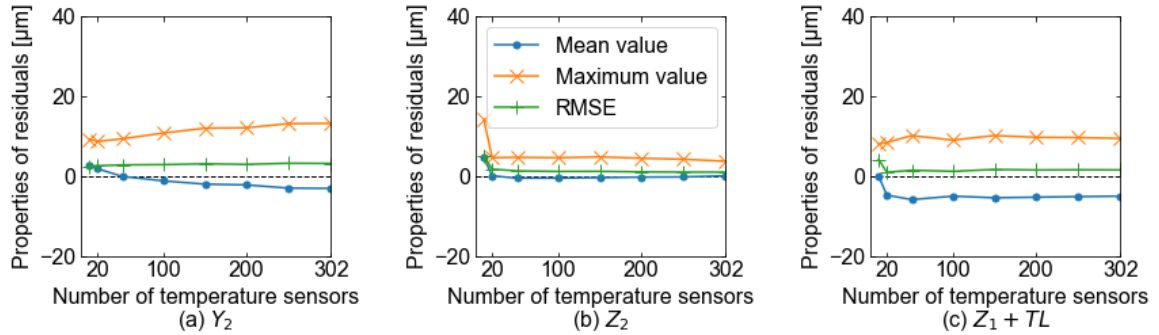


Fig. 3-21 Performance evaluation of thermal error estimation at cold start according to the number of temperature sensors in each estimation model.

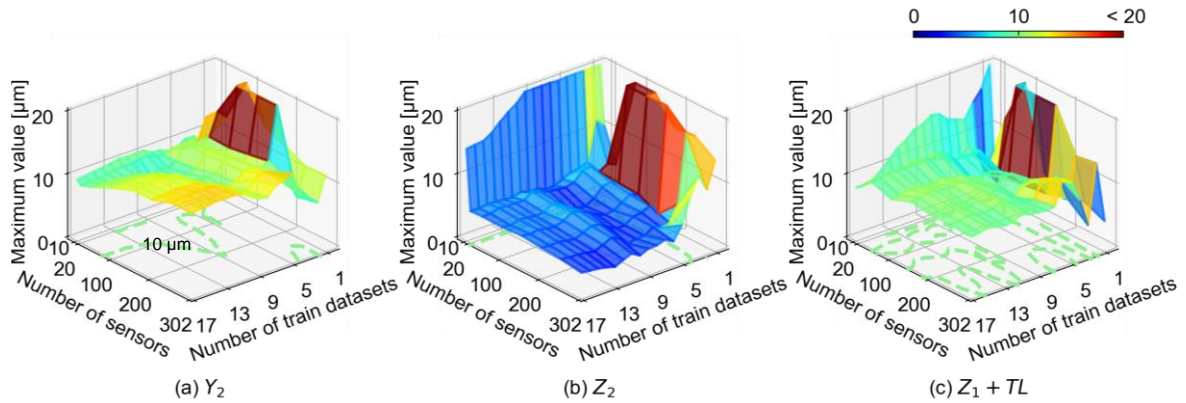


Fig. 3-22 Maximum values of residuals at cold start according to the use of datasets in each estimation model.

considered. Moreover, the performance of model Z_2 exhibited a certain correlation with the number of sensors. The increase in the number of sensors, as well as sensor installation inside structures, will be considered to improve the performance.

Thus, thermal errors on CFRPMTs were estimated through simple regression models

and LATSIS. With the progress of information and communication technologies, the reliability of estimation models can be improved by using considerable sensor information at low costs. Especially, the estimation accuracy after work positioning is required for flexible manufacturing systems. Although the estimation models integrate the relative values every 1 min, the residuals can be within 10 μm against the test datasets measured for 7 h. Particularly on the machine tools having complex mechanical characteristics, clear models based on sensing actual phenomena are advantageous to the implementation in industries. Moreover, data acquisition operating at a maximum speed is efficient to construct sufficient MLR models. This measurement procedure can reduce the cost of model construction.

3.5. Summary

This chapter describes thermal error analysis and modeling of the CFRPMT against spindle rotation. Considering the implementation of two energy-saving machining methods, thermal error measurement using a test bar was conducted by repeating spindle rotation for 2 h. The contents are summarized as follows.

- 8 temperature and 5 displacement sensors were selected for the experimental analysis of thermal errors. Cold start induced larger thermal errors in the Z-axis direction and the increase in proportion to time in the Y-axis direction.
- Spindle rotation after idle reduction can suppress thermal errors to 5 μm in the Z-axis direction; however, twice as large inclination in $-A$ -axis was observed compared with that after the idle condition using the cooling system. The different behaviors of thermal errors must be considered in the development of estimation models as well as mechanical design.
- The principal component analysis reveals the effectiveness of temperature measurement points on the CFRPMT. The time behavior of measured temperature against spindle rotation and ambient temperature changes can be expressed in eight dimensions. However, more than 289 temperature sensors at 1 min of sampling frequency are required to measure temperature distribution. The measurement frequency of temperature distribution and required temperature measurement points have an inverse correlation.
- Thermal error estimation models were developed based on MLR. The relative displacement from the previous sample was estimated by the temperature changes

3. Thermal error analysis and modeling of CFRPMTs against spindle rotation

every 1 min. The estimated thermal errors were the integrated values of the relative displacement from the reference time after work positioning performed to the current time, which have high applicability in flexible manufacturing systems.

- The estimation models were evaluated by comparing the number of train datasets and sensor signals, against the datasets conducting from cold start and under idle reduction. By using a sufficient number of train datasets, residuals subtracted by estimation values from measurement values can be within 10 μm . The effective data acquisition for training the estimation models based on MLR is the measurements under the conditions of maximum heat generation.

4. Dynamical analysis and modeling of CFRP spindle units

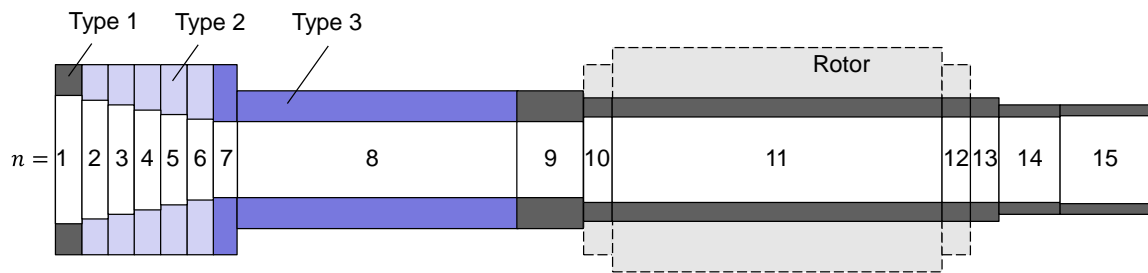
4.1. Kinematic models of substructures

For high-efficiency machining by process planning, high dynamics stiffness is required to select efficient machining conditions. This chapter proposes dynamical modeling method with lower computational costs for the development of CFRP spindle units.

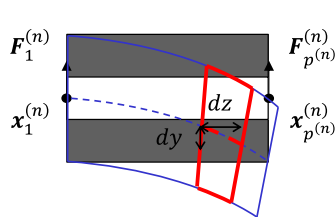
One approach to apply CFRP to spindle shafts is first choose materials, decide the target volume ratios, consider the applicable location, and fix the stacking sequences. The modeling method for CFRP spindle shaft dynamics was proposed for use in all developmental phases. A hybrid structure of CFRP and steel was employed as an example in this study; this structure was proposed by Kono et al. [11]. To develop the spindle shaft models, receptance matrices are introduced and the mechanical properties of composite spindle shafts for a TBMs are formulated.

4.1.1. One-dimensional TBM and receptance matrix

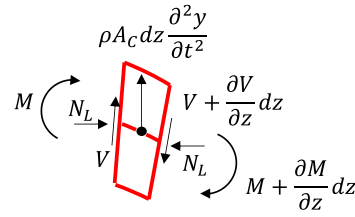
The analytical model of the CFRP spindle shaft was divided into 15 segments as shown in Fig. 4-1(a); the dimensions are summarized in Table B-1 of Appendix B. The length L_s of the segments is determined according to the difference in the stacking sequences. The rotor and sleeve of these segments from 10 to 12 are shown in Fig. 4-1(a). After calculating



(a) CFRP spindle shaft shape



(b) Structural model of the n -th segment



(c) Forces and moments on differential element

Fig. 4-1 Schematic of CFRP spindle shaft segments.

the receptance matrix of the segments, the analytical models are constructed by receptance coupling. Another advantage of low computational costs is that other models can be obtained easily by the local replacement of updated segments.

Fig. 4-1(b) and (c) show the differential element of a segment divided into a uniform cross-section. The centroidal axis of cross-section z is in the rotational axis of the shaft. Translational displacement y is defined based on the centroidal axis; bending angle θ represents the curvature of the normal line in differential elements. This diagram assumes the effects of translational and rotational inertia subjected to bending, shear, and axial loads. The translational and rotational equilibria of the motion in the differential element are given as

$$\frac{\partial V}{\partial z} = \rho A_c \frac{\partial^2 y}{\partial t^2} \quad (4-1)$$

$$\frac{\partial M}{\partial z} = V - \rho I \frac{\partial^2 \theta}{\partial t^2} + N_L \frac{\partial y}{\partial z} \quad (4-2)$$

Further, the bending moment M and shear force V are respectively defined as

$$M = -EI \frac{\partial \theta}{\partial z} \quad (4-3)$$

$$V = A_S G \gamma \quad (4-4)$$

The corresponding shear distortions γ and bending deformations θ can be represented as the infinitesimal displacement in the translational direction as

$$\frac{\partial y}{\partial z} = \gamma + \theta \quad (4-5)$$

The variables of the translational displacement and bending angle under vibration conditions are separated using the shape functions $\phi(z)$ and $\psi(z)$ as

$$y(z, t) = \phi(z) \sin(\omega t) \quad (4-6)$$

$$\theta(z, t) = \psi(z) \sin(\omega t)$$

where ω represents the angular frequency and t represents time.

For the above equations, it is known that the general solutions under the boundary conditions of free ends can be obtained as [77], [92]

4. Dynamical analysis and modeling of CFRP spindle units

$$\phi(z) = C_1 \sin\left(\frac{\alpha z}{L_s}\right) + C_2 \cos\left(\frac{\alpha z}{L_s}\right) + C_3 \sinh\left(\frac{\beta z}{L_s}\right) + C_4 \cosh\left(\frac{\beta z}{L_s}\right) \quad (4-7)$$

$$\psi(z) = \frac{1}{L_s} \left[\lambda \left[C_1 \cos\left(\frac{\alpha z}{L_s}\right) - C_2 \sin\left(\frac{\alpha z}{L_s}\right) \right] + \delta \left[C_3 \cosh\left(\frac{\beta z}{L_s}\right) + C_4 \sinh\left(\frac{\beta z}{L_s}\right) \right] \right]$$

where,

$$\lambda = \alpha - \frac{\xi^2 v^2}{\alpha}, \delta = \beta + \frac{\xi^2 v^2}{\beta} \quad (4-8)$$

$$\alpha = \sqrt{A + B}, \beta = \sqrt{-A + B}$$

$$A = \frac{(\xi^2 v^2 + \kappa^2 + \xi^2 R^2)}{2}, B = \sqrt{\frac{1}{4}(\xi^2 v^2 + \kappa^2 + \xi^2 R^2)^2 - \xi^2(\xi^2 v^2 R^2 - 1)}$$

$$\xi^2 = \frac{\rho A_C \omega^2 L_s^4}{EI}, v^2 = \frac{EI}{A_S G L_s^2}, R^2 = \frac{I}{A_C L_s^2}, \kappa^2 = \frac{N_L L_s^2}{EI}$$

$$C_2 = -\frac{D_{11}}{D_{12}} C_1$$

$$C_3 = -\frac{\lambda - \alpha}{\delta - \beta} C_1$$

$$C_4 = \frac{\lambda \alpha}{\delta \beta} C_2 = -\frac{\lambda \alpha D_{11}}{\delta \beta D_{12}} C_1$$

$$D_{11} = (\lambda - \alpha)(\cosh(\beta) - \cos(\alpha))$$

$$D_{12} = (\lambda - \alpha) \sin(\alpha) - \frac{\lambda \alpha}{\delta \beta} (\delta - \beta) \sinh(\beta)$$

$$D_{21} = -\lambda \alpha \sin(\alpha) - \frac{\lambda - \alpha}{\delta - \beta} \delta \beta \sinh(\beta)$$

$$D_{22} = \lambda \alpha (\cosh(\beta) - \cos(\alpha))$$

At this time, the characteristic equations of $\phi(z)$ obtained by eliminating some terms are expressed as

$$\begin{vmatrix} D_{11} & D_{12} \\ D_{21} & D_{22} \end{vmatrix} = 0 \quad (4-9)$$

The dynamic transverse deflection of the segment can be obtained using coefficient ratios when dimensionless frequency numbers λ_r , δ_r , α_r , and β_r are correlated with the natural frequency ω_r in the r -th natural mode, as shown in Equation (4-9). Coefficient C_1 can be obtained by the mass normalization of the eigenfunctions to convert to the mass-

normalized natural mode,

$$\int_0^{L_s} \Phi_{r_1}^T \mathbf{M} \Phi_{r_2} dz = \begin{cases} 1, & r_1 = r_2 \\ 0, & r_1 \neq r_2 \end{cases} \quad (4-10)$$

where,

$$\Phi_r(z) = \begin{Bmatrix} \phi_r(z) \\ \psi_r(z) \end{Bmatrix}, \mathbf{M} = \begin{bmatrix} \rho A_c & 0 \\ 0 & \rho I \end{bmatrix} \quad (4-11)$$

The mass-normalized eigenfunctions of the translational and rotational modes are considered to explain the two rigid body modes.

$$\phi_{DC=0}^{trans}(z) = \sqrt{\frac{1}{\rho A_c L_s}} \quad (4-12)$$

$$\phi_{DC=0}^{rot}(z) = \sqrt{\frac{12}{\rho A_c L_s^2}} \left(z - \frac{L_s}{2} \right)$$

At point z_k , the deflection represents the superimposition of all vibrations in the modal coordinates. Analytical models used in this research use the number of modal coordinates $n_m = 1000$ in the order of degrees.

$$Y(z_k) \cong \sum_{r=0}^{n_m} C_r \phi_r(z_k) \quad (4-13)$$

Each index in the equation of forced vibration substituted by the displacement vector converted by the mass-normalized natural mode is uncoupled from other mode vibrations if the harmonic vibration F_i is applied only on point z_i . Each equation correlated with the vibration modes becomes one degree of freedom based on the orthonormality by multiplying modal coordinate from the left of the equation of motion. Further, the stiffness matrix and damping matrix become the modal stiffness coefficient $-\omega_r^2$ and modal damping coefficient $j\omega_r^2\zeta$, respectively, where structural damping ζ is defined. Coefficient $C_r(z_i)$ corresponds to the modal coordinate as the component of the basis vector, which can be written as

$$C_r(z_i) = \frac{1}{(\omega_r^2 - \omega^2) + j\omega_r^2\zeta} \phi_r(z_i) F_i \quad (4-14)$$

Hence, Equation (4-13) can be rewritten as

$$Y(z_k) = \sum_{r=0}^{n_m} \frac{\phi_r(z_i) F_i}{(\omega_r^2 - \omega^2) + j\omega_r^2\zeta} \phi_r(z_k) \quad (4-15)$$

The receptance functions are denoted by the letters H , N , L , and P , which express the compliance of the linear displacement against the force, angular displacement against the force, linear displacement against the moment, and angular displacements against the moment, respectively. Therefore, the receptance functions are defined as

$$\begin{aligned} H_{ik} &= \sum_{r=0}^{n_m} \frac{\phi_r(z_i) \phi_r(z_k)}{(\omega_r^2 - \omega^2) + j\omega_r^2\zeta} \\ N_{ik} &= \sum_{r=0}^{n_m} \frac{\phi_r'(z_i) \phi_r(z_k)}{(\omega_r^2 - \omega^2) + j\omega_r^2\zeta} \\ L_{ik} &= \sum_{r=0}^{n_m} \frac{\phi_r(z_i) \phi_r'(z_k)}{(\omega_r^2 - \omega^2) + j\omega_r^2\zeta} \\ P_{ik} &= \sum_{r=0}^{n_m} \frac{\phi_r'(z_i) \phi_r'(z_k)}{(\omega_r^2 - \omega^2) + j\omega_r^2\zeta} \end{aligned} \quad (4-16)$$

Here, the indexes i and k correspond to the output and input position of the transfer functions, respectively. There representative points are selected from the positions on the centroidal axis, where $p^{(n)} = 2$ against both ends of the element is required at least. According to the above calculations, the receptance matrix of the n -th segment $\mathbf{S}^{(n)}$ can be obtained as

$$\mathbf{S}^{(n)} = \begin{bmatrix} \mathbf{S}_{11}^{(n)} & \cdots & \mathbf{S}_{1p^{(n)}}^{(n)} \\ \vdots & \ddots & \vdots \\ \mathbf{S}_{p^{(n)}1}^{(n)} & \cdots & \mathbf{S}_{p^{(n)}p^{(n)}}^{(n)} \end{bmatrix} \quad (4-17)$$

where the matrix of transfer functions is defined as

$$\mathbf{S}_{ik}^{(n)} = \begin{bmatrix} H_{ik} & L_{ik} \\ N_{ik} & P_{ik} \end{bmatrix} \quad (4-18)$$

Therefore, the receptance matrix is expressed as a square matrix of order $2p^{(n)}$.

Table 4-1 Volume ratio and mechanical properties of CFRP spindle shaft

Material	Steel	CFRP 0°	CFRP ±30°	CFRP ±45°
Density ρ [g/cm ³]	7.85	1.54	1.61	1.72
Young's modules E_{z_u} [GPa]	200	394	60.6	14.2
Shear modules	$G_{z_u x_u}$ [GPa]	76.9	3.70	3.40
	$G_{z_u y_u}$ [GPa]	76.9	3.70	75.7
Poisson's ratio	$\nu_{z_u x_u}$	0.300	0.463	0.360
	$\nu_{z_u y_u}$	0.300	0.463	0.312
Volume ratio	Target	40%	30%	0
	Type 1	100%	0	0
	Type 2	10%	45%	19%
	Type 3	40%	30%	8%

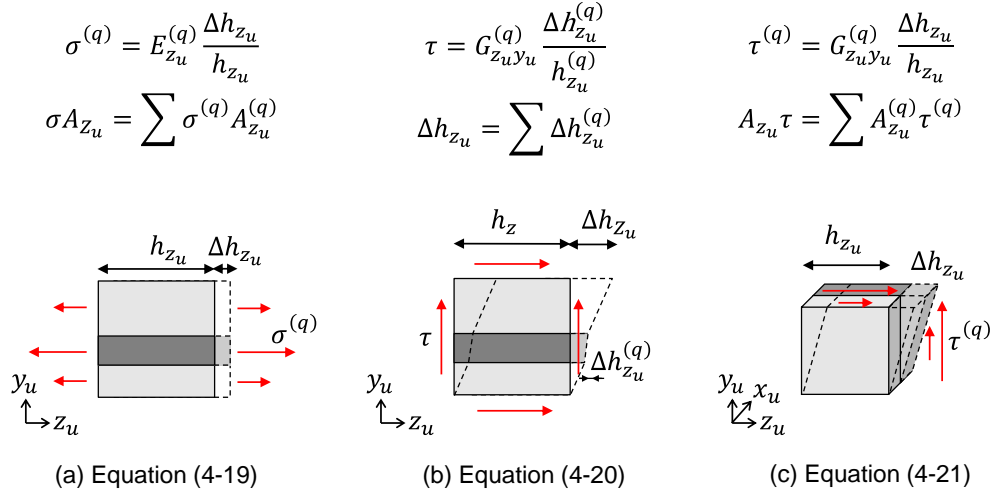


Fig. 4-2 Rule of mixture on a unit cube.

4.1.2. Mechanical property identification for CFRP spindle shafts

The mechanical properties of Young's modulus, shear modulus, and Poisson's ratio are required for the calculation of the above differential element. In product design using CFRP, an arranged fiber orientation is useful to enhance the mechanical properties in the target direction. Angle-ply laminates are combined with those having opposite phases to avoid the influence of tensile-bending coupling and bending-torsion coupling. Therefore, the volume ratio is determined based on the mechanical properties of the symmetric layers, and they are assumed to be one solid material. The design of the CFRP spindle shaft has a preference for low thermal expansion in the rotational axis direction while maintaining static stiffness. Table 4-1 summarizes the volume ratio and mechanical properties of the steel and CFRP.

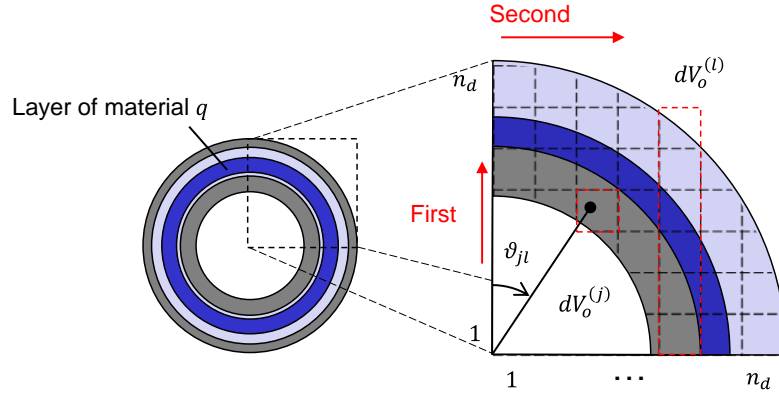


Fig. 4-3 Cross-section of composite pipes.

The Z-axis direction refers to the reference angle 0° of the fiber orientation as the z_u -axis, and the radial direction refers to the perpendicular direction as the x_u -axis on a unit cube.

These properties can be obtained based on rule of mixture for the composites; Figure 4-2 shows the derivation [44]. The equivalent mechanical properties have the following relation by using the volume ratio $V_o^{(q)}$ corresponding to the cross-sectional area $A_{z_u}^{(q)}$ of i -th matrix or fiber:

$$E_{z_u} = \sum_{q=1}^{n_q} V_o^{(q)} E_{z_u}^{(q)} \quad (4-19)$$

$$\frac{1}{G_{z_u y_u}} = \sum_{q=1}^{n_q} \frac{V_o^{(q)}}{G_{z_u y_u}^{(q)}} \quad (4-20)$$

$$G_{z_u y_u} = \sum_{q=1}^{n_q} V_o^{(q)} G_{z_u y_u}^{(q)} \quad (4-21)$$

Further, these equations hold for several materials. The number i is correlated to the stacking composite layers when a uniform distribution of fiber is assumed in each layer. Equations (4-20) and (4-21) describe the equivalent shear modules of the composites located along the longitudinal direction and parallel to the load direction, respectively. Rule of mixture is the same as that of FEA if the composite layers have parallel boundaries in one direction. Further, the integral approach is effective when boundaries have a geometric shape such as an arch. The performance is less deteriorated if the boundaries have long inclusion lengths against the load direction because the influence near the boundaries is dispersed in the surrounding matrix. Rule of mixture is adopted in the cross-section of the CFRP shaft to obtain the mechanical properties considering the layout, as shown in Fig. 4-

3.

$$E = \sum_{q=1}^{n_q} \frac{E_{z_u}^{(q)} I^{(q)}}{I} \quad (4-22)$$

$$G = \sum_{l=1}^{n_d} dV_o^{(l)} \left(\sum_{j=1}^{n_d} \frac{dV_o^{(j)}}{dG_z^{(j)}} \right)^{-1} \quad (4-23)$$

when assuming a uniform distribution

$$dG_z^{(j)} = \left[\sum_{q=1}^{n_q} V_o^{(q)} \left(G_{z_u x_u}^{(q)} \cos^2 \vartheta_{jl} + G_{z_u y_u}^{(q)} \sin^2 \vartheta_{jl} \right)^{-1} \right]^{-1} \quad (4-24)$$

when defining the dimensions

$$dG_z^{(j)} = G_{z_u x_u}^{(q)} \cos^2 \vartheta_{jl} + G_{z_u y_u}^{(q)} \sin^2 \vartheta_{jl} \quad (4-25)$$

Here, ϑ represents the angle of the divided area in polar coordinates and n_d is divided into 120 unit cells in each direction. First, the local parameters in the thin rectangular elements are calculated by integrating the unit cells in the parallel direction against the external force; the coordinate transformation of rotation is applied to the components of the unit cells. Second, shear stiffness is obtained by integrating thin rectangular elements in the vertical direction. dV_o is the area ratio of the unit cells or thin rectangular elements against the integrated area. On the boundary of the layers, the parameters of a single material with the highest volume of the two are used in Equation (4-25).

Like the shear modules, Poisson's ratio is calculated to define the effective shear area. The shear coefficient for a beam with a hollow circular cross-section is employed [77], [92].

$$A_s = \frac{6(1+\nu) \left(1 + \frac{d_{in}^2}{d_{out}^2} \right)^2}{(7+6\nu) \left(1 + \frac{d_{in}^2}{d_{out}^2} \right)^2 + (20+12\nu) \frac{d_{in}^2}{d_{out}^2}} A_c \quad (4-26)$$

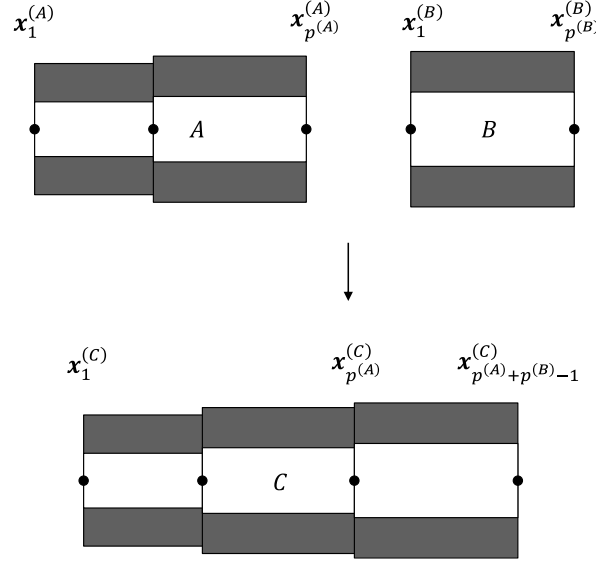


Fig. 4-4 Schematic of multi-point receptance coupling with rigid joints.

4.2. Multipoint receptance coupling for spindle unit dynamics

The dynamical models of spindle shafts and spindle units are constructed based on receptance coupling. In this section, receptance coupling is redefined to remain the information of dynamics at multiple points. Hence, both FRF and mode shape can be observed at low computational costs. Moreover, kinematic can be used to identify the bearing properties from measurement results.

4.2.1. Multipoint receptance coupling for individual components in axial direction

Figure 4-4 shows two segments of the CFRP spindle under free-end conditions. The equations of receptance matrices of A and B , respectively, with $p^{(A)}$ and $p^{(B)}$ of representative points, can be written as

$$\begin{cases} \mathbf{x}_1^{(A)} \\ \vdots \\ \mathbf{x}_{p^{(A)}}^{(A)} \end{cases} = \begin{bmatrix} \mathbf{S}_{11}^{(A)} & \cdots & \mathbf{S}_{1p^{(A)}}^{(A)} \\ \vdots & \ddots & \vdots \\ \mathbf{S}_{p^{(A)}1}^{(A)} & \cdots & \mathbf{S}_{p^{(A)}p^{(A)}}^{(A)} \end{bmatrix} \begin{cases} \mathbf{F}_1^{(A)} \\ \vdots \\ \mathbf{F}_{p^{(A)}}^{(A)} \end{cases} \quad (4-27)$$

$$\begin{cases} \mathbf{x}_1^{(B)} \\ \vdots \\ \mathbf{x}_{p^{(B)}}^{(B)} \end{cases} = \begin{bmatrix} \mathbf{S}_{11}^{(B)} & \cdots & \mathbf{S}_{1p^{(B)}}^{(B)} \\ \vdots & \ddots & \vdots \\ \mathbf{S}_{p^{(B)}1}^{(B)} & \cdots & \mathbf{S}_{p^{(B)}p^{(B)}}^{(B)} \end{bmatrix} \begin{cases} \mathbf{F}_1^{(B)} \\ \vdots \\ \mathbf{F}_{p^{(B)}}^{(B)} \end{cases}$$

After coupling the two segments, the displacement and force vectors can be written as

$$\mathbf{x}_i^{(C)} = \begin{cases} \mathbf{x}_j^{(A)} (i \leq p^{(A)}) \\ \mathbf{x}_{i-p^{(A)+1}^{(B)}} (i \geq p^{(A)}) \end{cases} \quad (4-28)$$

$$\mathbf{F}_i^{(C)} = \begin{cases} \mathbf{F}_i^{(A)} (i < p^{(A)}) \\ \mathbf{F}_{p^A}^{(A)} + \mathbf{F}_1^{(B)} (i = p^{(A)}) \\ \mathbf{F}_{i-p^{(A)+1}^{(B)}}^{(B)} (i > p^{(A)}) \end{cases}$$

$$p^{(C)} = p^{(A)} + p^{(B)} - 1$$

Here, $p^{(C)}$ denotes the number of representative coordinates after the coupling. From the row of a coupled point, the component force vectors can be written as

$$\mathbf{F}_{p^{(A)}}^{(A)} = \left(\mathbf{S}_{p^{(A)}p^{(A)}}^{(A)} + \mathbf{S}_{11}^{(B)} \right)^{-1} \left(-\mathbf{S}_{p^{(A)}1}^{(B)} \mathbf{F}_1^{(C)} \cdots -\mathbf{S}_{p^{(A)}p^{(A)}-1}^{(A)} \mathbf{F}_{p^{(A)}-1}^{(C)} + \mathbf{S}_{11}^{(B)} \mathbf{F}_{p^{(A)}}^{(C)} \right. \\ \left. + \mathbf{S}_{12}^{(B)} \mathbf{F}_{p^{(A)+1}^{(C)}} \cdots + \mathbf{S}_{1p^{(B)}}^{(B)} \mathbf{F}_{p^{(A)+p^{(B)}-1}^{(C)} \right) \quad (4-29)$$

$$\mathbf{F}_1^{(B)} = \left(\mathbf{S}_{p^{(A)}p^{(A)}}^{(A)} + \mathbf{S}_{11}^{(B)} \right)^{-1} \left(\mathbf{S}_{p^{(A)}1}^{(A)} \mathbf{F}_1^{(C)} \cdots + \mathbf{S}_{p^{(A)}p^{(A)}-1}^{(A)} \mathbf{F}_{p^{(A)}-1}^{(C)} + \mathbf{S}_{p^{(A)}p^{(A)}}^{(A)} \mathbf{F}_{p^{(A)}}^{(C)} \right. \\ \left. - \mathbf{S}_{12}^{(B)} \mathbf{F}_{p^{(A)+1}^{(C)}} \cdots - \mathbf{S}_{1p^{(B)}}^{(B)} \mathbf{F}_{p^{(A)+p^{(B)}-1}^{(C)} \right)$$

Therefore, the receptance matrix after coupling two segments can be expressed as

$$\begin{Bmatrix} \mathbf{x}_1^{(C)} \\ \vdots \\ \mathbf{x}_{p^{(C)}}^{(C)} \end{Bmatrix} = \begin{bmatrix} \mathbf{S}_{11}^{(C)} & \cdots & \mathbf{S}_{1,p^{(C)}}^{(C)} \\ \vdots & \ddots & \vdots \\ \mathbf{S}_{p^{(C)},1}^{(C)} & \cdots & \mathbf{S}_{p^{(C)},p^{(C)}}^{(C)} \end{bmatrix} \begin{Bmatrix} \mathbf{F}_1^{(C)} \\ \vdots \\ \mathbf{F}_{p^{(C)}}^{(C)} \end{Bmatrix} \quad (4-30)$$

where

$$\mathbf{S}_{ik}^{(C)} = \begin{cases} \mathbf{S}_{ik}^{(A)} - \mathbf{S}_{ip^{(A)}}^{(A)} \left(\mathbf{S}_{p^{(A)}p^{(A)}}^{(A)} + \mathbf{S}_{11}^{(B)} \right)^{-1} \mathbf{S}_{p^{(A)}k}^{(A)} & (i \leq p^{(A)}, k < p^{(A)}) \\ \mathbf{S}_{ip^{(A)}}^{(A)} \left(\mathbf{S}_{p^{(A)}p^{(A)}}^{(A)} + \mathbf{S}_{11}^{(B)} \right)^{-1} \mathbf{S}_{1,k-p^{(A)+1}}^{(B)} & (i \leq p^{(A)}, k \geq p^{(A)}) \\ \mathbf{S}_{i-p^{(A)+1,1}}^{(B)} \left(\mathbf{S}_{p^{(A)}p^{(A)}}^{(A)} + \mathbf{S}_{11}^{(B)} \right)^{-1} \mathbf{S}_{p^{(A)}k}^{(A)} & (i \geq p^{(A)}, k \leq p^{(A)}) \\ \mathbf{S}_{i-p^{(A)+1,k-p^{(A)+1}}^{(B)} - \mathbf{S}_{i-p^{(A)+1,1}}^{(B)} \left(\mathbf{S}_{p^{(A)}p^{(A)}}^{(A)} + \mathbf{S}_{11}^{(B)} \right)^{-1} \mathbf{S}_{1,k-p^{(A)+1}}^{(B)} & (i \geq p^{(A)}, k > p^{(A)}) \end{cases} \quad (4-31)$$

4. Dynamical analysis and modeling of CFRP spindle units

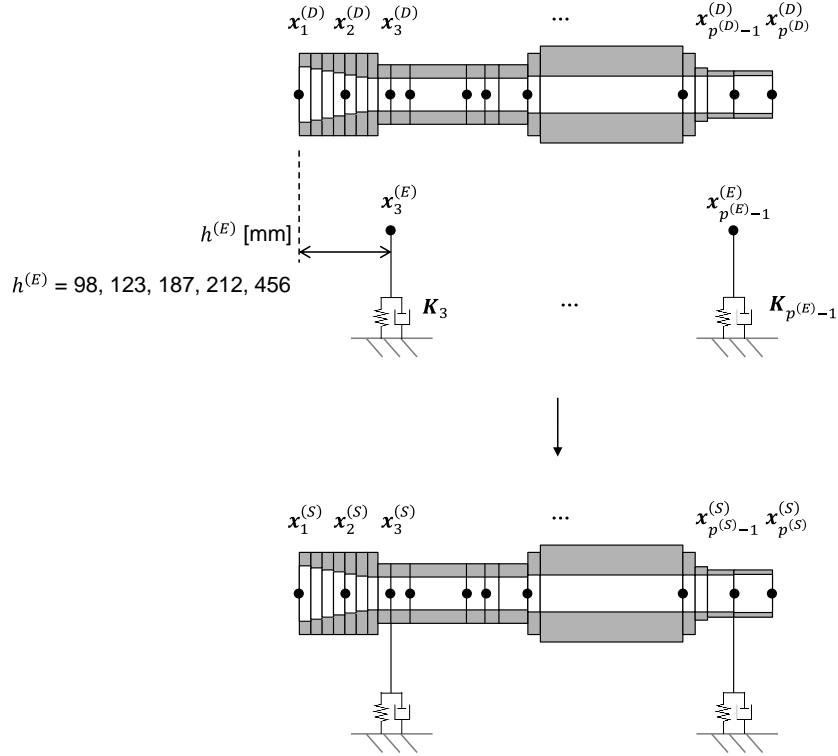


Fig. 4-5 Kinematic model of a spindle shaft grounded by springs and dampers; the distance from the spindle nose to the contact points of bearings on the CFRPMT is mentioned as $h^{(E)}$.

4.2.2. Bearing property identification from frequency response functions (FRFs)

Figure 4-5 illustrates the coupling of a spindle shaft model and bearing properties as a spring-damper system. The receptance matrix of spindle shaft $\mathbf{S}^{(D)}$ is developed under free-end conditions. The receptance matrix of bearings is defined as follows:

$$\mathbf{S}^{(E)} = \begin{bmatrix} \mathbf{K}_1 & & \mathbf{0} \\ & \ddots & \\ \mathbf{0} & & \mathbf{K}_{p^{(E)}} \end{bmatrix}^{-1} \quad (4-32)$$

where the properties are defined as:

$$\mathbf{K}_i = \begin{bmatrix} kt_i + j\omega ct_i & 0 \\ 0 & kr_i + j\omega cr_i \end{bmatrix} \text{ or } \mathbf{0} \quad (4-33)$$

Here, the parameters kt_i , kr_i , ct_i and cr_i represent the translational and rotational stiffnesses as the bearing dynamics expressed in complex numbers. In this study, DTBT

angular contact ball bearings and cylindrical roller bearings were used. The preload $N_L = 215$ was applied between the front bearings. The dimension of the diagonal matrix is the same as that of the receptance matrix of the spindle shaft. The element number i represents the representative points of the bearing location, and the other submatrices are zero.

After coupling with the bearings and shaft, the representative coordinates were found to be consistent. Inverse matrices can now be easily obtained using software. From the equation of motion, the component force vectors can be written as

$$\mathbf{F}^{(S)} = \mathbf{F}^{(D)} + \mathbf{F}^{(E)} = (\mathbf{S}^{(D)})^{-1} \mathbf{x}^{(D)} + (\mathbf{S}^{(E)})^{-1} \mathbf{x}^{(E)} \quad (4-34)$$

Therefore, the receptance matrix of the spindle-bearing system S comprises the receptance matrices of shafts and bearings as

$$(\mathbf{S}^{(S)})^{-1} = (\mathbf{S}^{(D)})^{-1} + (\mathbf{S}^{(E)})^{-1} \quad (4-35)$$

The compliance $H_{11}^{(S)}$ of analytical models corresponds to the FRFs at the spindle nose in the transverse direction. The receptance matrix of shafts can be calculated from the material properties and dimensions. If the FRF H_{meas} at the spindle nose are measured, the bearing properties of the receptance matrix of bearings can be identified by solving the minimization problem. The cost function of the least-squares method is defined in Equation (4-36). Compared to previous research [77], the approximation of the dynamic system and the number of calculations for combining the bearings is avoided. However, the quality of the inverse matrix calculation must be considered.

$$S_{cf} = \sum \sqrt{\left[\text{Re}(H_{meas}(\omega)) - \text{Re}(H_{11}^{(S)}(\omega)) \right]^2 + \left[\text{Im}(H_{meas}(\omega)) - \text{Im}(H_{11}^{(S)}(\omega)) \right]^2} \quad (4-36)$$

4.2.3. Multipoint receptance coupling considering contact characteristics

Generally, the dynamics of the whole spindle unit is represented by coupling analytical and measured receptance at both end points of individual components, such as the spindle, holder, and tool. The method of elastic coupling for the receptance matrix [68], [69], [71], [77] was employed. The contact characteristics at the holder-tool and spindle-holder interfaces must also be considered for receptance coupling.

4. Dynamical analysis and modeling of CFRP spindle units

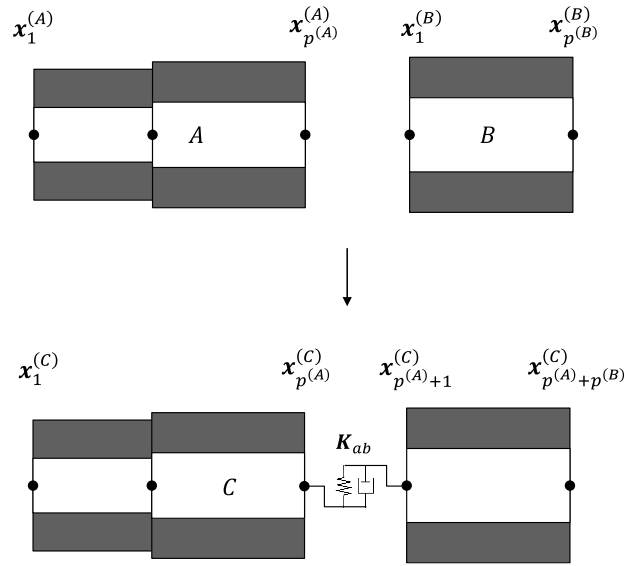


Fig. 4-6 Schematics of multipoint receptance coupling with spring–damper joints.

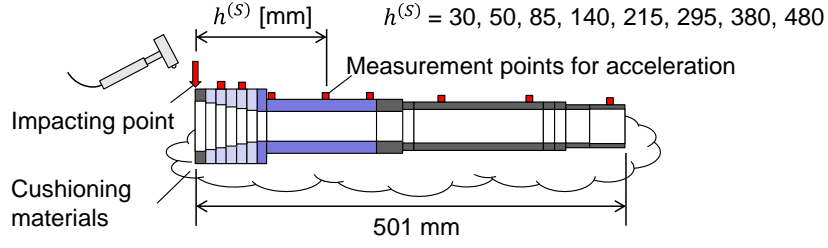
Figure 4-6 displays two segments with receptance matrices $\mathbf{S}^{(A)}$ and $\mathbf{S}^{(B)}$, following Equation (4-17). The segments were coupled by considering the contact parameters as constituting a spring–damper system. The receptance matrix of the interface is written as:

$$\mathbf{K}_{ab} = \begin{bmatrix} kt_{ab} + j\omega ct_{ab} & 0 \\ 0 & kr_{ab} + j\omega cr_{ab} \end{bmatrix} \quad (4-37)$$

Here, the parameters kt_{ab} , kr_{ab} , ct_{ab} , and cr_{ab} represent the translational and rotational stiffnesses as the contact characteristics expressed in complex numbers. General receptance coupling retaining both end matrices is in the case of $i, k = 1, p^{(A)} + p^{(B)}$, in the rows and columns.

Then, the receptance matrix of the bearing–spindle–holder system SH is calculated by coupling of $\mathbf{S}^{(S)}$ and $\mathbf{S}^{(H)}$ with the interface \mathbf{K}_{sh} in Equation (4-38). This equation, under the assumed contact parameters, is also used for the holder–tool interaction to obtain the receptance matrix of the entire spindle unit system, SHT . The receptance matrix of the interface is defined as \mathbf{K}_{ht} , similar to the interface in Equation (4-37). After the receptance matrix $\mathbf{S}^{(SHT)}$ is calculated by coupling the receptance matrix $\mathbf{S}^{(SH)}$ with the tool dynamics $\mathbf{S}^{(T)}$ from Equation (4-38), compliance $H_{11}^{(SHT)}$ as the FRF at the tool tip can be obtained.

4. Dynamical analysis and modeling of CFRP spindle units



(a) Schematic diagram of the measurement



(b) Appearance

Fig. 4-7 Experimental setup of impacting the CFRP spindle shaft.

$$\mathbf{s}_{ik}^{(C)} = \begin{cases} \mathbf{s}_{ik}^{(A)} - \mathbf{s}_{ip^{(A)}}^{(A)} \left(\mathbf{s}_{p^{(A)}p^{(A)}}^{(A)} + \mathbf{K}_{sh}^{-1} + \mathbf{s}_{11}^{(B)} \right)^{-1} \mathbf{s}_{p^{(A)}k}^{(A)} & (i \leq p^{(A)}, k < p^{(A)}) \\ \mathbf{s}_{ip^{(A)}}^{(A)} \left(\mathbf{s}_{p^{(A)}p^{(A)}}^{(A)} + \mathbf{K}_{sh}^{-1} + \mathbf{s}_{11}^{(B)} \right)^{-1} \left(\mathbf{K}_{sh}^{-1} + \mathbf{s}_{11}^{(B)} \right) & (i \leq p^{(A)}, k = p^{(A)}) \\ \mathbf{s}_{ip^{(A)}}^{(A)} \left(\mathbf{s}_{p^{(A)}p^{(A)}}^{(A)} + \mathbf{K}_{sh}^{-1} + \mathbf{s}_{11}^{(B)} \right)^{-1} \mathbf{s}_{1,k-p^{(A)}}^{(B)} & (i \leq p^{(A)}, k > p^{(A)}) \\ \mathbf{s}_{i-p^{(A)},1}^{(B)} \left(\mathbf{s}_{p^{(A)}p^{(A)}}^{(A)} + \mathbf{K}_{sh}^{-1} + \mathbf{s}_{11}^{(B)} \right)^{-1} \mathbf{s}_{p^{(A)}k}^{(A)} & (i > p^{(A)}, k < p^{(A)} + 1) \\ \mathbf{s}_{i-p^{(A)},1}^{(B)} \left(\mathbf{s}_{p^{(A)}p^{(A)}}^{(A)} + \mathbf{K}_{sh}^{-1} + \mathbf{s}_{11}^{(B)} \right)^{-1} \left(\mathbf{s}_{p^{(A)}p^{(A)}}^{(A)} + \mathbf{K}_{sh}^{-1} \right) & (i > p^{(A)}, k = p^{(A)} + 1) \\ \mathbf{s}_{i-p^{(A)},k-p^{(A)}}^{(B)} - \mathbf{s}_{i-p^{(A)},1}^{(B)} \left(\mathbf{s}_{p^{(A)}p^{(A)}}^{(A)} + \mathbf{K}_{sh}^{-1} + \mathbf{s}_{11}^{(B)} \right)^{-1} \mathbf{s}_{1,k-p^{(A)}}^{(B)} & (i > p^{(A)}, k > p^{(A)} + 1) \end{cases} \quad (4-38)$$

4.3. Validation of CFRP spindle shaft dynamics

Mechanical property identification on composite materials and multipoint receptance coupling are proposed in Section 4.1 and 4.2, respectively. All proposed models were developed using a commercial programming language, MATLAB R2021b (MathWorks). Analytical models following all developmental phases of the CFRP spindle shaft are developed and compared to measurement results and a model developed by FEA.

4.3.1. Impact tests of CFRP spindle shaft and analysis conditions

The impact test of the CFRP spindle shaft was conducted on cushioning materials under free-end conditions. Figure 4-7 shows the experimental setup for the impact test. The front end of the shaft was excited using an impulse hammer (086C03, PCB Piezotronics). The

4. Dynamical analysis and modeling of CFRP spindle units

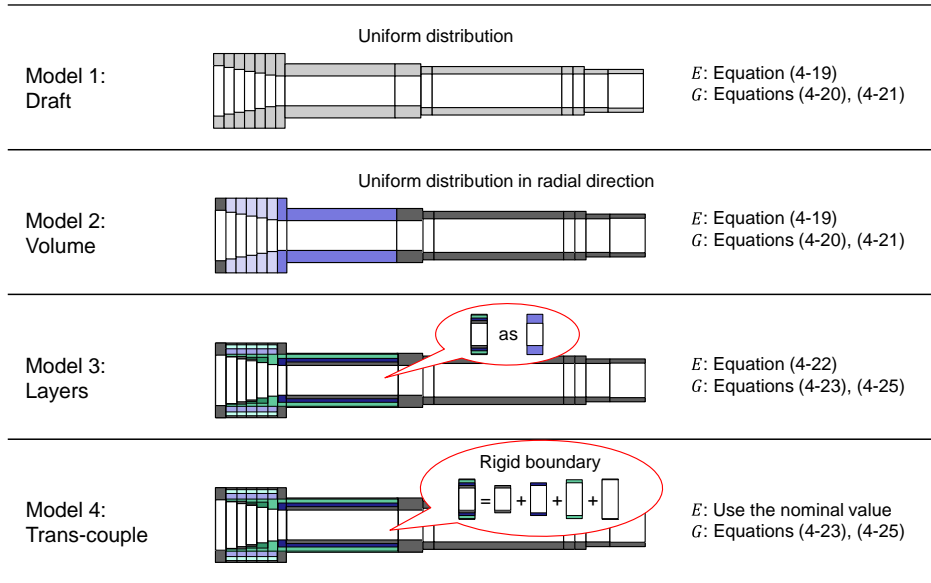


Fig. 4-8 Analytical models of CFRP spindle shaft according to the development phase.

Table 4-2 Calculated physical properties of divided segments on the analytical models

Param	Model 1	Model 2		Model 3						
n	1–15	2–6	7, 8	2	3	4	5	6	7	8
E [GPa]	202–203	214	206	216	216	216	216	216	201	204
G [GPa]	10.0–10.1	7.20–7.21	10.0–10.1	24.7	24.5	23.9	23.9	24.4	51.7	34.1
ν	0.0809–0.0810	0.119–0.120	0.101–0.102	0.0689	0.0699	0.0692	0.0670	0.0697	0.227	0.168

acceleration of the shaft was measured at eight measurement points using piezoelectric accelerometers (356A16, PCB Piezotronics). The FRFs from the excitation force to the shaft displacement were obtained via double integration. The sampling frequency and number of sample points were set to 12.8 kHz and 8192, respectively. The FRFs from the five measurements were averaged by an FFT analyzer (DS-3000, ONO SOKKI).

Four types of analytical models were compared as shown in Fig. 4-8; the conditions for the comparison are listed in Table 4-2. The equivalent coefficients of the draft model were determined using the initial target volume, as summarized in Table 4-1. The draft model assumes a uniform distribution of the materials in the spindle shaft. Further, the volume model is determined using the actual volume ratio of each segment, whose parameters are obtained by Equations (4-19), (4-23), and (4-24). The volume model assumes a uniform distribution in the radial direction. The layers model used in Equations (4-22), (4-23), and (4-25) considers the dimensions of the layers. For a holder–tool or shaft–holder assembly, Schmitz et al. proposed a combination method for receptance matrices of the inner and outer pipes in the transverse direction [68]. Model 4 using transverse coupling described in

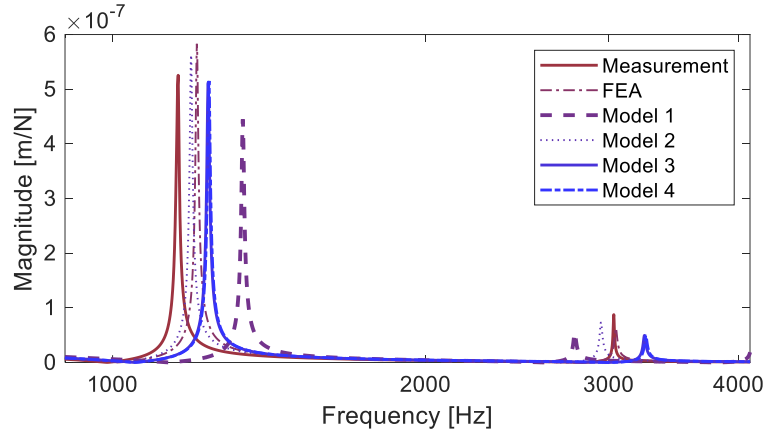


Fig. 4-9 FRFs located at a distance of 30 mm from the impact point on the CFRP spindle shaft.

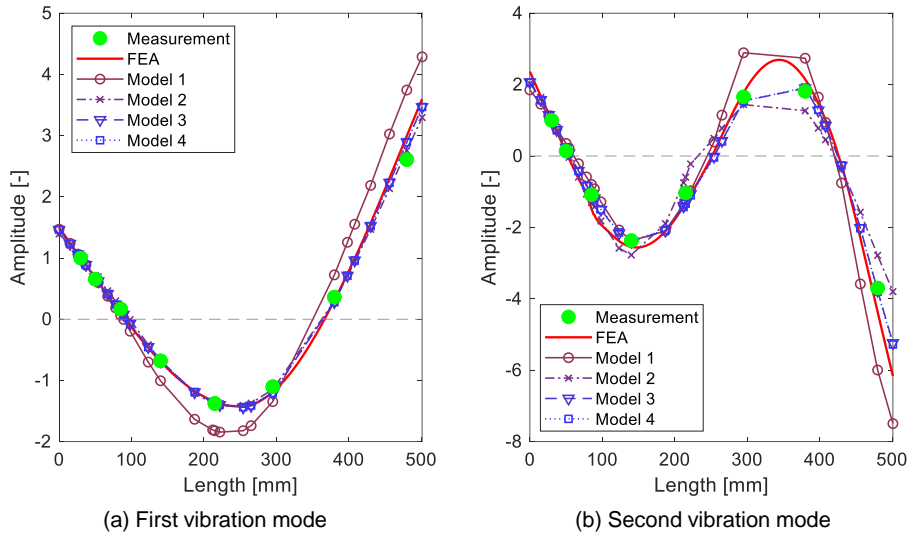


Fig. 4-10 Mode shapes in natural frequencies.

Appendix C corresponds to this method. Receptance matrices are obtained by calculating each layer using Equations (4-23) and (4-25), and they are combined with all layers in each segment. For mass normalization, a function object of numerical integration (@integral) was used. In the calculations of combining the receptance matrices and combining the bearing matrices, a function object of inverse matrices (@inv) was used.

The modal analysis of the shaft for the free-free boundary condition was conducted using the FEA to verify the proposed models. A commercial FEA package, ANSYS Workbench 17.2, was used for the analysis. A 3D model of the shaft was developed using CAD. The CFRP stacked with a consistent stacking sequence was modeled as a solid orthotropic material, and these solid components were assembled by bonding without considering the adhesive layers. The material properties of the CFRP, listed in Table 4-1, were used in the simulation. In the above analysis, structural damping $\zeta = 2.9 \times 10^{-3}$ was defined based on the

Table 4-3 Natural frequencies and MAC on the CFRP spindle shaft

Models	First mode			Second mode		
	Freq. [Hz]	Diff. [%]	S_{MAC}	Freq. [Hz]	Diff. [%]	S_{MAC}
Measurements	1156	-	-	3031	-	-
FEA	1203	4.1	0.9947	3044	0.4	0.9959
Model 1	1334	15.4	0.9851	2782	-8.2	0.9562
Model 2	1190	2.9	0.9988	2948	-2.7	0.9541
Model 3	1236	6.9	0.9970	3246	7.1	0.9967
Model 4	1238	7.1	0.9969	3256	7.4	0.9961

measurement results.

4.3.2. Comparison and discussion of analytical models

Figure 4-9(a) shows the FRFs at a distance of 30 mm from the front end of the CFRP spindle shaft. Table 4-3 summarizes the natural frequencies in the estimated first and second vibration modes. Model 1 shows large errors of natural frequencies. Model 2 shows lower errors of 1.2% than that of the FEA in the first vibration mode. The high accuracy of the TBM is an advantage because the first vibration mode oscillates the entire structure. The natural frequency in the first vibration mode can be estimated by the definition of the site applying the CFRP. Models 3 and 4 are similar estimations due to the same assumptions of the equivalent coefficients. The large differences in the parameters between models 2 and 3 are the equivalent shear stiffness as presented in Table 4-2. Model 2 uses lower shear stiffness which is consistent with the measured results. Moreover, the proposed modeling method helps estimate the dynamics of the CFRP spindle shafts using the parameters of its dimension and the volume ratio with lower computational costs than FEA.

Meanwhile, we focus on the mode shape, which indicates the time variation of a specific vibration pattern. Figure 4-10 shows the mode shapes in the natural frequencies of each model, which were obtained from $H_{i1}^{(D)}(\omega_r)$; the reference value of the phase was the impact point and the magnitudes were divided by the value at a distance of 30 mm from the front end. Modal assurance criterion (MAC) is a popular statistical indicator for the quantitative comparison of modal vectors [93] and is given as

$$S_{MAC} = \frac{|\sum H_{i1}(\omega_r)H_{meas,i}(\omega_{meas,r})|^2}{(\sum H_{i1}(\omega_r)^2)(\sum H_{meas,i}(\omega_{meas,r})^2)} \quad (4-39)$$

Table 4-4 Sensitivity analysis of natural frequencies and MAC of the spindle shaft models with a parameterization error of $\pm 5\%$

Variation of E_{z_u} , G_{z_u}	First mode				Second mode				
	Freq. [Hz]	Var. [Hz]	S_{MAC}	Var.	Freq. [Hz]	Var. [Hz]	S_{MAC}	Var.	
Model 1:	+5%	1357	23	0.9850	-0.0001	2837	55	0.9563	0.0001
	-5%	1310	-24	0.9850	-0.0001	2724	-58	0.9561	-0.0001
Model 2:	+5%	1197	7	0.9986	-0.0002	2984	36	0.9607	0.0066
	-5%	1182	-8	0.9991	0.0003	2911	-37	0.9464	-0.0077
Model 3:	+5%	1241	5	0.9967	-0.0003	3266	20	0.9959	-0.0008
	-5%	1230	-6	0.9972	0.0002	3224	-22	0.9974	0.0007
Model 4:	+5%	1243	5	0.9966	-0.0003	3275	19	0.9952	-0.0009
	-5%	1233	-5	0.9972	0.0003	3237	-19	0.9968	0.0007

Here, ω_r and $\omega_{meas,r}$ represent the natural frequencies. $H_{meas,i}$ denotes the measured FRFs, where i represents the number of coordinates at the measurement points of eight. The results of the MAC in each model against the measurement are summarized in Table 4-3.

In the first vibration mode, MAC of model 2 is 0.9988, and the estimation is the most accurate. Models 3 and 4 show more accurate mode shapes than the others in the second vibration mode. The same tendency is observed in both models, the natural frequencies of which were higher than the measured ones around 7%. The model value of the mass integrated all segments corresponds reasonably well with the measurement of the spindle shaft. Thus, one of the causes for this result is the influence of the screw joint with the adhesive, mass of the accelerometers and cushioning materials. The analytical models and FEA ignore the contact characteristics on the 9-th segment. Model 3 was recalculated in the case of the elastic coupling in Equation (4-38) employed between the 9th and 10th segments. The values of the translational and rotational stiffness obtained by curve fitting of in the similar manner to Equation (4-36) were 6.13×10^8 N/m and 3.07×10^6 Nm/rad. The interface dynamics expressed the shift of natural frequency with improving MAC values. The estimated natural frequencies and MAC of the trans-couple model are slightly worse than those of the layers model because modeling errors are accumulated by calculating each layer despite the higher computational costs.

The difficulty in the accurate parameterization of laminated CFRP layers sometimes induces modeling errors. The Young's modulus and shear modulus of the CFRP in Table 4-1 were changed by $\pm 5\%$ and the analytical models recalculated to evaluate the sensitivity of the models against the variation of mechanical properties. Table 4-4 lists the natural

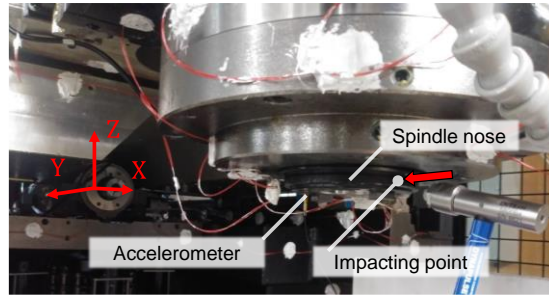


Fig. 4-11 Experimental setup of the impact tests in the Y-axis direction on the spindle unit.

frequencies and MAC of the spindle shaft models with a parameterization error of $\pm 5\%$. The values are summarized as the variation of the models using the initial parameters. The layers model and trans-couple model were robust against parameterization errors because the consideration of stacking sequences limits the influence. Further, the discretization of the dimensions in the Z-axis direction should be considered in addition to the deterioration of the analytical models. The division into the segments is discussed in Fig. B-1 of Appendix B.

The above results indicate that the first vibration mode can be estimated using equivalent coefficients assuming a uniform distribution in the rotational direction without using CAD models. Further, the information of stacking sequences is required to estimate dependable dynamic characteristics. Compared to the measurements, the analytical models and FEA show higher natural frequencies owing to the round of contact rigidity and mass.

4.4. Validation of motorized CFRP spindle unit dynamics

The spindle unit dynamics is developed by using the spindle shaft model developed in Section 4.3, and the bearing properties are identified from the measurement results. Further, the effect of CFRP application on the dynamic stiffness of machine tool spindle units are discussed by comparing the analytical models.

4.4.1. Impact tests at the spindle nose and bearing property identification

The impact of thermal expansion of bearings is herein discussed as a case study of the changes in dynamic properties. The main spindle was rotated at 9000 min^{-1} for 2 h to warm-up the spindle unit. After 10 min from stopping the spindle rotation, impact tests were conducted at the spindle nose in X- and Y-axis directions. Figure 4-11 shows the experimental setup. The front end of the mounted shaft was excited using an impulse hammer (5850B4, Dytran Instruments), and the acceleration of the spindle nose in the Y-

Table 4-5 Identified bearing properties

Bearings		Translational	Translational	Rotational	Rotational
		stiffness	damping	stiffness	damping
		kt [N/m]	ct [Ns/m]	kr [Nm/rad]	cr [Nms/rad]
Initial conditions	K_{1-4}	100×10^6	1000	5.00×10^5	10
	K_5	100×10^6	100	5.00×10^5	10
Identification in X-axis	$K_{1,2}$	5.38×10^7	3.43×10^2	2.97×10^6	5.03×10
	$K_{3,4}$	1.86×10^8	1.29×10^{-10}	1.01×10^4	4.17×10^{-13}
	K_5	2.98×10^8	2.75×10^3	3.04×10^4	1.83×10^{-6}
Identification in Y-axis	$K_{1,2}$	5.11×10^7	1.98×10^2	2.96×10^5	3.38×10^2
	$K_{3,4}$	2.68×10^8	9.15×10^4	3.66×10^5	1.98×10^{-6}
	K_5	1.50×10^8	2.61×10^{-5}	6.56×10^5	1.83×10^{-6}

axis was measured using a piezoelectric accelerometer (NP-3412, ONO SOKKI). The FRFs from the ten measurements were averaged by a FFT analyzer (DS-3000, ONO SOKKI) and the phase was inverted after the measurements.

A layers model was used for the motorized CFRP spindle unit and referred to as model 5. The estimation accuracy of the mode shapes was significant because the spindle shafts were supported at several intermediate points. The parts of the rotor and sleeve were connected by a shrink fit; the models used the same mechanical properties as those of steel listed in Table 4-1 and were coupled by means of a rigid joint. For the combination of bearing properties, a function object optimized by the simplex method (@fminsearch) was used to identify the bearing properties by the cost function of the least-squares method in Equation (4-36). The frequency bandwidth for the identification ranged from 300–2500 Hz at 2817 points. The optimization problem was solved twice to avoid falling into a local solution. First, the models of the front bearing properties are defined in the same variables $K_1 = K_2 = K_3 = K_4$. Next, the obtained solution was used as the initial condition for the identification of the assumed bearing properties $K_1 = K_2 \neq K_3 = K_4$.

4.4.2. Results of bearing property identification and discussion of effectivity of CFRP application

Figure 4-12 shows the FRFs of measurements and spindle unit models in the X- and Y-axes. Table 4-5 summarizes the identified bearing properties, where the initial conditions are set for the identification. The resonant frequencies are different in each direction; however, two similar peaks are found: the highest peak around 1000 Hz and the second highest peak around 1200 Hz. Figure 4-13 shows the mode shapes on resonant frequencies

4. Dynamical analysis and modeling of CFRP spindle units

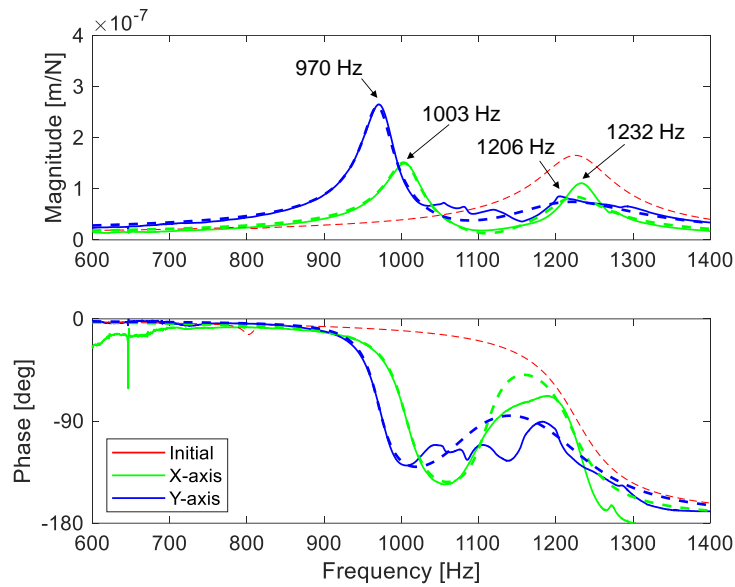


Fig. 4-12 FRFs at the spindle nose on the CFRP machine tool.

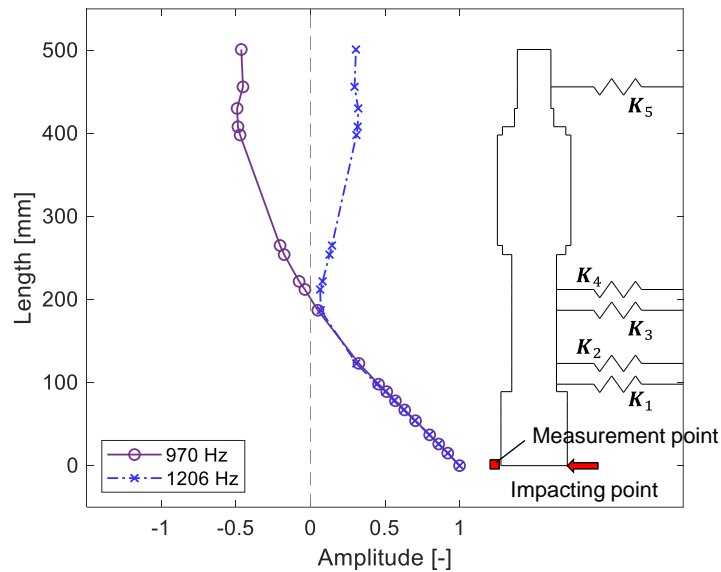


Fig. 4-13 Mode shapes of the mounted CFRP spindle shaft in the Y-axis direction.

in the Y-axis direction. On the highest peak, the spindle shaft oscillated as rolling or pitching motion around the bottom of the sleeve. Therefore, compliance in the X-axis is lower than that in the Y-axis because the identified equivalent stiffness of the top and bottom bearings in the X-axis becomes larger than that in the Y-axis. The equivalent stiffness includes not only the modeling errors of the shaft and the bearings but also the influence of other supporting structural dynamics. The CFRP spindle unit is supported by the ram of the Z-axis, the slider of the X-axis, and the saddle of the Y-axis, in that order. Further, the differences are attributed to machine configurations and not to the mechanical

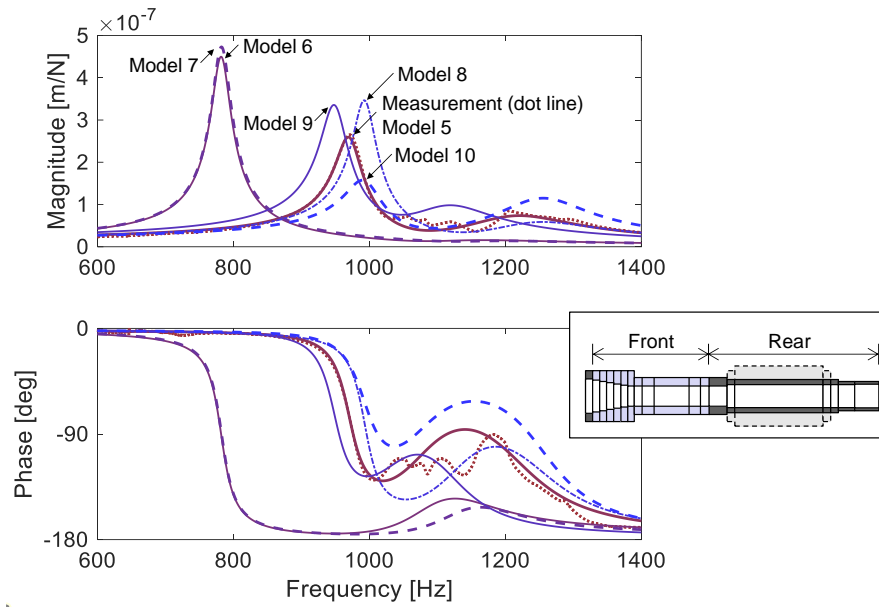


Fig. 4-14 Comparison of the spindle shaft models on the spindle unit.

Table 4-6 Comparison results and description of spindle shaft models

Model	Frequency [Hz]	Compliance [m/N]	Explanation of shaft
5	970	2.61×10^{-7}	Model 3
6	782	4.50×10^{-7}	Steel shaft
7	783	4.73×10^{-7}	Steel / CFRP±45° with sleeve
8	992	3.47×10^{-7}	Model 3 / CFRP±45° with sleeve
9	948	3.36×10^{-7}	Model 2
10	991	1.57×10^{-7}	Change to half sleeve thickness of model 3

anisotropy of bearings and the CFRP in the spindle shaft.

Figure 4-14 shows a comparison of the spindle shaft models in the CFRP application. Table 4-6 lists the comparison results and description of spindle shaft models. The bearing properties obtained in they-axis direction were used in the spindle unit models. Model 6 of steel was developed using the same dimensions; the parameter of structural damping $\zeta = 4.5 \times 10^{-4}$ was used. Compared to model 6, the maximum magnitudes of model 5 improved by 42%. In terms of the stability limit, it can be said that the CFRP spindles can be used for machining using a higher material removal rate. The original design was intended for application in the front parts, as shown in Fig. 4-14. Models 7 and 8 recalculated the rear parts of model 6 and 7 to CFRP with the steel sleeve, respectively. The maximum magnitudes and resonant frequencies increased, especially for model 5 when the CFRP was used in the front parts. In order to obtain a high dynamic stiffness, the rear parts require a high shear stiffness and mass. The front parts of model 9 uses the volume model to the shaft: smaller shear stiffness values compared to model 5, as presented in Table 4-2.

Although there is no significant difference in the FRFs and mode shapes of model 2 and 3, switching the models with different assumptions is inappropriate on the spindle unit because bearing properties contains modeling errors. The sensitivity of bearing properties depends on the accuracy of the spindle model. In addition, a smaller shear stiffness results in an increase in the compliance of the CFRP spindle unit. The maximum magnitudes on the machine tool are highly correlated with the spindle shaft dynamics of the front parts. In case of model 10, the volume ratio of the CFRP of the front parts increased and the sleeve thickness of the front parts was 1 mm, which is half of that of model 5. The maximum magnitudes of the spindle unit improved by 65% compared to that of model 6. Another model swapping stacking sequence of $\pm 30^\circ$ and $\pm 45^\circ$ on model 5 can be used to improve the compliance by 5.22×10^{-9} , but this can lead to a decrease in the resonant frequency by 1 Hz. It is known that the assembly close to the fix end conditions are desired to improve the dynamics of spindle units [94]. The lightweight structure at the rear side deteriorates the dynamics but that at the front side can improve. Optimizing the stacking sequence in the applicable location and the bearing position contributes to a further improvement in the dynamic stiffness at the spindle nose.

The receptance matrix of spindle shafts based on generalized receptance coupling to multiple points can be used for the bearing properties combination to enable optimization procedures for parameter identification and visualization of mode shapes. The FRFs were varied depending on idle time after stopping the spindle rotation, whose influences appear in the front bearing properties. In terms of the spindle design, the CFRP application improves the dynamical stiffness when CFRP is used in the front bearings.

4.5. Summary

This chapter describes dynamical analysis and modeling of CFRP spindle units. The dynamical models of the motorized CFRP spindle units are proposed. The dynamical models of CFRP spindle shafts and CFRP spindle units were experimentally validated. The contents are summarized as follows.

- Mechanical property of composite materials was formulated by the volume ratio or layouts of the Timoshenko beam models. The mechanical property identification was proposed to partly replace the analytical models and to use general solutions, which can drastically reduce the computational costs of dynamical analysis of CFRP spindle shafts compared to commercial FEA software.
- Multipoint receptance coupling was proposed. Both FRFs and mode shapes were observed by redefining the receptance coupling. The proposed method can avoid the

4. Dynamical analysis and modeling of CFRP spindle units

approximation of the dynamic system and the number of calculations for combining the bearings. Moreover, the bearing properties and contact characteristics assumed spring–damper systems can be experimentally identified by using multipoint receptance coupling.

- Four types of analytical spindle shaft models following the actual development phase were prepared. The impact test results of the CFRP spindle shaft as free-end conditions indicate that the volume model assuming uniform distribution on the applicable location performs a more accurate estimation of natural frequencies and mode shapes compared to that with the FEA. The layers model considering stacking sequences was robust against the parameterization errors of CFRP, as confirmed by the sensitivity analysis.
- The analytical models of the spindle unit were developed by combining the spindle shaft models with the rotor model and bearing properties. The bearing properties were identified from the FRFs of the impact tests based on the optimization procedure, which is applicable to the investigation of bearing property behavior. Two resonant peaks of the FRFs at the spindle nose were measured, and their mode shapes were investigated by generalized receptance coupling to multipoint.
- The effect of CFRP application was revealed by comparing it with the steel spindle shaft model and models designing the layout of CFRP. The comparison results indicated the improvement of dynamic stiffness and the proposals of layout for further improvement.

5. Dynamical analysis and modeling of spindle units including thermomechanical effects

5.1. Experimental modeling method of spindle unit dynamics including thermomechanical effects

In Section 3.2, the correlation with thermal errors and temperature around the CFRP spindle unit indicated thermal expansion of the spindle-bearings system, as shown in Fig. 3-4. Moreover, the spindle dynamics considering the mechanical properties of CFRP was modeled in Section 4.2. The bearing properties can be experimentally obtained by the identification procedures with the dynamical model.

By performing impact tests under temperature fluctuation, the bearing properties are discussed through temperature measurements as the information for thermomechanical effects. In addition, an application of the proposed regression models, spindle unit dynamics including thermomechanical effects, to SLDs for high-efficiency machining is proposed.

5.1.1. MLR models for bearing properties including thermomechanical effects

The estimation models of bearing properties from temperature data are developed by employing MLR. MLR is a statistical technique that assumes a linear relationship between the inputs and the output. In machine learning, it is implemented in algorithms to predict response variables. In this study, the identified bearing properties are expressed as the product of temperature data and coefficients in a sample j as follows:

$$\begin{Bmatrix} kt_i^{(j)} \\ ct_i^{(j)} \\ kr_i^{(j)} \\ cr_i^{(j)} \end{Bmatrix} = \mathbf{b}_i \mathbf{x}^{(j)} = \begin{bmatrix} bkt_0 & \cdots & bkt_m \\ bct_0 & \cdots & bct_m \\ bkr_0 & \cdots & bkr_m \\ bcr_0 & \cdots & bcr_m \end{bmatrix} \begin{Bmatrix} 1 \\ T_1^{(j)} \\ \vdots \\ T_m^{(j)} \end{Bmatrix} \quad (5-1)$$

Here, m is the number of sensor information used in MLR models. To obtain the appropriate coefficients \mathbf{b}_i , the minimization problem of the difference between the estimation and the measurements is solved.

Figure 5-1 outlines the procedure of the model construction. Impact tests were performed by varying the temperature, and bearing properties were obtained by the

5. Dynamical analysis and modeling of spindle units including thermomechanical effects

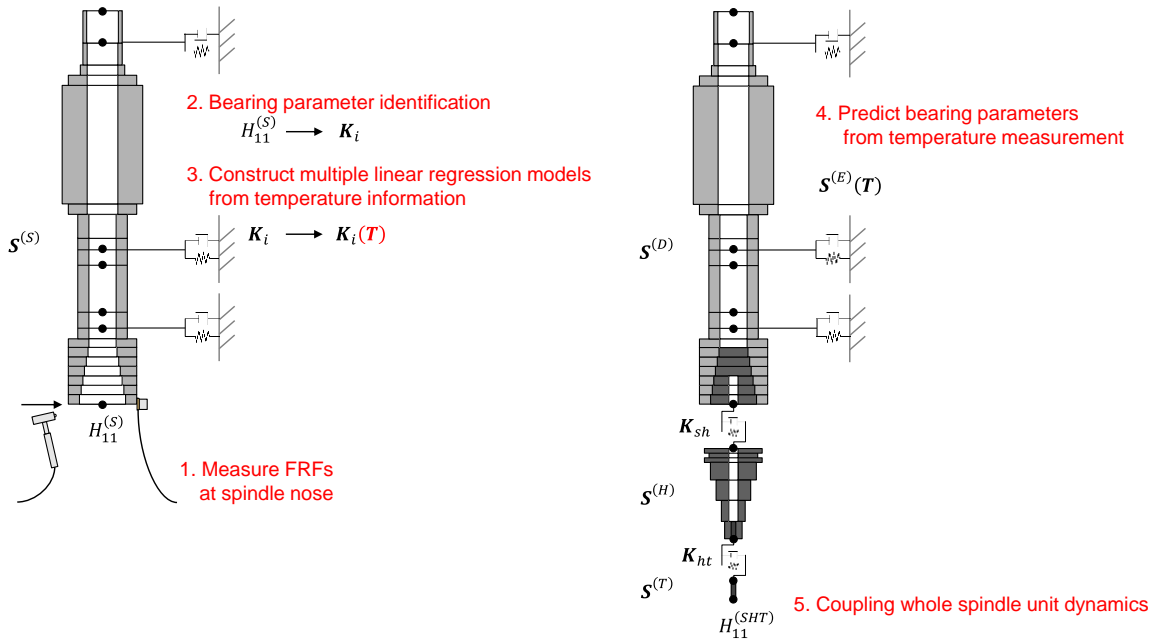


Fig. 5-1 Dynamical model construction of spindle units including thermomechanical effects; left side diagram shows the procedure of the regression model construction; right side diagram shows the procedure for the estimation of FRFs at tool tips.

identification procedure discussed. Next, the MLR models of bearing properties were trained on temperature data. In the next phase, the bearing properties were estimated from the temperature measurements. The dynamics of the whole spindle unit system were calculated by receptance coupling, and subsequently the FRFs at the tool tips were estimated.

5.1.2. Stability lobe diagrams for predicting stable processes and a novel design of discrete spindle speed tuning

For SLDs in the milling process (Figs. 1-9 and 1-10), the zeroth-order approximation analysis was proposed under the assumption of a single dominant frequency [57]. It is known that chatter grows in a frequency ω_c , and the displacement vector is approximated to $\Delta \mathbf{x}_0 e^{-i\omega_c t}$. In the milling process with a constant spindle rotation, the cutting force coefficient matrix comprises a direct current (DC) component and an alternate current (AC) component in the frequency of the rotational speed and its harmonics. However, the cutting force coefficient matrix often contains its DC component \mathbf{F}_{DC} . Owing to the machine tool dynamics working as a band-pass filter, the transfer function amplifies only around the resonant frequency. Note that the machine tool dynamics corresponds to the FRFs at the tool tip. Therefore, the critical condition of axial depth of cut $a_p = a_{lim}$ can be expressed by substituting Equation (1-5) into Equation (1-4) as follows:

5. Dynamical analysis and modeling of spindle units including thermomechanical effects

$$\mathbf{F}_{DC} = \frac{1}{2} a_{lim} K_{tc} (1 - e^{-j\omega_c T_a}) \begin{bmatrix} a_{xx} & a_{xy} \\ a_{yx} & a_{yy} \end{bmatrix} \begin{bmatrix} H_{xx}(s) & H_{xy}(s) \\ H_{yx}(s) & H_{yy}(s) \end{bmatrix} \mathbf{F}_{DC} \quad (5-2)$$

This equation has a non-trivial solution if its determinant is not zero.

$$\det \left[[I] + \Lambda \begin{bmatrix} a_{xx} & a_{xy} \\ a_{yx} & a_{yy} \end{bmatrix} \begin{bmatrix} H_{xx}(s) & H_{xy}(s) \\ H_{yx}(s) & H_{yy}(s) \end{bmatrix} \right] = 0 \quad (5-3)$$

where Λ is the reciprocal of the eigenvalues. The values are equal to the term as follows:

$$\Lambda = \text{Re}(\Lambda) + j\text{Im}(\Lambda) = -\frac{1}{2} a_{lim} K_{tc} (1 - e^{-j\omega_c T_a}) \quad (5-4)$$

The DC component of the cutting force coefficient matrix is obtained from the integration from the cutting start angle ϑ_{st} to the cutting end angle ϑ_{ex} for each tooth.

$$\begin{aligned} a_{xx} &= \frac{n_T}{4\pi} \left[\cos 2\vartheta - 2 \frac{K_{rc}}{K_{tc}} \vartheta + \frac{K_{rc}}{K_{tc}} \sin 2\vartheta \right]_{\vartheta_{st}}^{\vartheta_{ex}} \\ a_{xy} &= \frac{n_T}{4\pi} \left[-\sin 2\vartheta - 2\vartheta + \frac{K_{rc}}{K_{tc}} \cos 2\vartheta \right]_{\vartheta_{st}}^{\vartheta_{ex}} \\ a_{yx} &= \frac{n_T}{4\pi} \left[-\sin 2\vartheta + 2\vartheta + \frac{K_{rc}}{K_{tc}} \cos 2\vartheta \right]_{\vartheta_{st}}^{\vartheta_{ex}} \\ a_{yy} &= \frac{n_T}{4\pi} \left[-\cos 2\vartheta - 2 \frac{K_{rc}}{K_{tc}} \vartheta - \frac{K_{rc}}{K_{tc}} \sin 2\vartheta \right]_{\vartheta_{st}}^{\vartheta_{ex}} \end{aligned} \quad (5-5)$$

Here, the torsional angle of the cutting edge is assumed as 0° , and its specific cutting force is K_{tc} in the tangential direction and K_{rc} in the radial direction. From Equation (5-4), the critical axial depth of cut a_{lim} , the phase difference between the displacements of cutting edges ε , and the rotation speed S can be obtained by solving the real and imaginary parts of the simultaneous equations.

$$a_{lim} = -\frac{\text{Re}(\Lambda)}{K_{tc}} \left\{ 1 + \left(\frac{\text{Im}(\Lambda)}{\text{Re}(\Lambda)} \right)^2 \right\} \quad (5-6)$$

$$\varepsilon = \pi - 2 \tan^{-1} \frac{\text{Im}(\Lambda)}{\text{Re}(\Lambda)} \quad (5-7)$$

$$S = \frac{60\omega_c}{n_T(2k_c\pi + \varepsilon)} \quad (5-8)$$

5. Dynamical analysis and modeling of spindle units including thermomechanical effects

According to process planning by SLDs, the machining conditions with high MRR are selected from the stable spindle speeds in stability pockets. However, the stability pockets could shift in high frequencies after spindle rotation owing to the increase of resonant frequencies at the TCP. On the CFRPMT, the FRFs in the Y-axis have a higher degree of compliance and can be better estimated than those in the X-axis by the proposed models of spindle unit dynamics. To compensate the inaccuracy of SLDs in process, the optimal spindle rotational speed is updated by Equation (5-9).

$$S_{new} = \frac{60(f_r - f_o)}{n_r k_c} \quad (5-9)$$

Here, the resonant frequency of machine tool dynamics is extracted from the models. The oscillation in resonant frequency is avoided by subtracting the offset value of frequency $f_o = 20$ Hz, where the sign is decided by considering the lower resonant frequency in the X-axis direction than that in the Y-axis direction in section 5.4. The proposed models can compensate preidentified machine tool dynamics from temperature information and enhance the productivity by the DSST approach in process.

5.2. Experimental analysis of thermomechanical effects on bearing

An application for energy saving is an on/off control scheme for a hot-gas bypass cooling system to operate them at the optimal point of the coefficient of performance as heat exchange [18]. From the perspective of thermal expansion, constant low-heat sources to give the repeatability of thermal deformation behaviors will be eliminated. The variations in dynamic properties of the latest machine tools with respect to abrupt temperature changes in volatile environments such as by the intermittent operation of the cooling system must be discussed.

In this section, impact tests were conducted on a spindle unit under temperature fluctuations. The conditions were warmup from cold start, standby under idle conditions, and idle reduction, where the chiller stops under the idle conditions. The dynamic properties of bearings are discussed from the behavior of FRFs with temperature measurement.

5.2.1. Experimental setup for impact tests at spindle nose

In the similar manner to the impact tests as shown in Fig.4-11, the spindle nose was excited using an impulse hammer (5850B4, Dytran Instruments), and the accelerations

5. Dynamical analysis and modeling of spindle units including thermomechanical effects

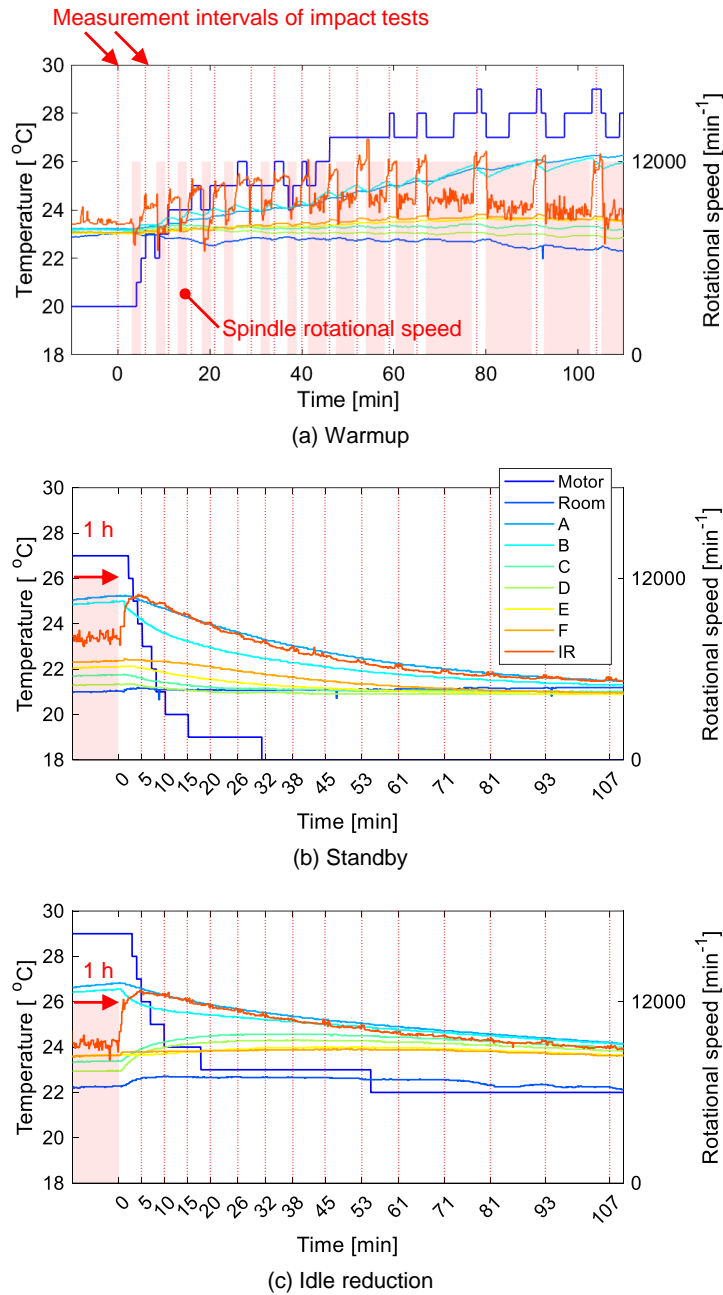


Fig. 5-2 Temperature conditions of (a) warmup; (b) standby; (c) idle reduction of the chiller as experimental conditions of impact tests.

along the X- and Y-axes were measured using a piezoelectric accelerometer (NP-3412, ONO SOKKI). The FRFs from the excitation force to the displacement were obtained by double integration. The sampling frequency and number of sample points were set to 12.8 kHz and 16384, respectively. The FRFs from the five measurements were averaged using a FFT analyzer (DS-3000, ONO SOKKI).

Figure 5-2 illustrates temperature and rotational speed as the experimental conditions. The impact tests are performed in the X- and Y-axis directions sequentially every 1 min. The measurement intervals are represented by red dotted lines. Under the warmup

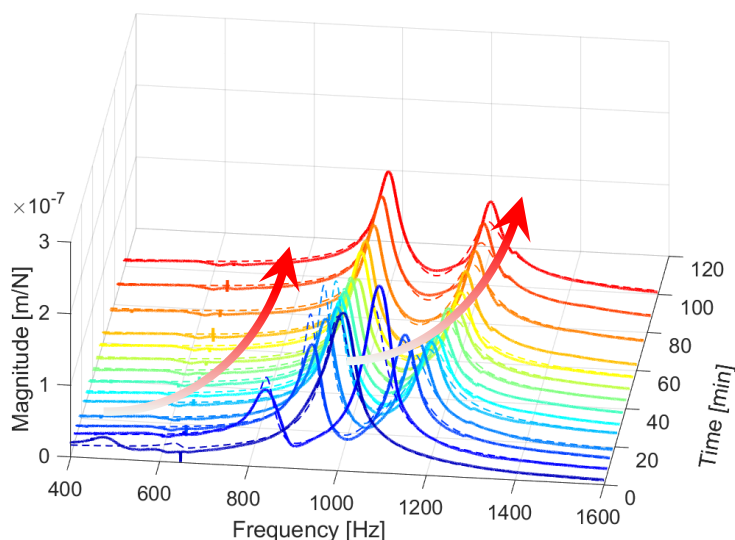


Fig. 5-3 Measurement results under the condition of warmup in the X-axis; solid lines represent the measurements, and dotted lines the models.

condition in Fig. 5-2(a), an impact test was performed in the cold state of the CFRP machine tool. Next, the main spindle was rotated at 12000 min^{-1} for 2 min and then stopped. Subsequently, the impact test was performed. This operation was repeated while the motor temperature increased and the duration was changed to 4 and 10 min to control the housing temperature (A and B) in a linear increase. Fourteen FRFs were obtained in the two directions.

For the idle conditions, the spindle was operated under standby and idle reduction after an hour of rotation to stabilize the thermal expansion. Temperature C–F on the cast metal decrease under standby, by contrast, increased under idle reduction because the chiller was halted. By using measurement results in Chapter 3, the time constants of thermal errors in the Y- and Z-axes modeled by a first-order lag system were 88.0 and 14.3 min^{-1} , respectively. Impact tests were performed at specific intervals after stopping the spindle rotation, which corresponded to 5%–70% by 5% of response of the thermal error model in the Y-axis against a constant spindle rotation of 12000 min^{-1} as a step command. Consequently, 14 FRFs were obtained in each condition.

5.2.2. Discussion of FRFs under temperature fluctuations

Figure 5-3 shows the magnitudes of FRFs in the X-axis under warmup. At cold start (0 min), the two peaks of compliances were 0.301 and $2.22 \times 10^{-7} \text{ m/N}$ at 475 and 1015 Hz , respectively. As the temperature increased, the resonant frequency increased, and the vibration mode with the highest peak changed from second to first. This behavior nearly

5. Dynamical analysis and modeling of spindle units including thermomechanical effects

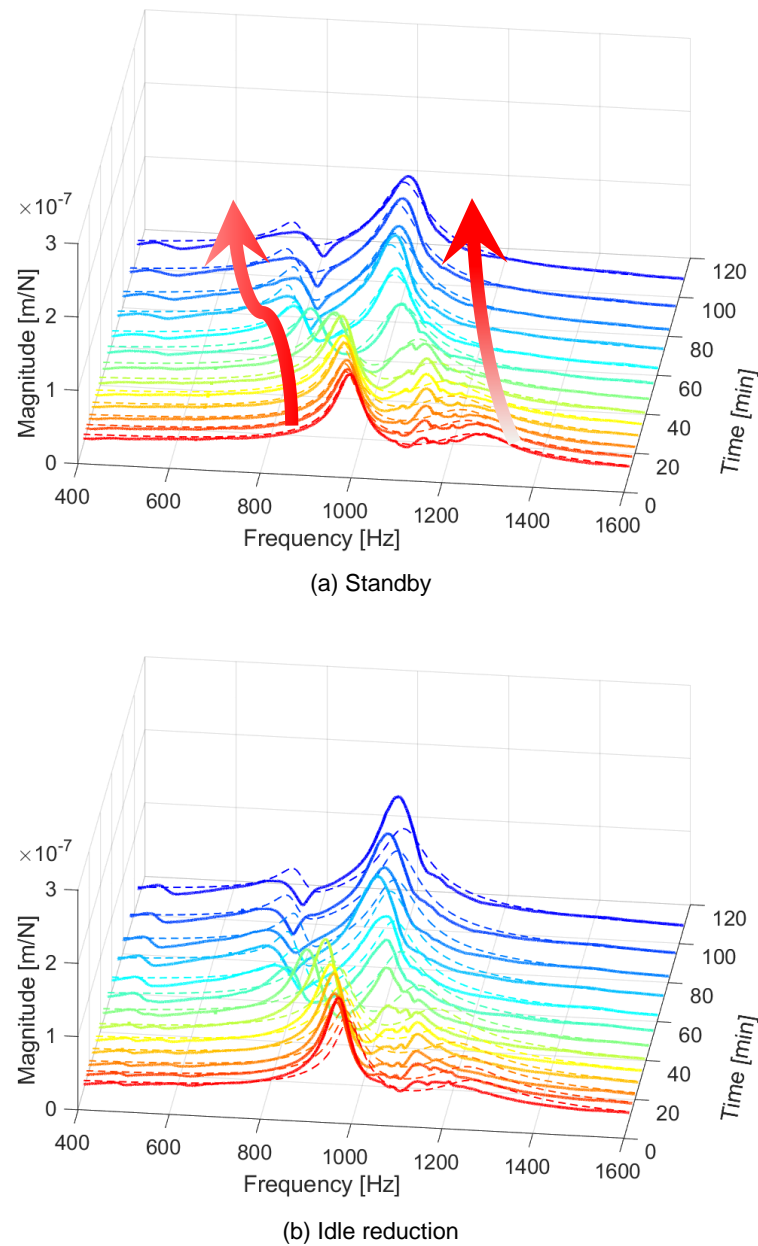


Fig. 5-4 Measurement results under the conditions of (a) standby; (b) idle reduction in the Y-axis; solid lines represent the measurements, and dotted lines the models.

saturates at the fifth measurement; the accumulated time of spindle rotation was 10 min, where the two peaks of compliance were 1.62 and 1.19×10^{-7} m/N at 971 and 1186 Hz, respectively. After the fifth measurement, temperatures A and B on the housing continued to increase as shown in Fig. 5-2(a). Generally, as mentioned in a keynote study [24], the thermal expansion of mechanical parts changes the bearing preload and bearing ring curvature. The resulting contact angle variation induced by the temperature increase decreased the resonant frequencies and stiffness in the DTBT configurations with the position preload [10], [24], [95]. However, the results in Fig. 5-3 shows the opposite trend to

5. Dynamical analysis and modeling of spindle units including thermomechanical effects

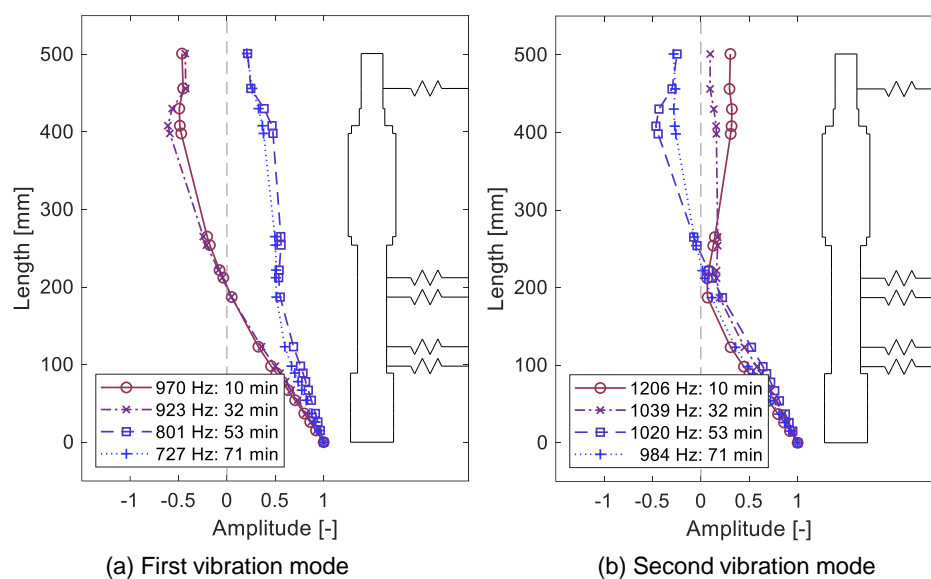


Fig. 5-5 Mode shapes of the mounted CFRP spindle shaft under temperature change along the Y-axis.

those on conventional steel shafts. Another study reported an increase in the resonant frequency of a CFRP spindle shaft [10]. This means the thermal deformation behavior changes due to the difference between the thermal expansion coefficients of CFRP and steel spindle shafts. A comparison with the conventional steel spindle shafts revealed that the CFRP shaft had a smaller thermal expansion coefficient in the rotational axis direction and a larger coefficient in the radial direction. The latter induced the increase in the resonant frequency.

Furthermore, as the thermal error model in the Z-axis, the time constant of thermal expansion around the bearings is smaller than that of the whole spindle unit. We suppose that a warmup operation for 10 min or more is mechanically effective in eliminating the thermomechanical effects on the dynamics. The thermal expansion of the spindle shaft with the bearings that affects the resonant frequencies stabilizes rapidly.

Figure 5-4 displays the magnitudes of FRFs in the Y-axis under idle conditions. The behavior of the FRFs is not affected by the operation of the chiller. At the first measurement (5 min) under standby, the compliances of the two peaks were 1.15 and 0.428×10^{-7} m/N at 986 and 1279 Hz, respectively. As the spindle unit was cooled, the resonant frequency reduced and the vibration mode with the highest peak shifted from first to second after the measurement (44 min). After stopping the spindle rotation for 2 h, the FRFs were similar to those at cold start. This trend was also observed in the X-axis. These results suggest that the bearings expanded faster than they contracted, owing to the temperature changes in the surrounding components. The motor stator and cast metal were effectively cooled by the chiller, although the heat radiated toward the housing. The resonant frequency with the

5. Dynamical analysis and modeling of spindle units including thermomechanical effects

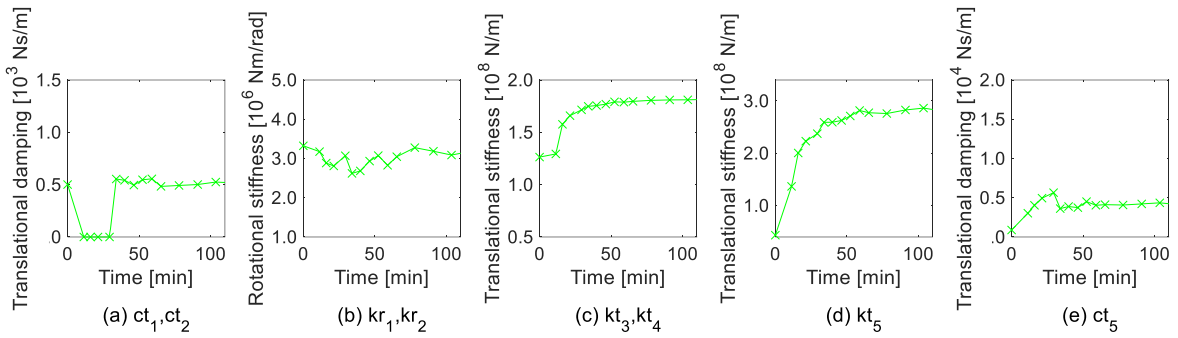


Fig. 5-6 Bearing properties in the X-axis under the condition of warmup.

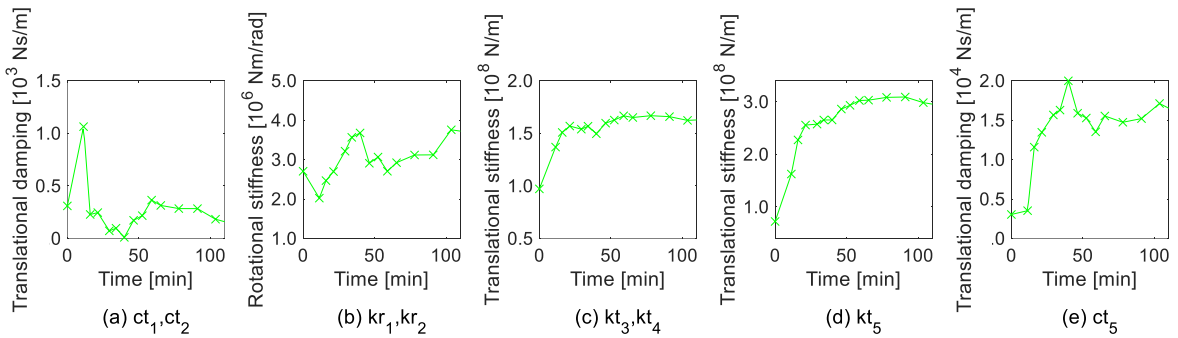


Fig. 5-7 Bearing properties in the Y-axis under warmup.

maximum magnitude was maintained at approximately 1000 Hz by switching the vibration modes as shown in Fig. 5-5, where the spindle shaft models with identified bearing parameters are used for the illustration. The influence of this behavior on the FRFs at the tool tips should be discussed.

5.2.3. Results of bearing property identification

As illustrated in Figs. 5-3 and 5-4 (dotted lines), the identification of the bearing properties for Eq. (4-36) was performed. In the beam models of the spindle unit, the spindle shaft was supported by five spring–damper systems that simulated the bearing configurations. From the spindle nose in the spindle unit, three parameters representing the bearing properties were assumed: $\mathbf{K}_1 = \mathbf{K}_2$ for the two front bearings on the front, $\mathbf{K}_3 = \mathbf{K}_4$ for the two front bearings on the rear, and \mathbf{K}_5 for the rear bearings. Therefore, the spindle unit model had 12 equivalent parameters, including a kinematic approximation with modeling errors on the bearings formulated in Equations (4-32) and (4-33). As shown in the identified results in Table 5-4, a few identified parameters exhibited a correlation with the idle time, whereas others changed vibrationally. The selection of effective bearing

5. Dynamical analysis and modeling of spindle units including thermomechanical effects

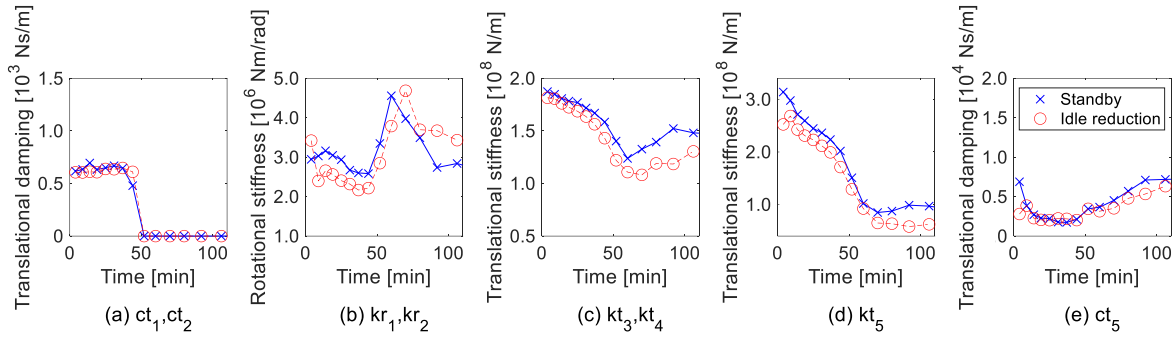


Fig. 5-8 Bearing properties in the X-axis under the conditions of standby and idle reduction.

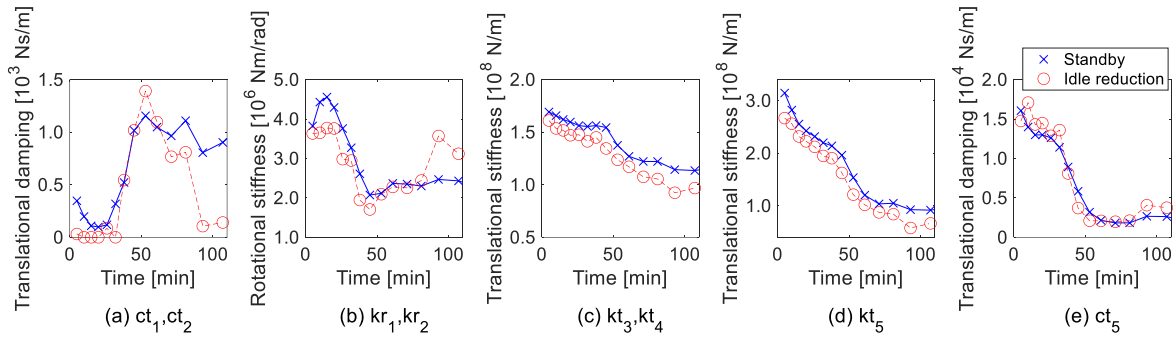


Fig. 5-9 Bearing properties in the Y-axis under the conditions of standby and idle reduction.

properties to reduce objective variables must contribute to the repeatability of regression models.

Based on numerical variations of the identified bearing properties, the dynamic behavior of system properties within the measured frequency bandwidth is discussed. The rotational stiffness kr_5 does not affect the FRFs if the value has an insufficient magnitude. The rotational damping cr is negligible. The translational damping coefficients $ct_{1,2}$ and $ct_{3,4}$ can replace each other. Second, the identification procedure was repeated using seven variables; $ct_{3,4}$ and cr were fixed to 10^{-5} , and kr_5 to 10^5 . This result reveals that the translational stiffness $kt_{1,2}$ and rotational stiffness $kr_{3,4}$ were approximately 0. Finally, the identification procedure was repeated using five variables; $kt_{1,2}$ and $kr_{3,4}$ were fixed to 10^{-5} , and $ct_{1,2}$, $kr_{1,2}$, $kt_{3,4}$, kt_5 , and ct_5 were identified from each FRF.

Figs. 5-6–5-9 present the identified parameters under temperature changes. Under warmup, as illustrated in Figs. 5-6 and 5-7, $kt_{3,4}$, kt_5 , and ct_5 follow trends similar to those of temperature “Motor.” The equivalent translational stiffness significantly increased with the temperature. $ct_{1,2}$ and $kr_{1,2}$ have no clear time dependability to spindle rotation. Under the idle conditions in Figs. 5-8 and 5-9, $kt_{3,4}$, kt_5 , and ct_5 decreased as the idle time increased. In the X-axis, $ct_{1,2}$ became zero when the temperature conditions were close to cold start. Moreover, $kt_{3,4}$ and ct_5 show the different tendency after 50 min. The

5. Dynamical analysis and modeling of spindle units including thermomechanical effects

behaviors of equivalent parameters have structural anisotropy. The chiller can be toggled between on and off states with little effect on the dynamic properties of the spindle. The on/off control scheme for energy saving need not consider its influence on changes in the dynamic properties.

5.3. Regression model construction of thermomechanical effects on bearing properties

This section presents the construction of regression models from temperature information based on the results of the identification of five equivalent bearing properties. To ensure an adequate number of data points, the parameters were linearly interpolated based on the time of measurement. Temperature data were down-sampled to 1 min. A dataset of 130 points under the warmup condition and 102 under each idle condition was prepared. The selection of temperature sensors and the preparation of explanatory variables for MLR were discussed. The developed regression model enabled the estimation of bearing properties from temperature information. The contact characteristics at the interface were also identified, to couple the receptance matrices of the spindle unit up to the tool tip.

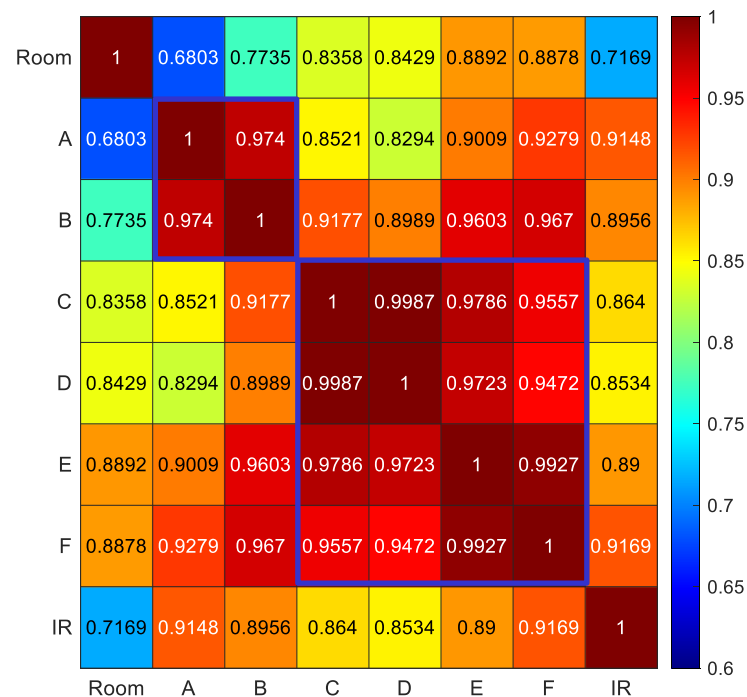


Fig. 5-10 Autocorrelation coefficients of temperature signals.

5. Dynamical analysis and modeling of spindle units including thermomechanical effects

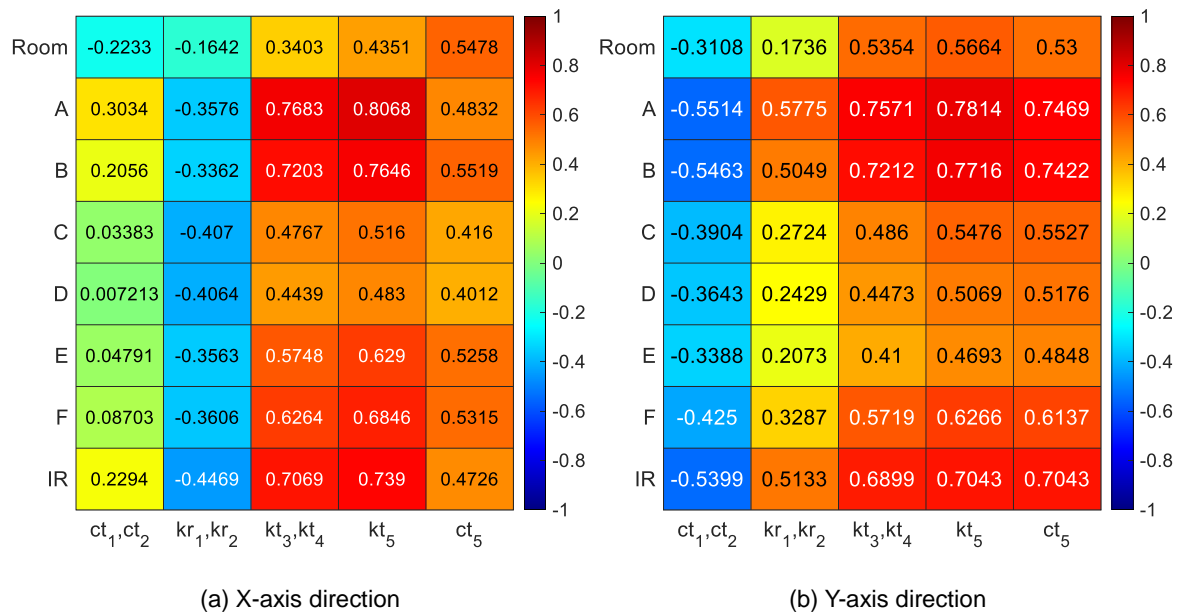


Fig. 5-11 Cross-correlation coefficients between temperature signals and behaviors of the five equivalent parameters predicted (a) in the X-axis direction; (b) in the Y-axis direction.

5.3.1. Selection of effective temperature sensors for MLR

Temperature sensors were difficult to internally retrofit and were mounted on the surface of the spindle unit. Multicollinearity must be avoided when explanatory variables share strong correlations with each other. Figure 5-10 shows the autocorrelation coefficients of the temperature sensors. The coefficients were calculated from a time series of temperature data through experiments shown in Fig. 5-2. The coefficients of temperatures IR and Room were less than 0.9, and the corresponding two sensor signals were relatively independent from the rest. Moreover, two groups of temperatures A and B, as well as C–F, revealed large values; one temperature signal was selected from each group.

Figure 5-11 shows the cross-correlation coefficients between temperature signals and the behaviors of five equivalent parameters. A comparison of the coefficients in the X- and Y-axes reveal higher values in the latter. Hence, the kinematic assumption of the proposed models is more applicable in the Y-axis. The machine construction supporting the spindle unit using a saddle and column in the Y-axis is considered close to the condition of a fixed end. The identified properties mainly possess the information of the bearing characteristics. Regarding the coefficients, temperature A is higher than temperature B. Temperature F is better than the rest in its group. Based on these coefficients, we selected the signals of temperatures IR, A, F, and Room as the explanatory variables of MLR.

5. Dynamical analysis and modeling of spindle units including thermomechanical effects

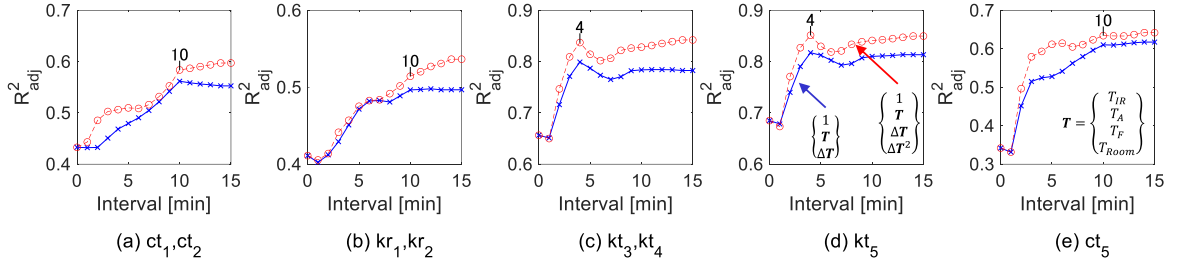


Fig. 5-12 Adjusted coefficients of determination under varying intervals of differential information in the X-axis; the selected intervals are annotated.

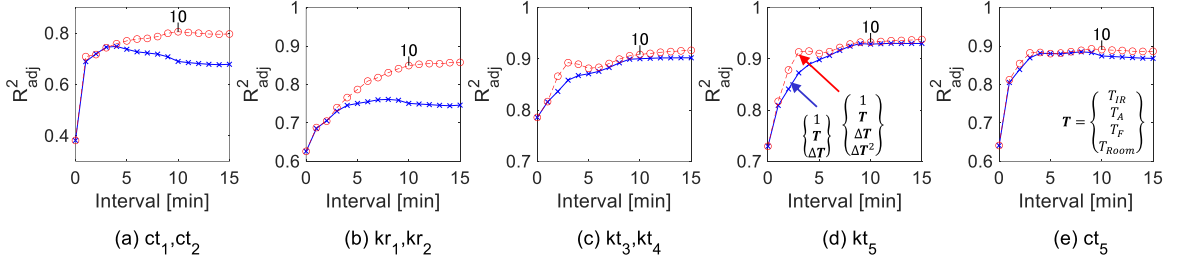


Fig. 5-13 Adjusted coefficients of determination under varying intervals of differential information in the Y-axis; the selected intervals are annotated.

5.3.2. Preparation of explanatory variables using differential information

Four temperature signals were used to express the spatial temperature distribution in the MLR models. In the viewpoint of the heat diffusion equation, regression models will benefit from the use of the differential information of time. Then, differential data of four temperature signals were prepared, and the coefficients of MLR were calculated by varying the interval τ_K to subtract previous data from current data. Figs. 5-12 and 5-13 show the optimized coefficient of determination under a varying interval τ_K . The equivalent parameters were modeled as Equation (5-1) using nine variables: four temperature information terms $\mathbf{T}(t)$, four temperature-difference information terms $\Delta\mathbf{T}(t) = \mathbf{T}(t) - \mathbf{T}(t - \tau_K)$, and one intercept term. As shown in the red lines of Figs. 5-11 and 5-12, the squared values of differential data $\Delta\mathbf{T}(t)^2$ are also validated, and 13 variables are used for the MLR models. Here, interval 0 min means the MLR models using five variables: four temperature information terms and one intercept term. The regression quality was improved using the differential data; especially, the squared values were better. The maximum values of the adjusted coefficients of determination were observed at a differential data interval of 10 min, except the intervals for $kt_{3,4}$ and kt_5 in the X-axis, which were 4 min each. Moreover, a longer interval than 10 min was not used considering the sensitivity of regression models. Thirteen explanatory variables using differential data

with the intervals of 4 and 10 min were used for the MLR models of five equivalent parameters in each direction. The obtained coefficients are summarized in Appendix D.

5.3.3. Contact characteristics identification on taper and collet at spindle–holder–tool interface

The analytical determination of contact characteristics at the holder–tool and spindle–holder interfaces is difficult. Therefore, impact tests were conducted with a setup similar to that in Fig. 4-11. In this setup, a holder (BBT40-MEGA13E-105, BIG DAISHOWA SEIKI) was clamped to the spindle nose. The acceleration of the holder end was measured by a piezoelectric accelerometer, and the FRFs from the excitation force to the displacement were obtained by double integration. The temperature conditions for the spindle–holder interface were at cold start and after warmup. Meanwhile, the spindle rotated constantly at 12000 min^{-1} for 1 h.

Figure 5-14 depicts the FRFs of the measurements and models with the identified contact parameters after warmup. The cost function for the contact parameters identification is similar to Eq. (4-36), where \mathbf{K}_{sh} is the variables. The identified bearing properties after 4 and 5 min in Figs. 5-8 and 5-9 were used in the models of the bearing–spindle–holder system. The calculation of the receptance matrices and dimensions of the beam models are summarized in Appendix E. Table 5-1 lists the contact parameters. Notably, the identified bearing properties at cold start in Figs. 5-6 and 5-7 were used to identify the contact parameters at cold start. These parameters were also varied with the temperature conditions. The results from the FRFs at cold start are also summarized in Table 5-2. The translational stiffness and damping after warmup were smaller than those at cold start. As mentioned earlier, the CFRP spindle shaft has a larger thermal expansion coefficient in the radial direction than conventional steel shafts. As illustrated in Fig. 5-2, the temperature IR increases by 2 °C in 3 min and equals temperature A. The saturation value of the housing with the spindle motor was higher than those of the front bearings with the spindle shaft. After the spindle was stopped, the heat of the housing radiated to the spindle shaft through the front bearings. The reduction of parameters was caused by thermal expansion around the interface. These parameters are affected by the thermal characteristics of the components.

Figure 5-15 depicts the mode shapes in the natural frequency ω_r , which were obtained from $H_{i1}^{(SH)}(\omega_r)$. The reference value of the phase is the point of impaction, and the magnitudes were divided by the value at the front-end of the holder. The external dimensions of the spindle and holder models and the experimental setup of the impact tests are illustrated on the right side of the figure. By generalizing receptance coupling to

5. Dynamical analysis and modeling of spindle units including thermomechanical effects

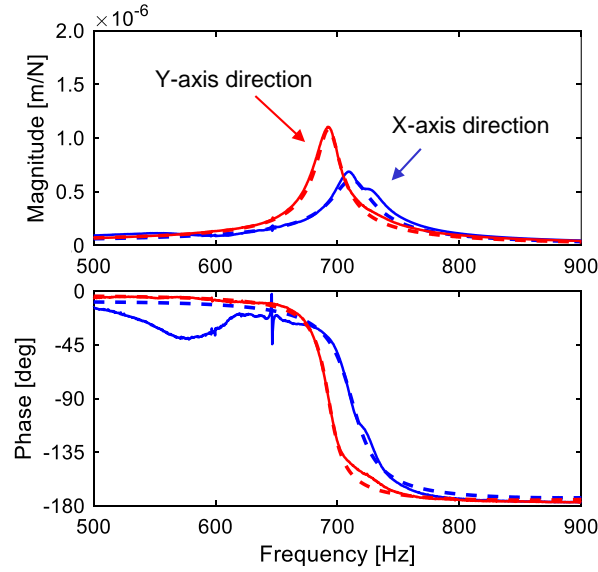


Fig. 5-14 FRFs at the holder end after warmup; solid lines are the measurements, and dotted lines the models.

Table 5-1 Contact parameters of the spindle–holder interface \mathbf{K}_{sh} after warmup

Direction	kt [N/m]	ct [Ns/m]	kr [Nm/rad]	cr [Nms/rad]
X-axis	4.05×10^8	3.47×10^4	2.99×10^5	8.24×10^2
Y-axis	1.25×10^8	3.56×10^3	8.63×10^5	2.35×10^3

Table 5-2 Contact parameters of the spindle–holder interface \mathbf{K}_{sh} at cold start

Direction	kt [N/m]	ct [Ns/m]	kr [Nm/rad]	cr [Nms/rad]
X-axis	5.14×10^8	4.10×10^4	2.53×10^5	5.99×10^2
Y-axis	1.89×10^8	8.31×10^3	4.10×10^5	1.03×10^3

multiple points, the receptance matrices of spindle units can be used to visualize the mode shapes. The measurements at the front-end of the holder and spindle nose confirmed the quality of the models.

A similar method was used to identify the contact parameters at the holder–tool interface. A square endmill (ASM4100DL, SUMITOMO ELECTRIC HARDMETAL) with a collet was mounted on the holder with a protrusion of 40 mm. The temperature condition is at cold start. The FRFs and setup are illustrated in Fig. 5-16 in the next section. The bearing properties in Fig. 5-7 and the contact parameters in Table 5-2 were used for the analytical model described in Appendix E. The contact parameters were identified by fitting $H_{11}^{(SHT)}$ to the measurement H_{meas} at the tool tip in the Y-axis. The cost function is similar to Eq. (4-36), where the variable is \mathbf{K}_{ht} . The identification results are summarized in Table 5-3.

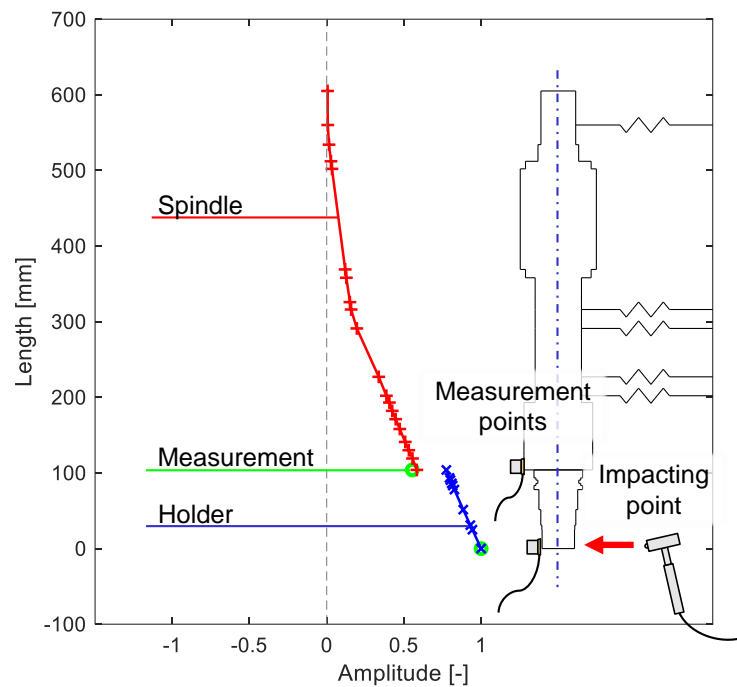


Fig. 5-15 Mode shapes of spindle–holder assembly at 692 Hz in the Y-axis.

Table 5-3 Contact parameters of the holder-tool interface K_{ht}

kt [N/m]	ct [Ns/m]	kr [Nm/rad]	cr [Nms/rad]
3.44×10^7	1.00	2.42×10^4	1.00

5.4. Estimation of FRFs at tool tips under temperature variation

This section validates the proposed models of the thermomechanical effects on bearings. The dynamics of the whole machine tool spindle unit are estimated by multipoint receptance coupling with a holder–tool model. The FRFs at the tool tip were estimated under a fluctuating temperature using the temperature information from the four sensors mounted on the surface of the spindle unit.

5.4.1. Experimental setup for impact tests at tool tips

Figure 5-16 displays the experimental setup of the impact tests. The tool tip was excited using an impulse hammer. The accelerations along the X- and Y-axes were measured using a piezoelectric accelerometer. The FRFs from the five measurements were averaged using the FFT analyzer.

Figure 5-17 shows temperature and spindle rotational speed as the experimental

5. Dynamical analysis and modeling of spindle units including thermomechanical effects

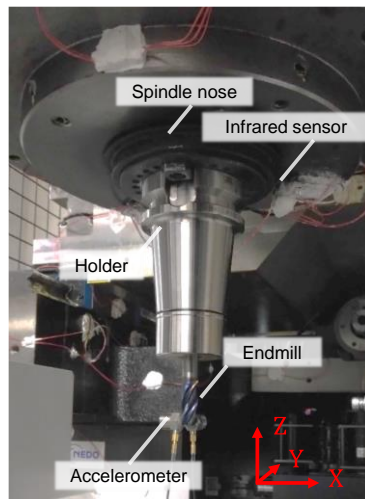


Fig. 5-16 Experimental setup of impact tests at the tool tip.

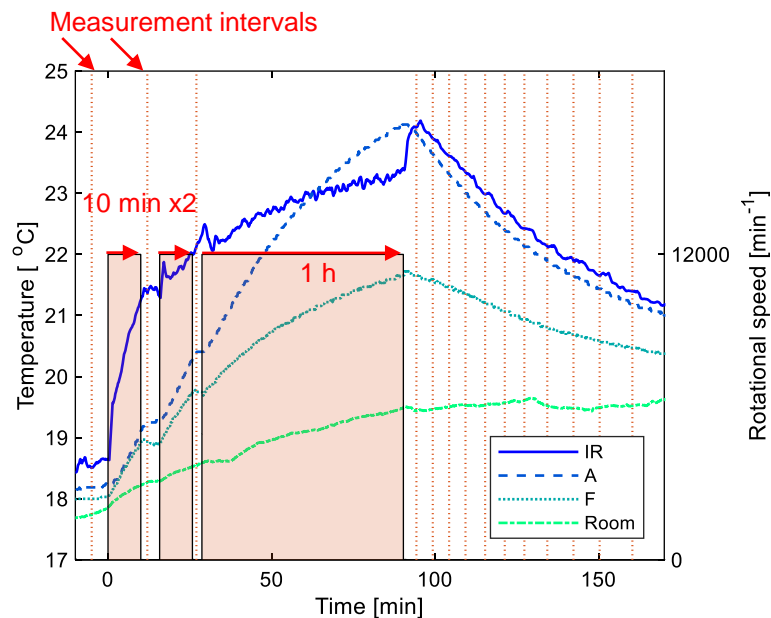


Fig. 5-17 Temperature and rotational speed as experimental conditions.

conditions. The tests were performed sequentially in the X- and Y-axes in intervals of 1 min. The measurement intervals are represented by red dotted lines. First, an impact test was performed at cold start. Next, the main spindle was rotated at 12000 min⁻¹ for 10 min, and then stopped. Subsequently, an impact test was performed. This operation was repeated once, and the spindle was rotated again for 1 h, and then stopped. The impact tests were performed at specific intervals, similar to the conditions in Fig. 5-2; however, the measurements in each direction were conducted 11 times by 71 min.

5. Dynamical analysis and modeling of spindle units including thermomechanical effects

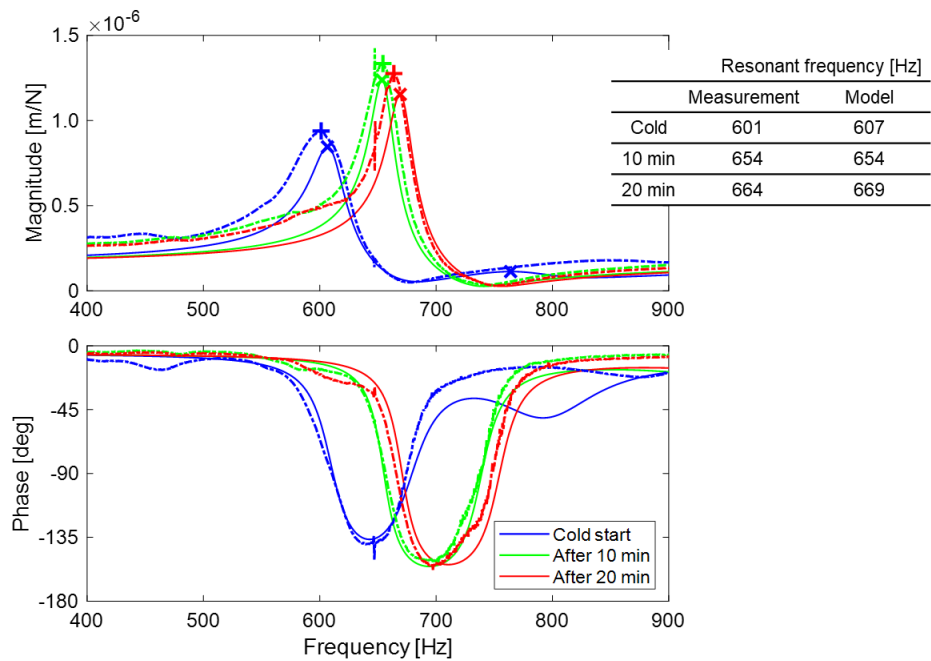
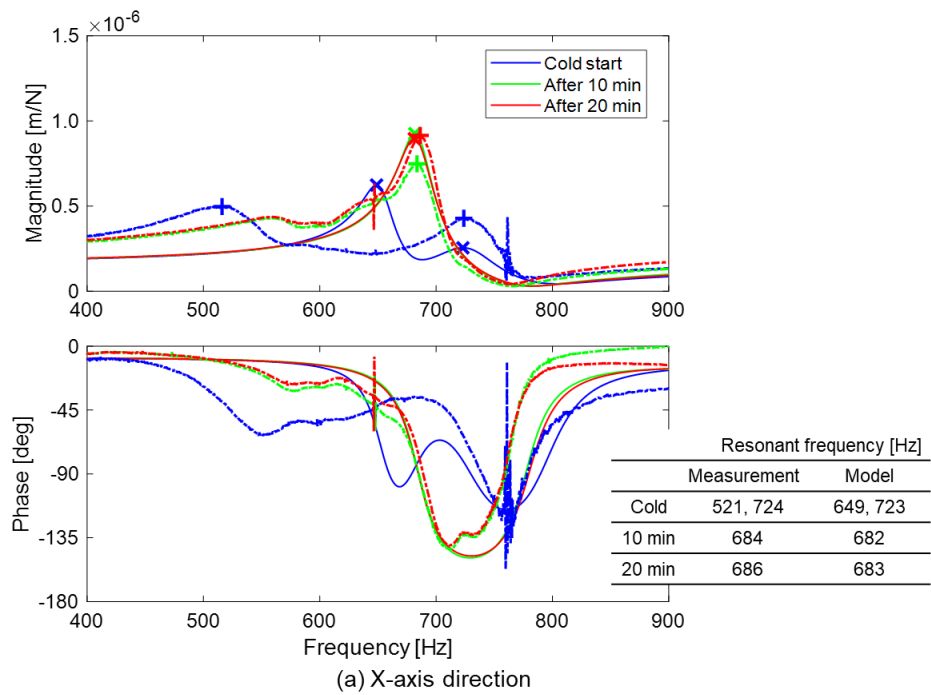


Fig. 5-18 FRFs at the tool tip under the condition of warmup; solid lines represent the models, and dotted lines the measurements.

5.4.2. Results under warmup operation

Figure 5-18(a) shows the FRFs in the X-axis. Two peaks of FRFs were observed at cold start. The model can express two peaks but does not estimate their resonant frequencies accurately. The frequencies are summarized in the figure. Only one peak was observed after the rotation is stopped. The magnitudes almost doubled, and the resonant frequency was

5. Dynamical analysis and modeling of spindle units including thermomechanical effects

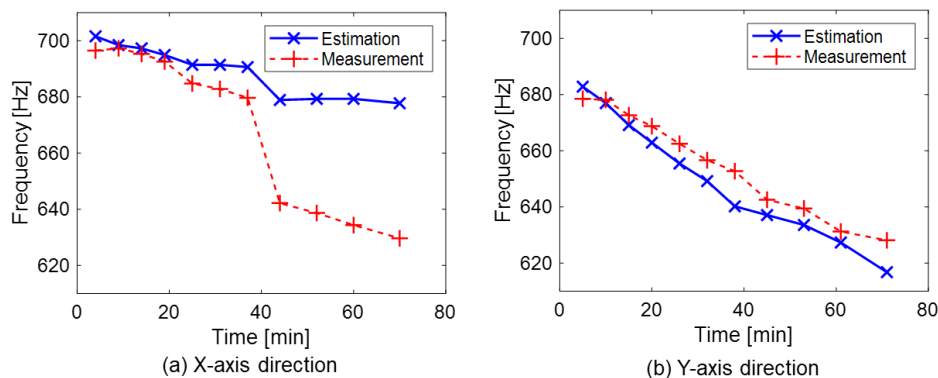


Fig. 5-19 Resonant frequencies of machine tool dynamics at the tool tip after stopping warmup operation; solid lines represent the estimations by the proposed models, and dotted lines the measurements.

approximately 865 Hz. The spindle only needed to be rotated for 10 min to stabilize the thermal behavior of the machine tool. Hence, the proposed models can estimate the FRFs after the first measurement. Furthermore, mechanical resonance around 760 Hz appears at cold start. The mechanics of bearings and contact characteristics in the X-axis become complex under the cold state.

Figure 5-18(b) illustrates the FRFs in the Y-axis. In the three measurements under warmup operation, the resonant frequencies sequentially changed to 601, 654, and 664 Hz. The proposed models maintained this behavior within an error margin of 10 Hz. However, the quality of estimation of curves could be improved by considering the kinematic models of tools and collets, as well as the kinematic assumption at the holder–tool interface. Nevertheless, the kinematic models with coupling as the spring–damper system up to the holder described the phenomenon accurately (Figs. 5-14 and 5-15). The identification of the precise material properties and dimensions of the tool with the collet is also considered.

5.4.3. Results after stopping warmup operation

Figure 5-19 shows the resonant frequencies of the highest peak versus time after the warmup operation is stopped. Compared with the first measurement at cold start, the resonant frequencies increased by 175 Hz to 696 Hz in the X-axis and by 78 Hz to 679 Hz in the Y-axis direction. The frequencies decreased with heat radiation. The results reveal that the proposed models can estimate the FRFs within an error margin of 10 Hz under the temperature changes of the spindle units. However, in Fig. 5-19(a), after 40 min, the measurements have two resonant frequencies, which are difficult to be expressed by the proposed models. The results in subsection 5.3.3 imply that the contact parameters of the spindle–holder interface at the taper were also influenced by the thermal effects. Moreover, the influence of changes in the contact parameters is also considered the cause of modeling

5. Dynamical analysis and modeling of spindle units including thermomechanical effects

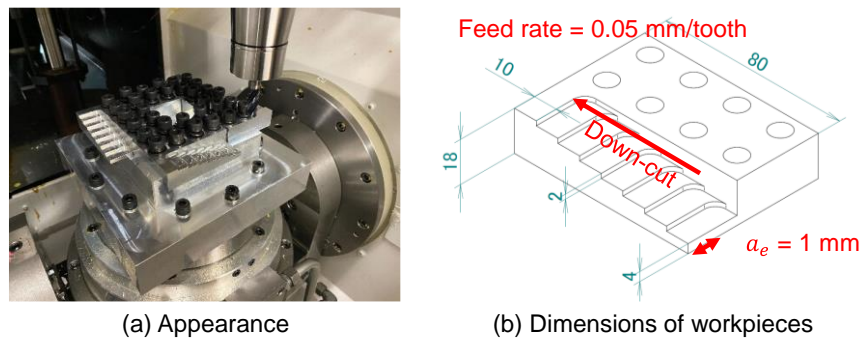


Fig. 5-20 Experimental setup for side milling tests.

errors. We have determined that the thermal expansion of the parts around the taper can induce the loose which kinematic model is similar to the joint at a point expressed in Equations (4-37) and (4-38). Moreover, most of the training dataset for MLR was collected after spindle rotation. Measurements at cold start and before a significant temperature increment under various ambient conditions should improve the regression models.

5.5. Application of the modeling of spindle unit dynamics including thermomechanical effects to stability lobe diagrams

This section validates the application of a novel DSST design through side milling tests. The estimation performance of FRFs at the tool tip and the variation of process stability are discussed against temperature fluctuation.

5.5.1. Experimental setup for side milling tests under temperature changes

Figure 5-20 shows the experimental setup for side milling tests. The same tool-holder assembly as Fig. 5-16 is employed. An accelerometer was attached to the spindle head and acceleration was measured at a sampling frequency of 6400 Hz. The side milling is conducted on step-shape workpieces at constant spindle rotation in dry cutting, as shown in Fig. 5-20(b). The material is aluminum alloy A5052. The axial depth of cut is changed from 4 to 18 mm by 2 mm. The process stability at each depth of cut can be measured from these milling test results.

Figure 5-21 shows temperature and spindle rotational speed as the experimental conditions. The side milling tests are conducted under three temperature conditions: at cold start, after spindle rotation for 10 min, and after spindle rotation for a total of 20 min. The

5. Dynamical analysis and modeling of spindle units including thermomechanical effects

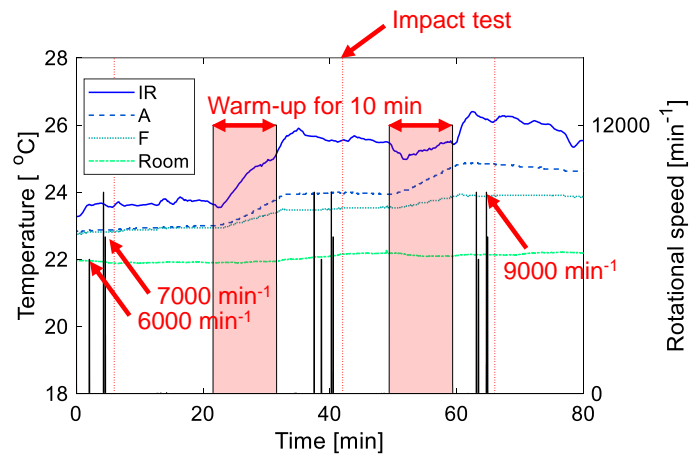


Fig. 5-21 Temperature and rotational speed as experimental conditions.



(a) Surface

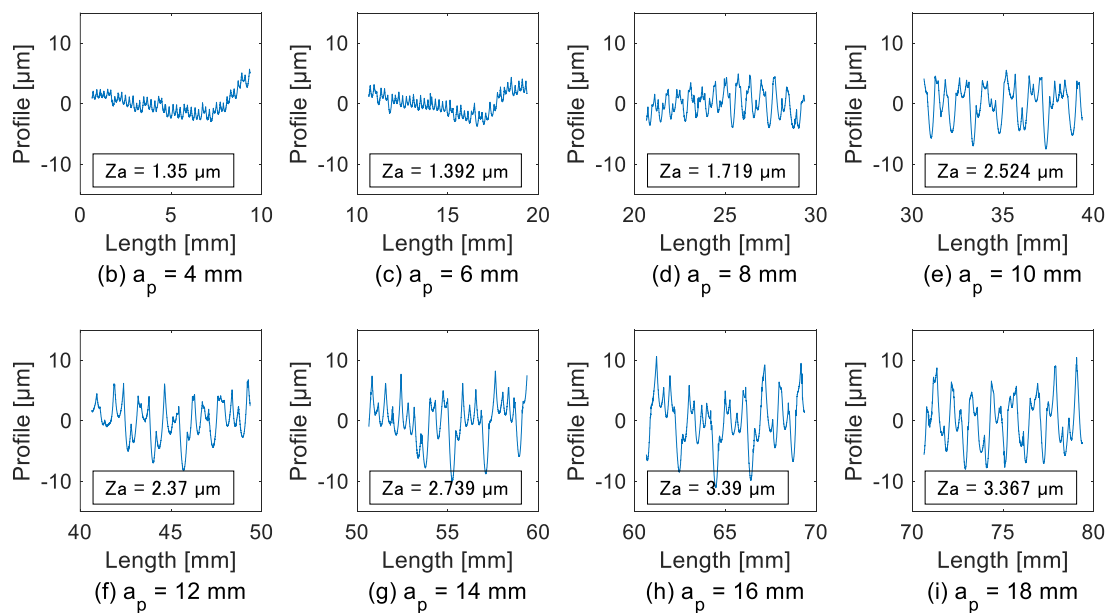


Fig. 5-22 Surface profile of a workpiece at cold start, 6000 min⁻¹.

side surface of each workpiece is firstly planned at 9000 min⁻¹ and is secondly milled at 6000 or 7000 min⁻¹ for validation. Each radial depth of cut is 1 mm. After processing two workpieces, impact tests were performed sequentially in the X- and Y-axes. The measurement intervals are represented by red dotted lines in Fig. 5-21.

5. Dynamical analysis and modeling of spindle units including thermomechanical effects

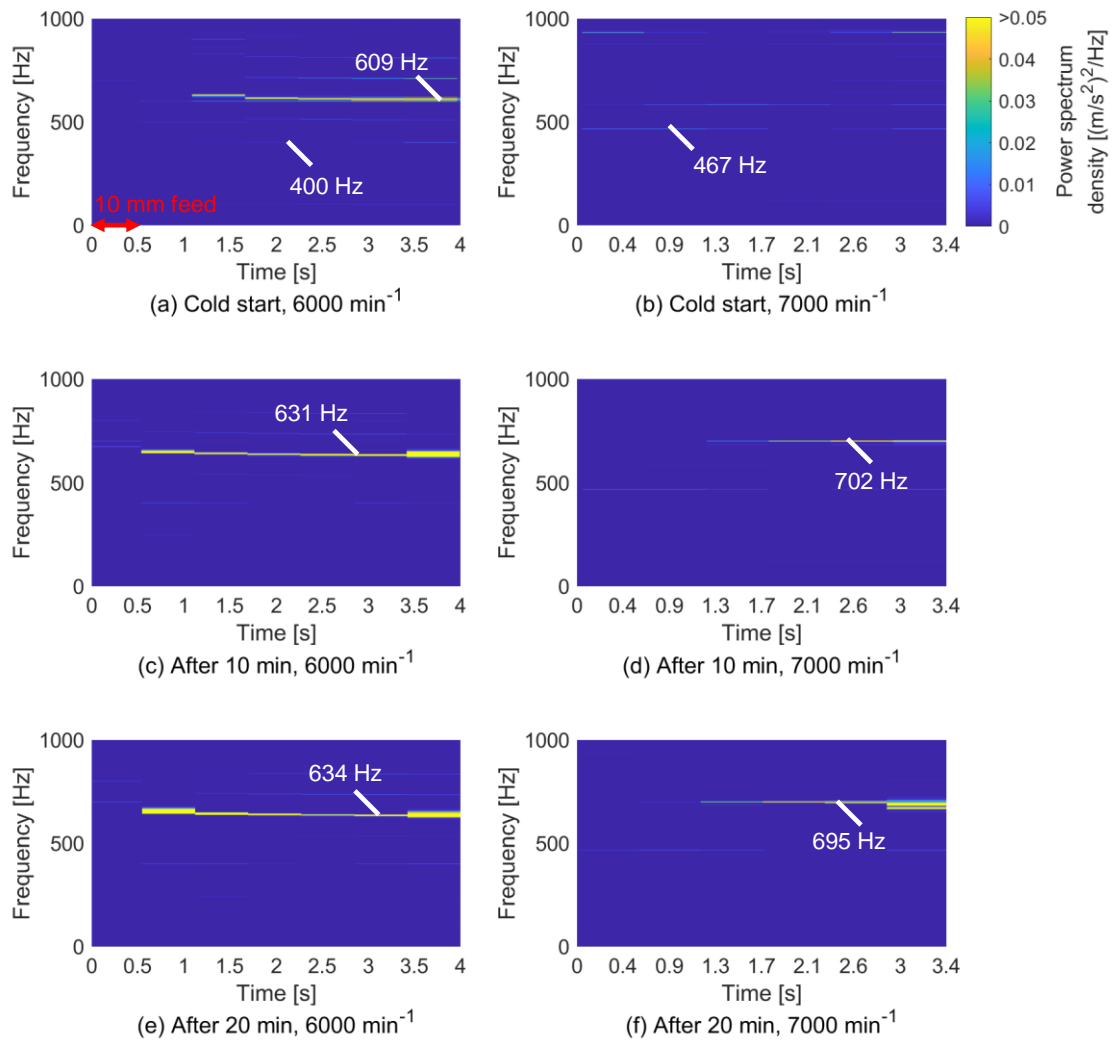


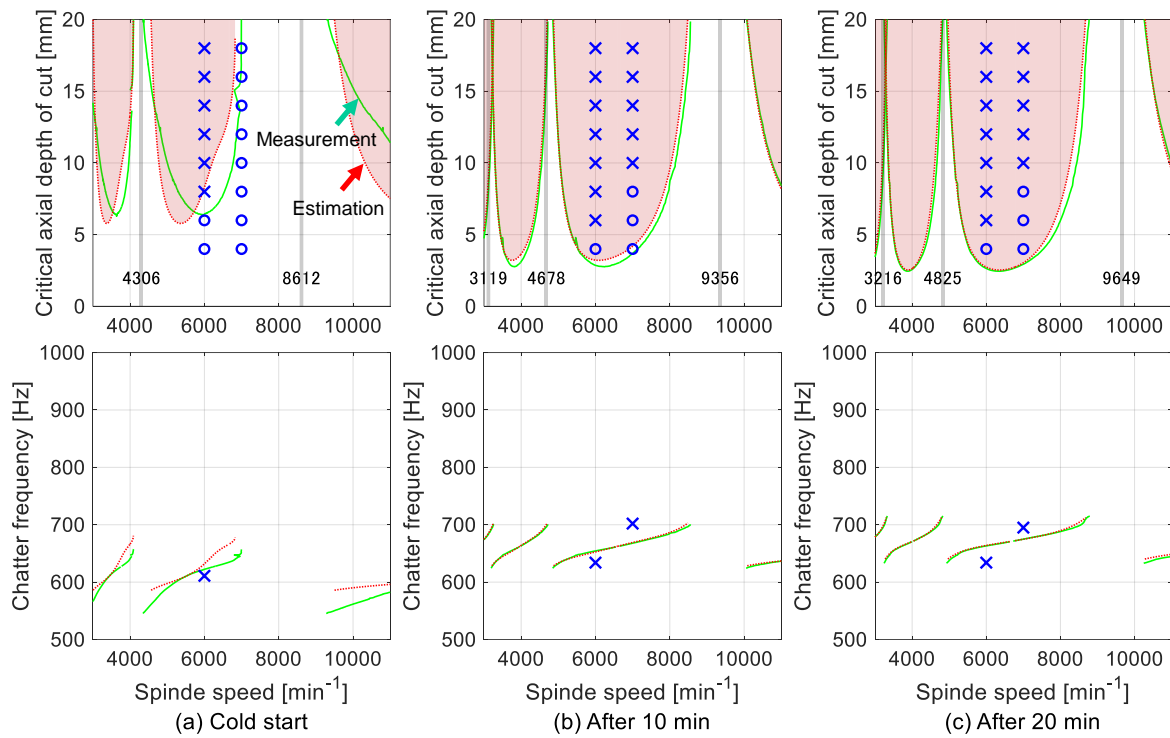
Fig. 5-23 Short-time Fourier transform analysis of acceleration signals.

5.5.2. Results of milling tests and process stability

Figure 5-22 shows a surface profile of a workpiece at cold start, 6000 min^{-1} , as an example. The side surface is measured by a surface roughness tester (SURFCOM-FLEX-50A, TOKYO SEIMITSU). The measurement resolutions in vertical and horizontal directions are 0.016 and $32 \mu\text{m}$, respectively. The sample points for the arithmetical mean height of a line in each depth of cut are 5451, and the results are listed in the figures. More than the axial depth of cut 6 mm , the chatter mark on the surface is observed and surface roughness decreases.

Figure 5-23 shows the results of short-time Fourier transform analysis during side milling tests. The sample points of windowing are 4096. The ticks of the time axis correspond to the feed 10 mm . Tooth-passing frequencies of the 4-teeth endmill are 400 and 467 Hz at spindle rotational speeds 6000 and 7000 min^{-1} , respectively. Therefore, small peaks with around power spectrum density $0.015 \text{ (m/s}^2\text{)}^2\text{/Hz}$ can be observed at these

5. Dynamical analysis and modeling of spindle units including thermomechanical effects



$$K_{tc} = 220 \text{ MPa}, \frac{K_{rc}}{K_{tc}} = 0.3$$

Fig. 5-24 Stability limit diagrams under temperature changes; red dotted lines represent the proposed models; green lines represent the measurements; the gray area with spindle rotational speeds represents the proposed DSST design; markers o/x represent milling test results of stable/unstable process in (a) first measurement at cold start (b) second measurement after spindle rotation for 10 min (c) third measurement after spindle rotation for 20 min in total.

frequencies and their harmonics. Over the axial depth of cut 6 mm in Fig. 5-23(a), the maximum amplitude can be observed at 609 Hz and corresponds to the decrease of surface roughness. If higher power spectrum density in another frequency is observed, it is decided that chatter is occurred at the conditions.

Figure 5-24 shows stability limit diagrams under temperature changes. The machining conditions of the tool diameter and radial depth of cut are used for analysis conditions. The material conditions of the cutting force coefficient and its ratio are decided from tensile strength and a previous study [54], [96]. The process stability is estimated by the proposed models and measured FRFs. The milling test results of process stability at each machining condition are plotted by markers. The stability limit diagrams using the proposed models show almost the same stability prediction to these by using the measurements. At spindle rotational speed 7000 min^{-1} , chatter is not detected at cold start machining. On the other hand, chatter is occurred after warm-up operation more than the axial depth of cut 8 mm.

5. Dynamical analysis and modeling of spindle units including thermomechanical effects

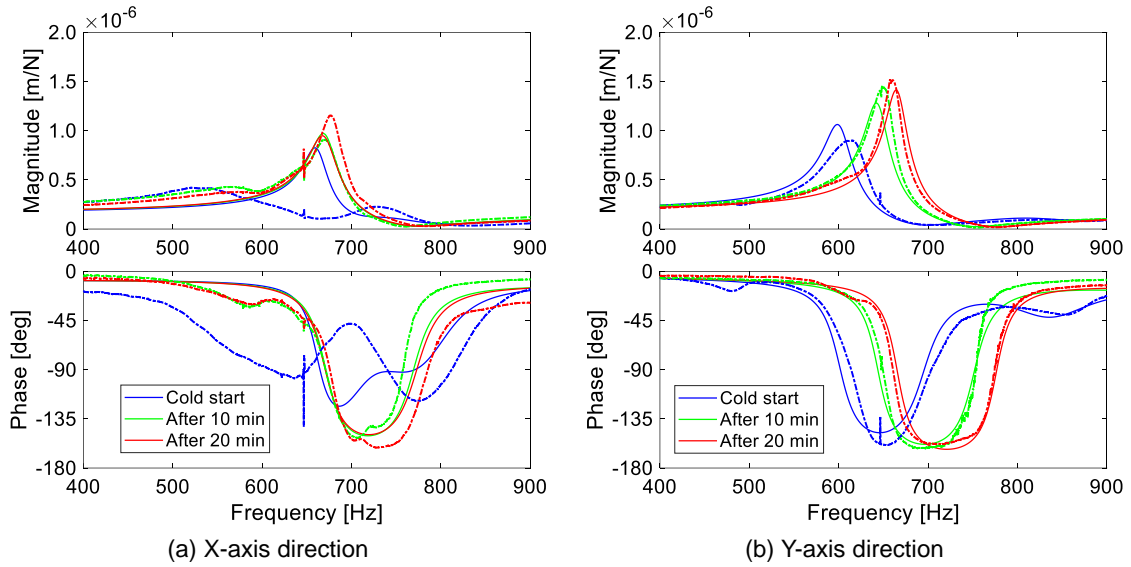


Fig. 5-25 FRFs at the tool tip in milling tests; solid lines represent the models, and dotted lines the measurements.

Owing to the increase of resonant frequency by the thermomechanical effects, the stability pockets move to a higher frequency. The proposed DSST design can estimate the optimal spindle rotational speed for high-efficiency machining. However, the chatter conditions after warm-up operation have differences between estimations and milling test results.

5.5.3. Discussion of estimated FRFs at the tool tip and chatter conditions

Figure 5-25 shows the FRFs of the estimations and measurements under three temperature conditions similar to Fig. 5-18. The magnitude and the phase of FRFs in the Y-axis direction can be estimated even if the second resonant frequency appears at cold start. The estimation performance is confirmed against other heat generation phenomena by cutting forces in the short-term. However, the model in the X-axis direction estimates only one resonant frequency at cold start. It is confirmed that the bearing–spindle–holder model cannot estimate the FRF measured at the holder end even though the model uses identified bearing properties not those of the estimation. As the discussion in subsection 5.3.3. and 5.4.2., the kinematic models with coupling as the spring–damper system for the holder–tool interface must be considered. The results imply that the kinematic assumption at cold start is not enough to express FRFs. According to previous research for high-precision modeling of the assembly, a uniform distribution of springs was modeled for taper contact characteristics [97]. The tool of the proposed models was assumed as a cylinder without flutes and its materials are defined as stainless steel. The determination of

5. Dynamical analysis and modeling of spindle units including thermomechanical effects

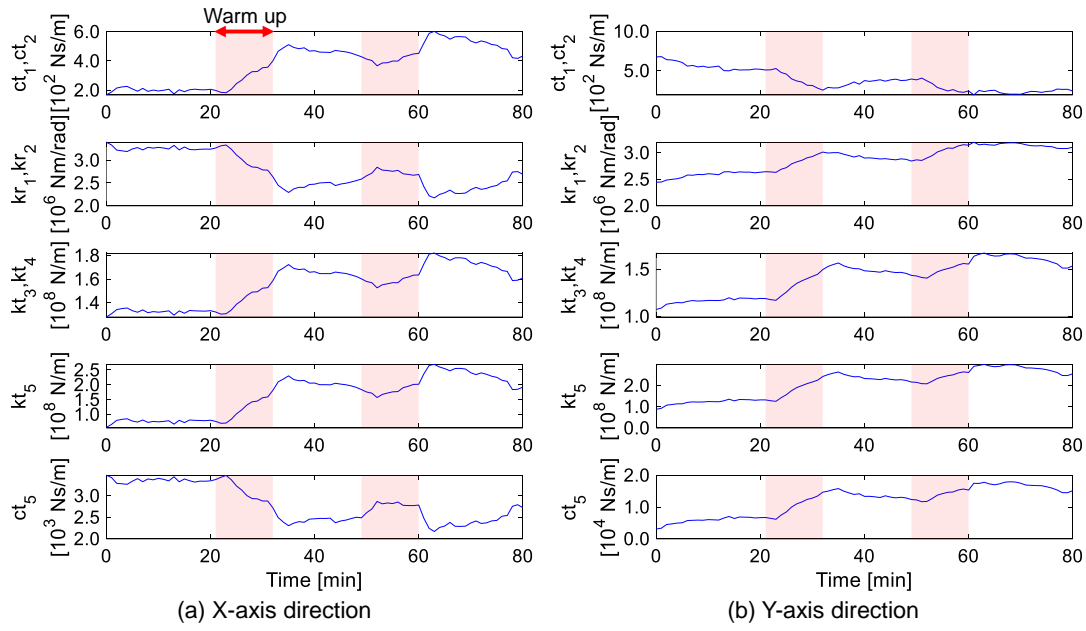


Fig. 5-26 Time behaviors of estimated bearing properties from temperature measurement; the time axis corresponds to Fig. 5-21.

mechanical/material properties of the holder, collet, and tool can improve the models similar to the CFRP components in this research or previous research [98]. Owing to the accumulation of modeling errors in bearing property identification, the estimation performance can be improved by considering the inaccuracy of the receptance matrixes. Besides, Fig. 5-26 shows time behaviors of estimated bearing properties. The regression models based on MLR use temperature signals. The kinematic assumption of the assembly and the linear correlation to temperature measurement work as a low-pass filter, which is an advantage in comparison with other ML approaches directly estimating the curve of FRFs or having nonlinear correlations between the properties and input signals.

Regarding the SLDs at 7000 min^{-1} , milling tests showed higher critical depths of cut than the analysis even though the difference between the measurements and models is little. As mentioned in subsection 1.4.3, machine tool dynamics changes are the main sources of errors. Another factor is process damping forces [99] generated by the contact of flank faces to the workpiece. The process damping forces cause the increase of critical depths of cut. In addition, bearing stiffness changes with spindle speed are considered. In previous research on measuring FRFs through milling tests [100], natural frequency decreases, and the damping ratio increases when spindle speeds increase. The spindle rotation induces the shift of SLDs in the lower spindle speed direction and higher critical depths of cut. Moreover, the cutting force coefficients decrease according to the increase in spindle speed [101]. To determine accurate parameters of machining conditions instead of the nominal values in this research, additional measurements by using dynamometers are required. The proposed

5. Dynamical analysis and modeling of spindle units including thermomechanical effects

MLR method has the potential to include these factors by using such measurements (i.e., inverse analysis, impacting under spindle rotation, and employing dynamometers).

From two measurement results of FRFs at the tool tip under temperature variation, the proposed MLR method can model the measured FRFs by using temperature information. The developed models of bearing properties have an expandability to the machine tool dynamics at the tool tips by receptance coupling, which can utilize various holder–tool assemblies.

5.6. Summary

This chapter describes dynamical analysis and modeling of spindle units including thermomechanical effects. Impact tests were conducted at the spindle nose under the conditions of warmup, standby, and idle reduction considering two energy-saving machining methods. The measurement results were used for the modeling of spindle unit dynamics including thermomechanical effects on bearings. The proposed models and their application to the DSST design were experimentally validated by impact tests at the tool tip and milling tests. The contents are summarized as follows.

- The procedure of experimental modeling of spindle unit dynamics including thermomechanical effects on bearings was proposed. The equivalent bearing properties were identified from the measured FRFs. The identified bearing properties were regressed as MLR models with temperature signals as the explanatory variables. The regression models were included in the dynamical models of spindle units proposed in Chapter 4.
- As per the comparison of FRFs at the tool tip under the conditions of cold start and after spindle rotation for 1 h, the resonant frequencies increase by 175 Hz in the X-axis and by 78 Hz in the Y-axis. Moreover, vibration mode after warmup operation return to that at cold start when the idle time is longer than 40 min. The warmup operation is essential to stabilize the thermomechanical effects.
- The operation of the chiller has little influence on the thermomechanical behavior of bearing properties under idle conditions.
- The proposed models can estimate FRFs at the tool tip within an error margin of 10 Hz of resonant frequency under temperature fluctuations. However, the FRFs have two major resonant frequencies in the X-axis when the machine tool is cooled. The proposed models can be improved by considering measurement data and

5. Dynamical analysis and modeling of spindle units including thermomechanical effects

regression methods to describe this phenomenon.

- Multipoint receptance coupling can identify the contact parameters at the spindle–holder and holder–tool interfaces. The properties of the spindle–holder interface changed with the temperature conditions. The translational stiffness and damping decrease after the warmup operation.
- The proposed models are used for updating SLDs. Moreover, a novel DSST design using the proposed models was demonstrated to control the spindle speeds in stability pockets. This chatter avoidance technique can be conducted by feedforward control without measuring chatter frequency.
- Side milling tests revealed the proposed models estimated FRFs at the tool tip under heat generation in process. The difference in process stability can be predicted by temperature signals. However, the accurate prediction of process stability can be achieved by considering other factors of mechanical/material property changes.

6. Conclusions

In this dissertation, experimental analysis and modeling of thermal errors and dynamics for machine tool spindle units were conducted by developing a temperature analysis environment on IoT systems.

Chapter 1 provided an overview of digital twins, which are the basic concepts of CPS, to install the intelligence on machine tools. From the viewpoint of installing high-power motors, composite materials, and energy-saving machining methods on recent machine tool spindle units, the improvement of machining accuracy, productivity, and energy efficiency can be achieved by addressing thermal errors and chatter using digital twins (i.e., SOMS). Based on the limitations of modeling approaches for thermal deformation and dynamics to develop SOMS, the research direction and objectives in this dissertation were defined.

Chapter 2 described the development of a temperature analysis environment for a CFRPMT and IoT systems as a platform for digital twins. The design and improvement of mechanical characteristics of each element of the CFRPMT were reviewed. The developed temperature analysis environment can run for measurement, data acquisition, data storage, computerization, and feedback in real time. Various applications of digital twins can be installed on the developed application server or on another launched server, where considerable temperature information can be used. The communication delay of the developed temperature analysis environment on temperature data through networks was evaluated. The developed temperature analysis environment has a high sampling frequency with acceptable delay for thermal error compensation techniques.

Chapter 3 described thermal error analysis of CFRP spindle units. Considering the implementation of two energy-saving machining methods, thermal error measurement was conducted using a test bar. Thermal errors showed different behaviors depending on whether the energy-saving machining methods were implemented. The different behaviors must be considered in the development of estimation models as well as mechanical design. Moreover, ambient temperature fluctuations strongly affect the behavior of thermal errors. The optimization of thermal error estimation has the potential to improve energy-saving methods for cooling units not only of chillers but also of thermostatic chambers.

Thermal error modeling was conducted using the measurement results. Most temperature measurement points of 302 are independent in the temperature distribution measurement every 1 min. Supposing flexible manufacturing systems, thermal error model deals with the integrated values of relative displacement estimated by MLR model with

temperature changes. An application server on the temperature analysis environment estimated thermal errors after work positioning. The estimation performance of thermal error models was evaluated according to the variation of datasets for training and the number of sensors for explanatory variables. The measurement data under the maximum spindle speed is effective to train sufficient models with fewer instances of train datasets. Optimal models of thermal errors suggested that CFRPMTs with energy-saving machining methods can realize both high-precision and energy efficiency simultaneously.

Chapter 4 proposed dynamical models of CFRP spindle units. Mechanical property of composite materials was formulated using the volume ratio or layouts of the TBMs to partially replace the analytical models and employ general solutions. In addition, multipoint receptance coupling was proposed. Both FRFs and mode shapes were observed by generalizing the receptance coupling to multi-points. The proposed method can avoid approximation of the dynamic system and number of calculations for combining the bearings. The mechanical property identification and multipoint receptance coupling can drastically reduce the computational costs of dynamical analysis of CFRP spindle shafts. Moreover, the bearing properties and contact characteristics assumed spring–damper systems can be experimentally identified using multipoint receptance coupling.

The dynamical models of CFRP spindle shafts were experimentally validated. The comparison of analytical spindle shaft models with impact tests as free-end conditions indicated that assuming a uniform distribution of composite materials on the applicable location resulted in a more accurate estimation of natural frequencies and mode shapes compared with that acquired from FEA and considering stacking sequences of composite materials was robust against the parameterization errors of CFRP, as confirmed by the sensitivity analysis. The receptance coupling of each layer's dynamics in the transverse direction resulted in lower accuracy owing to the accumulation of the modeling/parameterization errors. Therefore, the layers model was employed in the dynamical models of spindle units and their application. Additionally, the simplified models can be used in designing phases of CFRP spindle shafts.

The dynamical models of CFRP spindle units were developed by combining the spindle shaft models with the rotor model and bearing properties. The bearing properties were identified from the FRFs of impact tests based on the optimization procedure. Two resonant peaks of the FRFs at the spindle nose were measured, and their mode shapes were investigated. Moreover, the effect of application of CFRP was revealed by comparing it with the steel spindle shaft model and models designing the CFRP layout. The design proposals for improving the dynamic stiffness were provided. However, the expansion of the applicable location for CFRP must be considered.

Chapter 5 proposed dynamical models of spindle units, including thermomechanical effects. The equivalent bearing properties were identified from the measured FRFs using multipoint receptance coupling. The MLR models of bearing properties estimated using temperature signals were combined with the CFRP spindle shaft model.

Impact tests at the spindle nose considering the two energy-saving machining methods indicated that the operation of the chiller has little influence on the thermomechanical behavior of bearing properties under idle conditions. Moreover, resonant frequencies at the tool tip drastically increased after warmup operation as compared to cold start. After a certain period from the start of idle conditions, the vibration mode after warmup operation returned to that at cold start. The warmup operation is essential to stabilize the thermomechanical effects.

The proposed regression models of bearing properties were coupled to whole spindle dynamics. Comparing the FRFs of the measurements with the proposed models at the tool tip, it was confirmed that machine tool dynamics can be estimated under temperature fluctuations. The additional operation for compensating the inaccuracy of dynamical models can be reduced by the proposed models. Side milling tests clarified that the proposed models could estimate the FRFs at the tool tip not only under warm-up and standby conditions in the long-term but also under other heat generation conditions by cutting process in the short-term. Moreover, a novel discrete spindle speed tuning design using the proposed models was demonstrated to control the spindle speeds in stability pockets for high-efficiency machining. The application to SLDs can predict the changes in chatter conditions owing to the thermomechanical effects. These results clarified that the kinematic modeling of the bearing–spindle–holder–tool system and the linear correlation of the MLR model to temperature measurement contribute the robust estimation of FRFs against overfitting. This chatter avoidance technique can be installed at feedforward control without any applications of chatter detection and can realize high-efficiency machining.

In the development of thermal error models, the estimation performance was only validated against spindle rotation. Besides, the limitation of only employing MLR was confirmed by the saturation of the estimation performance with respect to the number of train datasets and sensors. As the literature review suggested, clustering methods and nonlinear algorithms should be used for high estimation accuracy with fewer number of sensors. In addition, the learning process in this study was conducted offline. The temperature analysis environment has the potential to be extended to adaptive process monitoring technologies based on big data analysis. Consequently, IoT systems can be retrofitted to multiple machine tools exclusively through connections with CNCs.

In the development of dynamical models, spindle shafts were modified by TBMs and were combined with bearing properties to spindle units by multipoint receptance coupling.

The FRFs of tool tips can be easily estimated by developing the models of tools and holders. Since the analytical models can estimate FRFs necessary to predict the stability limit, the dynamical modeling methods contribute to optimizing design proposals in developmental phases. The developed spindle shaft models can be repurposed in the application to the dynamical models of the whole spindle unit. However, it is not suitable for cases where a design proposal has already been determined or for three-dimensional analysis considering the geometry of pipes. The spindle unit models can be used for the investigation of bearing properties and contact parameters to fit models to measurement results on CPS. The proposed models on the temperature analysis environment demonstrated the connection between physical and virtual entities for digital twins.

Additionally, the models of thermal errors and spindle unit dynamics, including thermomechanical effects, use MLR, which is a simple ML technique, assuming a linear relationship between inputs and output. Abundant number of sensors with IoT systems and kinematic approaches can improve the performance of ML techniques. Even if the field of computer science gets attention, the work of mechanical engineering still plays an important role in the development of CPS.

In the future perspective of digital twins in the industry, measurement equipment for thermal errors occupies the workspace. Moreover, the impact tests for identification of bearing properties can be performed by operators. The development of in- or between-process measurement methods is also required. The measured data should be used for automatically updating models under operations. Accurate information on thermal deformation and dynamics can improve model-based control methods and extend machining performance. The relationship between machining accuracy, efficiency, machining conditions, and operation of cooling systems must be analyzed for constructing digital twins to optimize energy efficiency. The intelligence works for the optimization of the entire process and provides some knowledge for optimal conditions. To this end, the evaluation of actual phenomena, including compensation methods, using the proposed models and feedback control is the future research direction.

Appendices

A) Measurement location of LATSIS

Figure A-1 shows the temperature sensors of LATSIS. The sensor signals in asynchronous serial communication are received by the Windows computer through a converter with a microcontroller (CP2102, Silicon Laboratories). Every temperature sensor adhered to the CFRPMT with thermal conductive silicon (SCV-22, Sunhayato). Its thermal conductivity is 0.92 W/mk. A measurement test confirmed that the responsiveness of temperature sensors covered by that was enough to measure the temperature of machine tool structures every 1 min.

Table A-1 lists the measurement location of LATSIS. In this research, temperature A is the mean value of two sensor signals 56 and 66, B is 55 and 67, C is 87 and 74, D is 88 and 73, E is 89 and 72, F is 93 and 99, IR is 301 and 302, respectively. Temperature Room is the mean value of twenty sensor signals for ambient inside the machine tool cover.

B) Validation of the discretization of the dimensions in the Z-axis direction

In the calculation of the Timoshenko beam model, the cross-sectional area was assumed to be uniform in each segment. In a taper with a slope, the discretization of dimensions is a major source of modeling errors. Figure B-1 shows the parameters according to the length of the front end. The value of the center in each segment is used for the inner diameter listed in Table B-1 and the calculation results were listed in Table 4-2.

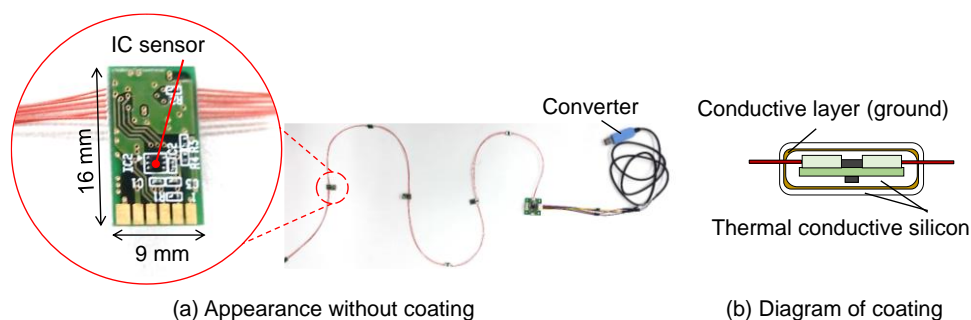


Fig. A-1 Temperature sensors of LATSIS.

Table A-1 Contact temperature sensor location of LATSIS mounted on CFRPMT

Component	Number	Parts	Label
Ambient	20	-	1–5, 110–124
Spindle unit	65	Ram with Z-axis linear guide rail	45–50, 57–65, 102–109
		Cast metal	51–54, 68–89
		Housing	55, 56, 66, 67
		Front cover of the spindle	90–101
X-axis slider	39	Z-axis motor	6, 7
		Z-axis motor coupling cover	8, 44
		Right side	9, 11, 12, 15, 18, 21, 22
		Bottom	24–27
		Left side	29, 30, 34, 35, 40, 41, 43
		Back	32, 36, 37
		X-axis linear guide	10, 13, 19, 23, 28, 31, 38, 42
		Z-axis linear guide	14, 20, 33, 39
Saddle	95	X-axis ball-screw nut	16, 17
		Back outside	125–128, 206–208, 210–214,
		Back inside	130–134
		Left side	129, 145, 146, 179, 201–203
		Right side	135–137, 189, 190, 191, 217–219,
		Front outside	153–157, 160, 194–198
		Front inside	161–169, 174, 175
		Bottom inside	170–173, 176, 177
		X-axis linear guide rail	138–144, 180–186
		X-axis motor	147, 148
		X-axis motor coupling cover	149–152
		Counter side X-axis ball-screw stand	158, 159, 187, 188
		Y-axis linear guide	192, 193, 199, 200, 204, 205, 215, 216
Y-axis ball-screw nut	209–211		
Bed	16	Front	220–223
		Left side	227, 228, 231–234
		Right side	295–300
Trunnion table	9	A-axis motor	224–226, 229, 230
		Counter side A-axis motor	288, 289, 290, 291
Column	54	Left outside	236–238, 243–245
		Left inside	240, 241
		Front	239, 242, 254, 255, 260, 261, 284, 287
		Top	270, 271, 276, 277
		Y-axis linear guide	246–253, 262–269
		Y-axis motor	279, 280
		Y-axis motor coupling cover	272–275
		Counter side Y-axis ball-screw stand	256–259
		Right outside	281–283, 292–294
Right inside	285, 286		
Cooling circuit of chiller	2	Joint for oil coming into chiller	235
		Joint for oil going out from chiller	278

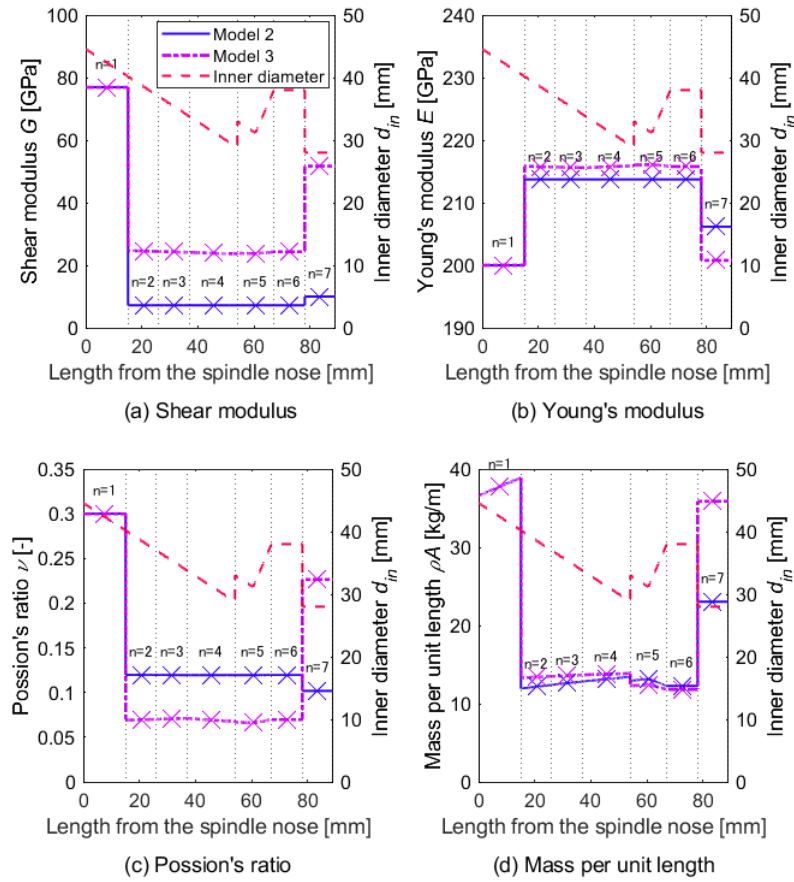

 Fig. B-1 Parameters of the spindle shaft at the taper part in the segments $n = 1-7$.

 Table B-2 Dimensions of CFRP spindle shaft $\mathbf{S}^{(D)}$

Segment number n	1	2	3	4	5	6	7	8	9	10	11	12	13	14	15
Length L_s [mm]	15.1	11.0	11.0	17.0	13.0	11.0	11.0	132.8	32.2	11.0	133.0	10.0	22.0	26.0	45.0
Outer diameter d_{out} [mm]	89.0	89.0	89.0	89.0	89.0	89.0	89.0	60.0	60.0	53.0 (85.0)	53.0 (98.6)	52.8 (85.0)	52.7	45.0	45.0
Inner diameter d_{in} [mm]	42.4	40.3	37.3	31.3	33.0	38.0	28.0	28.0	28.0	32.3	32.3	32.3	32.3	32.3	34.0
Material type q	1	2	2	2	2	2	3	3	1	1	1	1	1	1	1

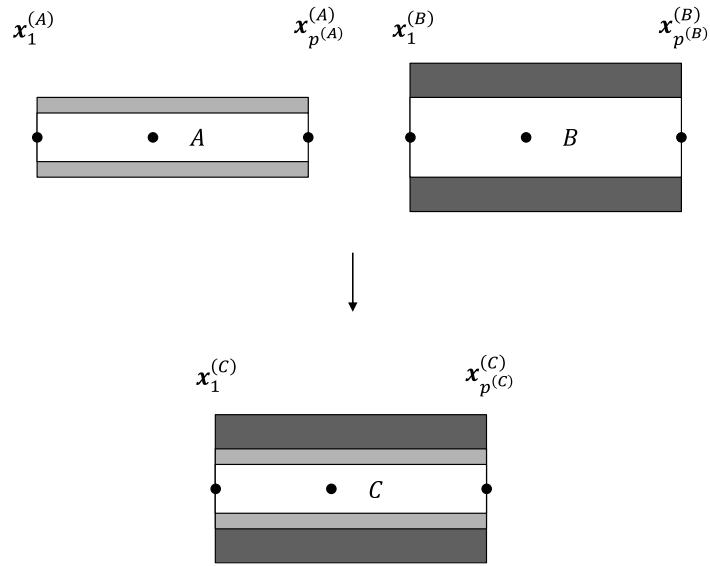


Fig. C-1 Schematic of multi-point receptance coupling in transverse direction.

C) Multipoint receptance coupling for individual components in transverse direction

Model 4 of the CFRP spindle shaft in section 4.3 is developed by the receptance coupling at multiple points in the transverse direction. Figure C-1 displays two segments with receptance matrices $\mathbf{S}^{(A)}$ and $\mathbf{S}^{(B)}$, following Equation (4-17). The segments were coupled by rigid joints. After coupling the two segments having the same number of coordinates at correlated points $p^{(A)} = p^{(B)} = p^{(C)}$, the displacement $\mathbf{x}^{(A)} = \mathbf{x}^{(B)} = \mathbf{x}^{(C)}$ becomes the same for all components. The component force vectors and displacement written in receptance matrix have the following relation.

$$\mathbf{F}^{(C)} = \mathbf{F}^{(A)} + \mathbf{F}^{(B)} \quad (\text{C-1})$$

$$\mathbf{S}^{(A)} \mathbf{F}^{(A)} = \mathbf{S}^{(B)} \mathbf{F}^{(B)} \quad (\text{C-2})$$

From Equations (C-1) and (C-2), the component force vectors $\mathbf{F}^{(A)}$ can be written by the external force vector as

$$\mathbf{F}^{(A)} = \left(\mathbf{S}^{(A)} + \mathbf{S}^{(B)} \right)^{-1} \mathbf{S}^{(B)} \mathbf{F}^{(C)} \quad (\text{C-3})$$

After rigid coupling, the displacement in each component becomes the same as the coupled component. The displacement can be expressed by Equation (C-3).

$$\mathbf{x}^{(C)} = \mathbf{S}^{(A)} \mathbf{F}^{(A)} = \mathbf{S}^{(A)} \left(\mathbf{S}^{(A)} + \mathbf{S}^{(B)} \right)^{-1} \mathbf{S}^{(B)} \mathbf{F}^{(C)} \quad (\text{C-4})$$

Therefore, the receptance matrix after coupling two segments can be expressed as:

$$\mathbf{S}^{(C)} = \mathbf{x}^{(C)} \mathbf{F}^{(C)-1} = \mathbf{S}^{(A)} \left(\mathbf{S}^{(A)} + \mathbf{S}^{(B)} \right)^{-1} \mathbf{S}^{(B)} \quad (\text{C-5})$$

D) Coefficients of bearing properties on multiple linear regression

Tables D-1 and D-2 list the coefficients of MLR models of five bearing properties along the X- and Y-axes.

E) Beam models of spindle–holder–tool assembly

In the calculation of the TBMs, the cross-sectional area was assumed have a uniform cylindrical shape in each segment of the components. The receptance matrix of each segment was calculated from the general solutions of the TBM under the boundary conditions of free ends. Young's modulus, shear modulus, and Poisson's ratio as the mechanical properties are required for the calculation. The mechanical properties of Cr–Mo steels for the holder and tool models are listed in Table E-1. The dimensions of the holder model and holder–tool model for the spindle–holder and spindle–holder–tool assemblies are listed in Tables E-2 and E-3, respectively. The segments are numbered from the front of the spindle unit. The dimensions of the spindle model with the rotor and sleeve for the assembly are also listed in Table E-4. The equivalent mechanical properties and dimensions of the CFRP spindle shaft are discussed in chapter 4. The segments from 1 to 5 consider the taper part of the holder contact inside with rigid joints. The contact characteristics at the holder–tool interface are considered between segments 1 and 2 in Table E-3 for the spindle–holder–tool assembly.

Table D-1 Coefficients of bearing properties in the X-axis direction

Signal	Intercept	T_{IR}	T_A	T_F	T_{Room}	ΔT_{IR}	ΔT_A
$ct_{1,2}$	2.91×10^3	-2.72×10	-2.39×10	3.07×10^2	-3.98×10^2	-2.70	1.45×10^2
$kr_{1,2}$	2.09×10^5	-1.06×10^5	5.92×10^5	-1.37×10^6	1.08×10^6	-1.96×10^4	-5.59×10^4
$kt_{3,4}$	1.26×10^8	1.63×10^7	9.44×10^6	-1.77×10^7	-8.83×10^6	-2.05×10^6	1.13×10^8
kt_5	-2.10×10^8	5.91×10^7	4.86×10^7	-9.78×10^7	2.43×10^6	-8.67×10^6	3.98×10^8
ct_5	-1.07×10^4	1.09×10^3	1.63×10^3	-4.11×10^3	2.04×10^3	-2.41×10^2	2.90×10^3

Signal	ΔT_F	ΔT_{Room}	ΔT_{IR}^2	ΔT_A^2	ΔT_F^2	ΔT_{Room}^2
$ct_{1,2}$	-1.33×10^2	7.77×10^2	2.50×10	5.50×10^2	1.77×10^2	-2.51×10^2
$kr_{1,2}$	1.18×10^6	-2.64×10^5	2.11×10^4	3.28×10^5	-4.29×10^6	-1.65×10^6
$kt_{3,4}$	-1.31×10^8	7.86×10^7	7.74×10^5	1.84×10^8	4.00×10^8	3.61×10^8
kt_5	-4.48×10^8	2.17×10^8	2.44×10^6	5.38×10^8	1.66×10^9	9.67×10^8
ct_5	-1.70×10^2	-1.52×10^2	-1.71×10^2	-1.87×10^3	4.47×10^2	9.61×10^3

Table D-2 Coefficients of bearing properties in the Y-axis direction

Signal	Intercept	T_{IR}	T_A	T_F	T_{Room}	ΔT_{IR}	ΔT_A
$ct_{1,2}$	-3.31×10^3	-2.70×10^2	8.19×10	-3.88×10^2	8.06×10^2	1.01×10^2	-8.01×10^2
$kr_{1,2}$	6.84×10^6	2.09×10^5	4.09×10^4	5.45×10^5	-1.05×10^6	-3.63×10^4	5.79×10^5
$kt_{3,4}$	-4.54×10^7	1.31×10^7	1.67×10^7	-3.38×10^7	1.15×10^7	-5.75×10^6	3.49×10^7
kt_5	-1.71×10^8	4.58×10^7	4.18×10^7	-6.07×10^7	-1.60×10^7	-1.84×10^7	1.81×10^8
ct_5	7.38×10^3	4.13×10^3	9.80×10^2	1.42×10^2	-5.76×10^3	-1.63×10^3	1.21×10^4

Signal	ΔT_F	ΔT_{Room}	ΔT_{IR}^2	ΔT_A^2	ΔT_F^2	ΔT_{Room}^2
$ct_{1,2}$	9.49×10^2	-1.34×10^3	4.34×10	9.46×10^2	-5.79×10^3	-5.52×10^3
$kr_{1,2}$	-1.73×10^6	2.22×10^6	-1.50×10^4	-1.56×10^6	1.55×10^7	3.63×10^6
$kt_{3,4}$	-9.71×10^6	-3.21×10^7	-1.97×10^6	1.88×10^7	-4.21×10^7	2.54×10^7
kt_5	-1.32×10^8	-4.49×10^7	-5.22×10^6	4.26×10^7	-2.05×10^6	1.42×10^8
ct_5	-1.20×10^4	5.42×10^3	-4.86×10^2	-5.73×10^3	2.08×10^4	2.82×10^4

Table E-1 Physical properties of the holder and tool models

Density [g/cm ³]	Young's modules [GPa]	Shear modules [GPa]	Poisson's ratio
7.81	212	82	0.28

 Table E-2 Dimensions of the holder model $\mathcal{S}^{(H)}$

Segment number	1	2	3	4	5	6	7	8	9
Length [mm]	25.0	6.0	20.5	26.5	5.4	2.9	4.3	2.9	10.6
Outer diameter [mm]	42.0	42.6	45.4	50.3	63.0	58.0	53.0	58.0	63.0
Inner diameter [mm]	20.0	20.0	20.0	20.0	20.0	20.0	20.0	20.0	20.0

 Table E-3 Dimensions of the holder and tool model $\mathcal{S}^{(H)}$ and $\mathcal{S}^{(T)}$

Segment number	1	2	3	4	5	6	7	8	9	10
Length [mm]	40.0	25.0	6.0	20.5	26.5	5.4	2.9	4.3	2.9	10.6
Outer diameter [mm]	10.0	42.0	42.6	45.4	50.3	63.0	58.0	53.0	58.0	63.0
Inner diameter [mm]	0	0	0	20.0	20.0	20.0	20.0	20.0	20.0	20.0

 Table E-4 Dimensions of the spindle model for coupling with the holder model $\mathcal{S}^{(S)}$

Segment number n	1	2	3	4	5	6	7	8	9	10	11	12	13	14	15
Length L_s [mm]	15.1	11.0	11.0	17.0	13.0	11.0	11.0	132.8	32.2	11.0	133.0	10.0	22.0	26.0	45.0
Outer diameter d_{out} [mm]	89.0	89.0	89.0	89.0	89.0	89.0	89.0	60.0	60.0	85.0	98.6	85.0	52.7	45.0	45.0
Inner diameter d_{in} [mm]	16.0	16.0	16.0	16.0	16.0	38.0	28.0	28.0	28.0	32.3	32.3	32.3	32.3	32.3	34.0

References

- [1] J. Leng, D. Wang, W. Shen, X. Li, Q. Liu, X. Chen, “Digital twins-based smart manufacturing system design in Industry 4.0: A review,” *Journal of Manufacturing Systems*, vol. 60, pp. 119–137, 2021, doi: 10.1016/j.jmsy.2021.05.011.
- [2] L. Monostori, B. Kádár, T. Bauernhansl, S. Kondoh, S. Kumara, G. Reinhart, O. Sauer, G. Schuh, W. Sihn, K. Ueda, “Cyber-Physical Systems in manufacturing,” *CIRP Annals*, vol. 65, no. 2, pp. 621–641, 2016, doi: 10.1016/j.cirp.2016.06.005.
- [3] L. Monostori, “Cyber-Physical Systems,” in *CIRP Encyclopedia of Production Engineering*, Springer, 2018, pp. 1–8. doi: 10.1007/978-3-642-35950-7_16790-1.
- [4] E. Negri, L. Fumagalli, M. Macchi, “A review of the roles of digital twin in CPS-based production systems,” *Procedia Manufacturing*, vol. 11, pp. 939–948, 2017, doi: 10.1016/j.promfg.2017.07.198.
- [5] R. Stark and T. Damerou, “Digital Twin,” in *CIRP Encyclopedia of Production Engineering*, Springer, 2019, pp. 1–8. doi: 10.1007/978-3-642-35950-7_16870-1.
- [6] J. Munoa, X. Beudaert, Z. Dombovari, Y. Altintas, E. Budak, C. Brecher, G. Stepan, “Chatter suppression techniques in metal cutting,” *CIRP Annals*, vol. 65, no. 2, pp. 785–808, 2016, doi: 10.1016/j.cirp.2016.06.004.
- [7] J. Mayr, J. Jedrzejewski, E. Uhlmann, M. A. Donme, W. Knapp, F. Härtig, K. Wendt, T. Moriwaki, P. Shore, R. Schmitt, C. Brecher, T. Würz, K. Wegener, “Thermal issues in machine tools,” *CIRP Annals*, vol. 61, no. 2, pp. 771–791, 2012, doi: 10.1016/j.cirp.2012.05.008.
- [8] M. Putz, C. Richter, J. Regel, M. Bräunig, “Industrial relevance and causes of thermal issues in machine tools,” *Proceedings Conference on Thermal Issues in Machine Tools*, vol. 1, pp 127–139, 2018.
- [9] H.-C. Möhring, C. Brecher, E. Abele, J. Fleischer, F. Bleicher, “Materials in machine tool structures,” *CIRP Annals*, vol. 64, no. 2, pp. 725–748, 2015, doi: 10.1016/j.cirp.2015.05.005.
- [10] R. Kondo, D. Kono, A. Matsubara, “Evaluation of machine tool spindle using carbon fiber composite,” *International Journal of Automation Technology*, vol. 14, no. 2, pp. 294–303, 2020, doi: 10.20965/ijat.2020.p0294.
- [11] D. Kono, S. Mizuno, T. Muraki, M. Nakaminami, “A machine tool motorized spindle with hybrid structure of steel and carbon fiber composite,” *CIRP Annals*, vol. 68, no. 1, pp. 389–392, 2019, doi: 10.1016/j.cirp.2019.04.022.
- [12] E. Frontoni, J. Loncarski, R. Pierdicca, M. Bernardini, M. Sasso, “Cyber Physical Systems for Industry 4.0: towards real time virtual reality in smart manufacturing,” *Augmented Reality, Virtual Reality, and Computer Graphics*, Cham, 2018, pp. 422–

434. doi: 10.1007/978-3-319-95282-6_31.
- [13] H.-C. Möhring, P. Wiederkehr, K. Erkorkmaz, Y. Kakinuma, “Self-optimizing machining systems,” *CIRP Annals*, vol. 69, no. 2, pp. 740–763, 2020, doi: 10.1016/j.cirp.2020.05.007.
- [14] “MTConnect,” MTConnect. <https://www.mtconnect.org> (accessed Aug. 07, 2022).
- [15] B. Edrington, B. Zhao, A. Hansel, M. Mori, M. Fujishima, “Machine Monitoring System Based on MTConnect Technology,” *Procedia CIRP*, vol. 22, pp. 92–97, 2014, doi: 10.1016/j.procir.2014.07.148.
- [16] C. Liu, X. Xu, Q. Peng, Z. Zhou, “MTConnect-based cyber-physical machine tool: a case study,” *Procedia CIRP*, vol. 72, pp. 492–497, 2018, doi: 10.1016/j.procir.2018.03.059.
- [17] P. Lei, L. Zheng, C. Li, X. Li, “MTConnect enabled interoperable monitoring system for finish machining assembly interfaces of large-scale components,” *Procedia CIRP*, vol. 56, pp. 378–383, 2016, doi: 10.1016/j.procir.2016.10.060.
- [18] “OPC Unified Architecture,” OPC Foundation. <https://opcfoundation.org/about/opc-technologies/opc-ua/> (accessed Aug. 07, 2022).
- [19] “UMATI — UNIVERSAL MACHINE TECHNOLOGY INTERFACE,” VDW — Verein Deutscher Werkzeugmaschinenfabriken e.V. (German Machine Tool Builders’ Association). <https://umati.org/> (accessed Aug. 07, 2022).
- [20] A. Martins, J. Lucas, H. Costelha, C. Neves, “Developing an OPC UA server for CNC machines,” *Procedia Computer Science*, vol. 180, pp. 561–570, 2021, doi: 10.1016/j.procs.2021.01.276.
- [21] M. Volkmann, T. Legler, A. Wagner, M. Ruskowski, “A CAD feature-based manufacturing approach with OPC UA skills,” *Procedia Manufacturing*, vol. 51, pp. 416–423, 2020, doi: 10.1016/j.promfg.2020.10.059.
- [22] B. Denkena, E. Abele, C. Brecher, M.-A. Dittrich, S. Kara, M. Mori, “Energy efficient machine tools,” *CIRP Annals*, vol. 69, no. 2, pp. 646–667, 2020, doi: 10.1016/j.cirp.2020.05.008.
- [23] J.-S. Chen, W.-Y. Hsu, “Characterizations and models for the thermal growth of a motorized high speed spindle,” *International Journal of Machine Tools and Manufacture*, vol. 43, no. 11, pp. 1163–1170, 2003, doi: 10.1016/S0890-6955(03)00103-2.
- [24] E. Abele, Y. Altintas, C. Brecher, “Machine tool spindle units,” *CIRP Annals*, vol. 59, no. 2, pp. 781–802, 2010, doi: 10.1016/j.cirp.2010.05.002.
- [25] A. Wirtz, M. Meiner, P. Wiederkehr, J. Myrzik, “Simulation-assisted investigation of the electric power consumption of milling processes and machine tools,” *Procedia CIRP*, vol. 67, pp. 87–92, 2018, doi: 10.1016/j.procir.2017.12.181.
- [26] L. Shabi, J. Weber, J. Weber, “Analysis of the energy consumption of fluidic systems

- in machine tools,” *Procedia CIRP*, vol. 63, pp. 573–579, 2017, doi: 10.1016/j.procir.2017.03.348.
- [27] A. M. M. S. Ullah, T. Akamatsu, M. Furuno, M. A. K. Chowdhury, A. Kubo, “Strategies for developing milling tools from the viewpoint of sustainable manufacturing,” *International Journal of Automation Technology*, vol. 10, no. 5, pp. 727–736, 2016, doi: 10.20965/ijat.2016.p0727.
- [28] W. Lee, S. H. Kim, J. Park, B.-K. Min, “Simulation-based machining condition optimization for machine tool energy consumption reduction,” *Journal of Cleaner Production*, vol. 150, pp. 352–360, 2017, doi: 10.1016/j.jclepro.2017.02.178.
- [29] C. Hirano, K. Morishige, “Development of rough cutting method with plunge milling using 5-axis control machine tool,” *Journal of the Japan Society for Precision Engineering*, vol. 73, no. 11, pp. 1261–1266, 2007, doi: 10.2493/jjspe.73.1261 (in Japanese).
- [30] Y. Oda, M. Fujishima, Y. Takeuchi, “Energy-saving machining of multi-functional machine tools,” *International Journal of Automation Technology*, vol. 9, no. 2, pp. 135–142, 2015, doi: 10.20965/ijat.2015.p0135.
- [31] M. Fujishima, H. Shimano, M. Mori, “Reducing the energy consumption of machine tools,” *International Journal of Automation Technology*, vol. 11, pp. 601–607, Jul. 2017, doi: 10.20965/ijat.2017.p0601.
- [32] J. Regel, D. Xu, M. Bräunig, V. Wittstock, M. Putz, “Evaluation of thermo-energetic behavior for demand-oriented operating of machine tool cooling systems,” *Procedia Manufacturing*, vol. 21, pp. 213–220, 2018, doi: 10.1016/j.promfg.2018.02.113.
- [33] J. Weber, L. Shabi, J. Weber, “State of the art and optimization of the energy flow in cooling systems of motorized high-speed spindles in machine tools,” *Procedia CIRP*, vol. 67, pp. 81–86, 2018, doi: 10.1016/j.procir.2017.12.180.
- [34] M. Fujishima, Oda Y., Mori M., “Energy consumption reduction of machine tools,” *Journal of the Japan Society for Precision Engineering*, vol. 78, no. 9, pp. 752–756, 2012, doi: 10.2493/jjspe.78.752 (in Japanese).
- [35] S.-K. Cho, H.-J. Kim, S.-H. Chang, “The application of polymer composites to the table-top machine tool components for higher stiffness and reduced weight,” *Composite Structures*, vol. 93, no. 2, pp. 492–501, 2011, doi: 10.1016/j.compstruct.2010.08.030.
- [36] M. Kashihara, K. Yamamoto, M. Furuta, H. Yonetani, T. Tumura, K. Nakata, S.-Y. Kim, S. Suzuki, H. Nakajima, “Application of lotus-type porous carbon steel to moving body of machine tools,” *Trans.JSME, Ser.C*, vol. 77, no. 784, pp. 4693–4703, 2011, doi: 10.1299/kikaic.77.4693.
- [37] M. Kato, D. Kono, H. Yoshioka, N. Sugita, A. Hamaguchi, K. Kono, K. Iijima, Y. Kakinuma, “Thermal error and energy-saving performance evaluation of the energy-

- saving machine tool using new structural materials,” *Transactions of the JSME*, vol. 86, no. 884, p. 20–00002, 2020, doi: 10.1299/transjsme.20-00002 (in Japanese).
- [38] M. Kato, Y. Mizoguchi, K. Kono, Y. Kakinuma, “Machining-based thermal error analysis of CFRP-structured machine tool,” *Proceedings of the Machining Innovations Conference*, 2020, doi: 10.2139/ssrn.3724093.
- [39] I. Inasaki, “Kikai kakō shisutemu : kōsei yōsokan no sōgo sayō to shisutemu no kōseinōka”. Yokendo, 2009 (in Japanese).
- [40] S. Shimizu, “Shoho kara manabu kōsaku kikai : Kyōtsūna kihon kōzō to shikumi ga wakaru,” Kogyo Chosakai Publishing, 2009 (in Japanese).
- [41] G. Spur, H. Fischer, “Thermal behaviour of machine tools,” *Advances in Machine Tool Design and Research*, pp. 147–160, 1969, doi: 10.1016/B978-0-08-015661-3.50013-8.
- [42] “Thermo-Friendly Concept | Intelligent Technology,” OKUMA CORPORATION. <https://www.okuma.co.jp/english/onlyone/thermo/> (accessed Aug. 19, 2022).
- [43] T. Saito, S. Nomura, H. Imai, “Measurement of Radial Thermal Expansivity of Carbon Fiber,” *Tanso*, vol. 1991, no. 146, pp. 22–26, 1991, doi: 10.7209/tanso.1991.22.
- [44] N. Noda, G. Hotta, Y. Sano, Y. Takase, “Mechanics and Stress Concentration for Bonded Dissimilar Materials,” CORONA, 2017 (in Japanese).
- [45] K. Mori, B. Bergmann, D. Kono, B. Denkena, A. Matsubara, “Energy efficiency improvement of machine tool spindle cooling system with on–off control,” *CIRP Journal of Manufacturing Science and Technology*, vol. 25, pp. 14–21, 2019, doi: 10.1016/j.cirpj.2019.04.003.
- [46] C. Ma, L. Zhao, X. Mei, H. Shi, J. Yang, “Thermal error compensation of high-speed spindle system based on a modified BP neural network,” *Int J Adv Manuf Technol*, vol. 89, no. 9–12, pp. 3071–3085, 2017, doi: 10.1007/s00170-016-9254-4.
- [47] S. N. Grama, A. Mathur, R. Aralaguppi, T. Subramanian, “Optimization of high speed machine tool spindle to minimize thermal distortion,” *Procedia CIRP*, vol. 58, pp. 457–462, 2017, doi: 10.1016/j.procir.2017.03.253.
- [48] R. Ramesh, M. Mannan, A.-N. Poo, S. Keerthi, “Thermal error measurement and modelling in machine tools. Part II. Hybrid Bayesian Network - Support vector machine model,” *International Journal of Machine Tools & Manufacture*, vol. 43, pp. 405–419, 2003, doi: 10.1016/S0890-6955(02)00264-X.
- [49] Y. C. Liang, W. D. Li, P. Lou, J. M. Hu, “Thermal error prediction for heavy-duty CNC machines enabled by long short-term memory networks and fog-cloud architecture,” *Journal of Manufacturing Systems*, vol. 62, pp. 950–963, 2022, doi: 10.1016/j.jmsy.2020.10.008.
- [50] M. Mareš, O. Horejš, L. Havlík, “Thermal error compensation of a 5-axis machine tool using indigenous temperature sensors and CNC integrated Python code validated with a machined test piece,” *Precision Engineering*, vol. 66, pp. 21–30, 2020, doi:

- 10.1016/j.precisioneng.2020.06.010.
- [51] Y. Sasaki, H. Iwai, Y. Wakazono, Y. Sakurai, Y. Oka, “Development of real-time thermal displacement compensation system,” *Journal of the Japan Society for Precision Engineering*, vol. 83, no. 2, pp. 121–124, 2017, doi: 10.2493/jjspe.83.121 (in Japanese).
- [52] T. Kizaki, S. Tsujimura, Y. Marukawa, S. Morimoto, H. Kobayashi, “Robust and accurate prediction of thermal error of machining centers under operations with cutting fluid supply,” *CIRP Annals*, vol. 70, no. 1, pp. 325–328, 2021, doi: 10.1016/j.cirp.2021.04.074.
- [53] P. Blaser, F. Pavliček, K. Mori, J. Mayr, S. Weikert, K. Wegener, “Adaptive learning control for thermal error compensation of 5-axis machine tools,” *Journal of Manufacturing Systems*, vol. 44, pp. 302–309, 2017, doi: 10.1016/j.jmsy.2017.04.011.
- [54] E. Shamoto, “Mechanism and suppression of chatter vibrations in cutting,” *Denkiseikou*, vol. 82, no. 2, pp. 143–155, 2011 (in Japanese).
- [55] E. I. Rivin, “Vibration isolation of precision equipment,” *Precision Engineering*, vol. 17, no. 1, pp. 41–56, 1995, doi: 10.1016/0141-6359(94)00006-L.
- [56] T. Brezina, L. Brezina, J. Vetiska, “Improvement of heavy machine tool dynamics by passive dynamic vibration absorber,” *MM SJ*, vol. 2015, no. 04, pp. 838–845, 2015, doi: 10.17973/MMSJ.2015_12_201545.
- [57] Y. Altıntaş E. Budak, “Analytical prediction of stability lobes in milling,” *CIRP Annals*, vol. 44, no. 1, pp. 357–362, Jan. 1995, doi: 10.1016/S0007-8506(07)62342-7.
- [58] M. A. Davies, J. R. Pratt, B. S. Dutterer, T. J. Burns, “The stability of low radial immersion milling,” *CIRP Annals*, vol. 49, no. 1, pp. 37–40, 2000, doi: 10.1016/S0007-8506(07)62891-1.
- [59] E. Shamoto, K. Akazawa, “Analytical prediction of chatter stability in ball end milling with tool inclination,” *CIRP Annals*, vol. 58, no. 1, pp. 351–354, 2009, doi: 10.1016/j.cirp.2009.03.087.
- [60] Z. Dombovari, Y. Altintas, G. Stepan, “The effect of serration on mechanics and stability of milling cutters,” *International Journal of Machine Tools and Manufacture*, vol. 50, no. 6, pp. 511–520, 2010, doi: 10.1016/j.ijmachtools.2010.03.006.
- [61] S. Turner, D. Merdol, Y. Altintas, K. Ridgway, “Modelling of the stability of variable helix end mills,” *International Journal of Machine Tools and Manufacture*, vol. 47, no. 9, pp. 1410–1416, 2007, doi: 10.1016/j.ijmachtools.2006.08.028.
- [62] Z. Dombovari, G. Stepan, “The effect of helix angle variation on milling stability,” *Journal of Manufacturing Science and Engineering*, vol. 134, no. 5, 2012, doi: 10.1115/1.4007466.
- [63] V. Sellmeier, B. Denkena, “Stable islands in the stability chart of milling processes due to unequal tooth pitch,” *International Journal of Machine Tools and Manufacture*,

- vol. 51, no. 2, pp. 152–164, 2011, doi: 10.1016/j.ijmachtools.2010.09.007.
- [64] L. Zhu, C. Liu, “Recent progress of chatter prediction, detection and suppression in milling,” *Mechanical Systems and Signal Processing*, vol. 143, p. 106840, 2020, doi: 10.1016/j.ymssp.2020.106840.
- [65] Z. Sun, J. Xiao, X. Yu, R. Tusiime, H. Gao, W. Min, L. Tao, L. Qi, H. Zhang, M. Yu, “Vibration characteristics of carbon-fiber reinforced composite drive shafts fabricated using filament winding technology,” *Composite Structures*, vol. 241, p. 111725, 2020, doi: 10.1016/j.compstruct.2019.111725.
- [66] M. Yang, L. Gui, Y. Hu, G. Ding, C. Song, “Dynamic analysis and vibration testing of CFRP drive-line system used in heavy-duty machine tool,” *Results in Physics*, vol. 8, pp. 1110–1118, 2018, doi: 10.1016/j.rinp.2018.01.067.
- [67] K. G. Bang, D. G. Lee, “Design of carbon fiber composite shafts for high speed air spindles,” *Composite Structures*, vol. 55, no. 2, pp. 247–259, 2002, doi: 10.1016/S0263-8223(01)00146-5.
- [68] T. L. Schmitz, G. S. Duncan, “Receptance coupling for dynamics prediction of assemblies with coincident neutral axes,” *Journal of Sound and Vibration*, vol. 289, no. 4, pp. 1045–1065, 2006, doi: 10.1016/j.jsv.2005.03.006.
- [69] T. Schmitz, “Modal interactions for spindle, holders, and tools,” *Procedia Manufacturing*, vol. 48, pp. 457–465, 2020, doi: 10.1016/j.promfg.2020.05.069.
- [70] T. Schmitz, E. Betters, E. Budak, E. Yüksel, S. Park, Y. Altintas, “Review and status of tool tip frequency response function prediction using receptance coupling,” *Precision Engineering*, vol. 79, pp. 60–77, 2023, doi: 10.1016/j.precisioneng.2022.09.008.
- [71] O. Özşahin, E. Budak, H. N. Özgüven, “Identification of bearing dynamics under operational conditions for chatter stability prediction in high speed machining operations,” *Precision Engineering*, vol. 42, pp. 53–65, 2015, doi: 10.1016/j.precisioneng.2015.03.010.
- [72] D. Zulli, “A one-dimensional beam-like model for double-layered pipes,” *International Journal of Non-Linear Mechanics*, vol. 109, pp. 50–62, 2019, doi: 10.1016/j.ijnonlinmec.2018.11.006.
- [73] K. M. Liew, Z. Z. Pan, L. W. Zhang, “An overview of layerwise theories for composite laminates and structures: Development, numerical implementation and application,” *Composite Structures*, vol. 216, pp. 240–259, 2019, doi: 10.1016/j.compstruct.2019.02.074.
- [74] A. S. Sayyad, Y. M. Ghugal, “Bending, buckling and free vibration of laminated composite and sandwich beams: A critical review of literature,” *Composite Structures*, vol. 171, pp. 486–504, 2017, doi: 10.1016/j.compstruct.2017.03.053.
- [75] L. Iurlaro, A. Ascione, M. Gherlone, M. Mattone, M. Di Sciuva, “Free vibration

- analysis of sandwich beams using the Refined Zigzag Theory: an experimental assessment,” *Meccanica*, vol. 50, no. 10, pp. 2525–2535, 2015, doi: 10.1007/s11012-015-0166-4.
- [76] F. Shadmehri, B. Derisi, S. V. Hoa, “On bending stiffness of composite tubes,” *Composite Structures*, vol. 93, no. 9, pp. 2173–2179, 2011, doi: 10.1016/j.compstruct.2011.03.002.
- [77] A. Erturk, H. N. Özgüven, E. Budak, “Analytical modeling of spindle-tool dynamics on machine tools using Timoshenko beam model and receptance coupling for the prediction of tool point FRF,” *International Journal of Machine Tools and Manufacture*, vol. 46, no. 15, pp. 1901–1912, 2006, doi: 10.1016/j.ijmachtools.2006.01.032.
- [78] H. Özgüven, E. Budak, “Effect analysis of bearing and interface dynamics on tool point FRF for chatter stability in machine tools by using a new analytical model for spindle–tool assemblies,” *International Journal of Machine Tools and Manufacture*, vol. 47, no. 1, pp. 23–32, 2007, doi: 10.1016/j.ijmachtools.2006.03.001.
- [79] S. Gao, K. Cheng, H. Ding, H. Fu, “Multiphysics-based design and analysis of the high-speed aerostatic spindle with application to micro-milling,” *Proceedings of the Institution of Mechanical Engineers, Part J: Journal of Engineering Tribology*, vol. 230, 2015, doi: 10.1177/1350650115619609.
- [80] C.-W. Lin, J. Tu, J. Kamman, “An integrated thermo-mechanical-dynamic model to characterize motorized machine tool spindles during very high speed rotation,” *International Journal of Machine Tools and Manufacture*, vol. 43, no. 10, pp. 1035–1050, 2003, doi: 10.1016/S0890-6955(03)00091-9.
- [81] Y. S. Tarn, E. C. Lee, “A critical investigation of the phase shift between the inner and outer modulation for the control of machine tool Chatter,” *International Journal of Machine Tools and Manufacture*, vol. 37, no. 12, pp. 1661–1672, 1997, doi: 10.1016/S0890-6955(97)00035-7.
- [82] S. Fukagawa, H. Fujimoto, Y. Terada, S. Ishii, “Experimental verification of chatter suppression in end milling process using cooperative control of spindle and stage motors,” *41st Annual Conference of the IEEE Industrial Electronics Society*, 2015, pp. 002794–002799. doi: 10.1109/IECON.2015.7392525.
- [83] S. Jayaram, S. G. Kapoor, R. E. DeVor, “Analytical stability analysis of variable spindle speed machining,” *Journal of Manufacturing Science and Engineering*, vol. 122, no. 3, pp. 391–397, 1999, doi: 10.1115/1.1285890.
- [84] N. Sugita, H. Yoshioka, Y. Kakinuma, D. Kono, “Shinkouzouzairyoutekiyousyouenegatakousakukikainokenkyuukaihatu,” *The Japan Society for Precision Engineering Spring Conference*, pp. 211–212, 2019, doi: 10.11522/pscjspe.2019S.0_211 (in Japanese).

- [85] J. Kato, H. Yoshioka, H. Shinno, K. Asakura, S. Goto, K. Usuda, N. Hori, “CFRPwotekiyoushitaneuhenkeiyokuseiborunezinoseinouhyouka,” The Japan Society for Precision Engineering Autumn Conference, pp. 145–146, 2018, doi: 10.11522/pscjspe.2018A.0_145 (in Japanese).
- [86] G. Zhang, J. Furusho, “Speed control of two-inertia system by PI/PID control,” Proceedings of the IEEE 1999 International Conference on Power Electronics and Drive Systems, 1999, vol. 1, pp. 567–572 vol.1. doi: 10.1109/PEDS.1999.794627.
- [87] S. Xiang, X. Yao, Z. Du, J. Yang, “Dynamic linearization modeling approach for spindle thermal errors of machine tools,” Mechatronics, vol. 53, pp. 215–228, 2018, doi: 10.1016/j.mechatronics.2018.06.018.
- [88] N. Zimmermann, S. Lang, P. Blaser, J. Mayr, “Adaptive input selection for thermal error compensation models,” CIRP Annals, vol. 69, no. 1, pp. 485–488, 2020, doi: 10.1016/j.cirp.2020.03.017.
- [89] J. Mayr, P. Blaser, A. Ryser, P. Hernandez-Becerro, “An adaptive self-learning compensation approach for thermal errors on 5-axis machine tools handling an arbitrary set of sample rates,” CIRP Annals, vol. 67, no. 1, pp. 551–554, 2018, doi: 10.1016/j.cirp.2018.04.001.
- [90] C. Zhang, F. Gao, L. Yan, “Thermal error characteristic analysis and modeling for machine tools due to time-varying environmental temperature,” Precision Engineering, vol. 47, pp. 231–238, 2017, doi: 10.1016/j.precisioneng.2016.08.008.
- [91] M. Schneider, F. Haag, A. K. Khalil, D. A. Breunig, “Evaluation of communication technologies for distributed industrial control systems: concept and evaluation of 5G and WiFi 6,” Procedia CIRP, vol. 107, pp. 588–593, 2022, doi: 10.1016/j.procir.2022.05.030.
- [92] J. D. Aristizabal-Ochoa, “Timoshenko beam-column with generalized end conditions and nonclassical modes of vibration of shear beams,” Journal of Engineering Mechanics, vol. 130, no. 10, pp. 1151–1159, 2004, doi: 10.1061/(ASCE)0733-9399(2004)130:10(1151).
- [93] M. Pastor, M. Binda, T. Harčarik, “Modal assurance criterion,” Procedia Engineering, vol. 48, pp. 543–548, 2012, doi: 10.1016/j.proeng.2012.09.551.
- [94] Y. Ito, T. Moriwaki, “Machine Tool Engineering (New Edition),” CORONA, 2019 (in Japanese).
- [95] H. Li, Y. C. Shin, “Analysis of bearing configuration effects on high speed spindles using an integrated dynamic thermo-mechanical spindle model,” International Journal of Machine Tools and Manufacture, vol. 44, no. 4, pp. 347–364, 2004, doi: 10.1016/j.ijmactools.2003.10.011.
- [96] A. Bhowmik, D. Mishra, “A comprehensive study of an aluminum alloy AL-5052,” vol. 3, no. 1, pp. 20–22, 2018.

- [97] M. Namazi, Y. Altintas, T. Abe, N. Rajapakse, “Modeling and identification of tool holder–spindle interface dynamics,” *International Journal of Machine Tools and Manufacture*, vol. 47, no. 9, pp. 1333–1341, 2007, doi: 10.1016/j.ijmachtools.2006.08.003.
- [98] T. Schmitz, A. Honeycutt, M. Gomez, M. Stokes, E. Betters, “Multi-point coupling for tool point receptance prediction,” *Journal of Manufacturing Processes*, vol. 43, pp. 2–11, 2019, doi: 10.1016/j.jmapro.2019.03.043.
- [99] Y. Altintas, M. Eynian, H. Onozuka, “Identification of dynamic cutting force coefficients and chatter stability with process damping,” *CIRP Annals*, vol. 57, no. 1, pp. 371–374, 2008, doi: 10.1016/j.cirp.2008.03.048.
- [100] N. Grossi, L. Sallese, F. Montevicchi, A. Scippa, G. Campatelli, “Speed-varying machine tool dynamics identification through chatter detection and receptance coupling,” *Procedia CIRP*, vol. 55, pp. 77–82, 2016, doi: 10.1016/j.procir.2016.08.022.
- [101] N. Grossi, L. Sallese, A. Scippa, G. Campatelli, “Chatter stability prediction in milling using speed-varying cutting force coefficients,” *Procedia CIRP*, vol. 14, pp. 170–175, 2014, doi: 10.1016/j.procir.2014.03.019.

Acknowledgements

This dissertation is a summary of my research work carried out from 2017 to 2022 as a member of Kakinuma laboratory in Keio University. Thanks to the endless guidance and support of numerous people, I could successfully complete my doctoral study.

Firstly, I would like to express my deepest gratitude to my supervisor, Professor Dr. Yasuhiro Kakinuma. He gave me a motivation to go on to the Ph.D. program and enthusiastically supported me throughout this research. He provided me with various opportunities such as attending conferences, writing journal articles, applying for grants and proposals for collaborative research with both academia and industry, and building international relationships with researchers. These opportunities are essential to develop my philosophy as an independent researcher. His insightful comments during our research meetings were helpful to deepen my understanding.

I would also like to express my gratitude to Senior Assistant Professor Dr. Ryo Koike. His insightful comments during our research meetings were helpful to deepen my understanding. Additionally, I would like to thank Professor Dr. Hideki Aoyama and Professor Dr. Masaki Takahashi of Keio University. They provided me with very beneficial comments and suggestions in developing this dissertation.

I would like to express my heartfelt gratitude to Assistant Professor Dr. Daisuke Kono from Kyoto University for his technical support on FEA with insightful advice. I would like to show my appreciation to Professor Dr. Naohiko Sugita, Professor Dr. Hayato Yoshioka, Project Research Associate Dr. Toru Kizaki, and Shun Tanaka from The University of Tokyo for their technical and fundamental support on installing LATSIS and maintaining research environment. In addition, their frank comments helped me refine my research direction.

I received a great deal of technical support and advice from industry in carrying out my research. I would like to express my gratitude to Kazunori Iijima from FANUC Corp. for his kind and polite assistance on my research. I could develop my philosophy through several collaboration research with him for 6 years. Additionally, I would like to appreciate Tomofumi Uwano and Takaki Shimoda from FANUC Corp. for the development of IoT systems. I would like to express my gratitude to Dr. Harumitsu Senda, Akihide Hamaguchi, and Yuji Mizoguchi for their technical support and knowledge on the operations of BaseMT and CFRPMT. I would like to express my gratitude to Humiyosi Ohtsuki and Teppei

Sasagawa from Japan Machine Tool Builders' Association for sustaining a favorable research environment. Moreover, I would like to express my gratitude to Nobuyuki Hori and Kozo Imanishi from JTEKT Corp.; Shingo Kajikawa and Kazumasa Kono from Makino Milling Machine Co. Ltd.; Manabu Sawada from Nakamura-Tome Co. Ltd.; and Yasuhiko Suzuki from Yamazaki Mazak Corp. Thanks to their assistance, I could carry out my experimental verifications.

I appreciate the former and current students in the laboratory — Dr. Shuntaro Yamato, Rei Miyata, Rintaro Yamaguchi, and Aoi Suzuki. I am really grateful to Kana Igarashi and Michie Ishiwata for their continuous contributions to sustaining a favorable research environment. I would also like to acknowledge the financial support provided to me by the Grant-in-Aid for JSPS Research Fellowship from the Japan Society for the Promotion of Science and the Keio University Doctoral Student Grant-in-Aid Program.

Finally, I would like to express my special thanks to my beloved parents and sisters for their endless support, and I was helped by friends who always invited me for a change.

February 2023

Makoto Kato